Università degli Studi di Ferrara

DOTTORATO DI RICERCA IN
"SCIENZE DELL'INGEGNERIA"

CICLO XXII

COORDINATORE Prof. Stefano Trillo

CHARACTERIZATION AND MODELING OF LOW FREQUENCY DISPERSIVE EFFECTS IN III-V ELECTRON DEVICES

Settore Scientifico Disciplinare ING-INF/01

Dottorando
Dott. Vadalà Valeria

____
(firma)

Tutore
Prof. Vannini Giorgio

____
(firma)

Anni 2007/2009

Contents

Preface V

Chapter 1 : III-V Electron Devices for Microwave Applications

Introduction 3

1.1 Gallium Nitride Properties 4

1.2 HEMT device 5

1.2.1 GaN HEMT device 10

1.3 Low frequency dispersion effect 12

1.4 Non linear modeling 16

References 19

Chapter 2 *:* Non-linear measurement systems for LF dispersion characterization and modelling

Introduction 25

2.1 Pulsed measurements 26

2.2 Load-Pull Measurements 28

2.3 Large Signal Network Analyzer 31

References 37

Chapter 3 : A novel measurement technique oriented to the characterization of low frequency dispersive effects

Introduction 41

3.1 Characterization of LF dispersion in microwave devices 42

3.2 Electron device characterization under nonlinear operation 44

3.3 Low frequency two-source large-signal measurement system … 46

3.3.1 The setup architecture …………………………………………. 47

3.3.2 The Control Software…………………………………………. 54

3.4 Experimental Results …………………………………………… 57

Conclusions ……………………………………………………… 64

References ………………………………………………………… 65

Chapter 4 : New Low-Frequency Model for Microwave Devices

Introduction ……………………………………………………… 69

4.1 Non linear modeling of Low frequency dispersion: model formulation ……………………………………………………... 71

4.2 Correction term effect ………………………………………… 75

4.3 Experimental results ………………………………………… 78

Conclusions ………………………………………………………90

References ……………………………………………………… 91

Chapter 5 : Low-Frequency Active Load-Pull Measurement System

Introduction ………………………………………………………97

5.1 The proposed method ……………………………………...98

5.2 Experimental Results ……………………………………... 103

Conclusions ……………………………………………………… 107

References ……………………………………………………..… 108

List of Publication ……………………………………………. 109

Acknowledgment ……………………………………………. 111

Preface

In this thesis, three years are enclosed of research activity in the topic of non linear characterization and modelling of microwave devices. I investigated various issues related to those topics which are closely related. In fact, to obtain good predictions, empirical models require accurate measurements. This aspect is particularly important when we want to predict the behavior of devices in nonlinear regime. More and more applications take advantage of devices operation in non-linear regime. For such a reason, non linear characterization is an hot topic and research activities have focused particular attention on the need of characterize the nonlinear behaviour of electron devices to obtain more accurate model prediction under actual operating conditions.

The importance of this theme can be clearly understood by considering how, in recent years, microwave technologies have become attractive for communication applications and a number of commercial devices which are largely used in everyday life (e.g., cell phone, GPS, wireless communication and so on).

In the first chapter the most important properties of devices and technologies used in microwave electronics circuits will be dealt with. Particular attention is devoted to the comparison between two III-V semiconductors for the fabrication of these devices: GaAs, proven technology and used for years, and GaN, a youngest technology still being tested. After this some of the most interesting issues related to III-V electron devices, are discussed, such as low frequency dispersion. Finally a brief look will be given at the non linear models for these devices.

In the second Chapter the most important microwave measurement systems exploited to characterize the non linear dynamic behaviour of electron devices will be discussed: pulsed setups, load / source-pull measurement systems, and Large Signal time domain characterization systems. In particular, for each measurement technique, it has been described the principle of operation and the application they are used for.

In chapter III an alternative, technology-independent large-signal measurement set-up, developed during the PhD studies, is proposed for the experimental investigation

on the low frequency dispersion of current/voltage characteristics in micro- and millimetre-wave electron devices and for their modeling. The proposed measurement technique will be presented describing its hardware and software implementations and showing different experimental examples.

In Chapter IV a new modeling approach will be presented accounting for the nonlinear description of low-frequency dispersive effects (due to thermal phenomena and traps) affecting electron devices. The model will be identified by exploiting measurements carried out with the measurement system described in chapter III.

In the last Chapter a new, low-cost technique will be described for drawing “load-pull contours” which are a powerful tool for power amplifier design. By exploiting the low-frequency measurement system described in chapter III and conventional descriptions of device parasitic elements and nonlinear reactive effects, the proposed approach allows to obtain the same information gathered by expensive high-frequency load pull measurement systems.

Prefazione

In questa tesi sono racchiusi tre anni di attività di ricerca nell'ambito delle misure non lineari e del modeling di dispositivi a microonde. Sono state affrontate diverse problematiche relative a tali ambiti che sono strettamente correlati. Per ottenere buone predizioni i modelli necessitano infatti di misure accurate. Questo aspetto è particolarmente importante quando si vuole predire il comportamento dei dispositivi in regime non lineare. Un numero sempre maggiore di applicazioni infatti sfrutta il funzionamento dei dispositivi in regime non lineare. Per questo motivo la caratterizzazione non lineare è un argomento di grande interesse e le attività di ricerca riguardanti questi argomenti hanno rilevato la necessità di caratterizzare il comportamento non lineare dei dispositivi al fine di ottenere modelli più accurati in diverse condizioni operative. L'importanza che riveste tutto questo può essere chiaramente valutata considerando che negli ultimi anni le tecnologie a microonde sono diventate interessanti per molte applicazioni largamente utilizzate nella vita di tutti i giorni come ad esempio la telefonia cellulare, il GPS, le comunicazioni wireless, la TV digitale, i protocolli di comunicazione UMTS, HDMA e così via.

Nel primo capitolo, verranno descritte le proprietà più importanti dei dispositivi e delle tecnologie utilizzate nei circuiti elettronici a microonde. Particolare attenzione sarà dedicata al confronto tra due dei semiconduttori III-V maggiormente usati per la fabbricazione di questi dispositivi: l'Arsenurio di Gallio (GaAs), tecnologia collaudata e utilizzata da anni, e il Nitruro di Gallio (GaN), tecnologia promettente e ancora in fase di maturazione. Successivamente saranno discusse alcune delle problematiche più interessanti relative a questi dispositivi, come ad esempio la dispersione in bassa frequenza. Infine verrà rivolto un breve sguardo ai modelli non lineari per i dispositivi a microonde.

Nel secondo capitolo saranno discussi i più importanti sistemi di misura a microonde utilizzati per caratterizzare il comportamento dinamico non lineare di dispositivi elettronici. Saranno descritti i sistemi di misura impulsati, i sistemi di misura source / load-pull, e infine i sistemi di misura a grande segnale operanti nel dominio del tempo

(Large Signal Network Analyzer). Di questi sarà descritto il principio di funzionamento e le più importanti applicazioni per cui vengono utilizzati.

Nel terzo capitolo sarà descritto un sistema di misura a grande segnale sviluppato durante il mio dottorato di ricerca. Si tratta di un sistema alternativo per la caratterizzazione dei fenomeni di dispersione a bassa frequenza delle caratteristiche di corrente nei dispositivi a microonde e ad onde millimetriche. Il sistema di misura in questione è indipendente dalla tecnologia che si vuole indagare. Oltre alla descrizione hardware della tecnica di misura sarà descritta anche l'implementazione del software di controllo sviluppato mostrando diversi esempi di misura.

Nel capitolo IV sarà presentato un nuovo approccio per il modeling degli effetti dispersivi in bassa frequenza (dovuti a fenomeni termici e a trappole) dei dispositivi elettronici a microonde. Il modello sarà identificato sfruttando le misurazioni effettuate con il sistema di caratterizzazione descritto nel capitolo III, e validato utilizzando vari sistemi di misura a grande segnale descritti nel capitolo 2.

Infine nel capitolo V sarà descritta una nuova tecnica per ottenere i contorni di load-pull, cioè i luoghi a parametri costanti che vengono comunemente utilizzati per il progetto di amplificatori di potenza a microonde. Sfruttando il sistema di misura a bassa frequenza descritto nel capitolo III e descrizioni convenzionali degli elementi parassiti ed effetti reattivi non lineari dei dispositivi, l'approccio proposto permette di ottenere le stesse informazioni ottenute tramite costosi sistemi di misura ad alta frequenza.

CHAPTER 1

III-V Electron Devices for Microwave Applications

Introduction

In the last years, microwave applications have become very attractive due to the increasing number of commercial devices exploiting microwave technologies (e.g., cell phone, GPS, wireless communication and so on) which are largely used in everyday life. This trend is reflected in a growing interest by companies that invest money in research themes related to these topics. The scenery of microwave and millimetre-wave applications is today dominated by solid state devices; many materials and devices are available for designers and applications but GaAs is the leading edge technology. At first with the MESFET (MEtal Semiconductor Field Effect Transistors) and then with the HEMT (High Electron Mobility Transistor), Gallium Arsenide devices, good performance was reached in terms of power, noise and efficiency at high frequency. The drawback of this kind of technology is related to high RF power and high temperature operating condition required in many applications. As a matter of fact, microwave power devices in GaAs produce RF power levels around 1 W/mm at millimetre waves and are able to operate with junction temperature around 150°C. This is not enough to meet the demands of increasing power and temperature at which the device should work for example in defence radar and communication system applications as well as wireless communication systems and satellite communication. Therefore alternative materials

were taken into account in recent years for microwave applications. In particular, wide band gap semiconductors allow to obtain microwave electronic devices with RF power capability an order of magnitude greater than that available from comparable devices fabricated from standard semiconductors, such as Si and GaAs. Presently, the best one is Gallium Nitride which shows the best performance in terms of power (6 W/mm) and efficiency for microwave applications. This primacy is due to amazing electrical properties like high breakdown voltage or high operative temperatures and also the ability to be integrated with silicon-based electronics.

1.1 Gallium Nitride Properties

The recent success of Gallium Nitride (GaN) devices is related to the unique material properties held by itself and its most important alloys like InGaN and AlGaN. These properties can be exploited to improve performance of nitride-based device. Wide energy bandgap generally translates into an ability to support high internal electric fields before electronic breakdown occurs, and also provides improved radiation resistance. GaN has an energy bandgap about two to three times those of the conventional semiconductors. High electric fields permit large terminal RF voltages to be supported, and this is necessary for the generation of high RF power levels.

The dielectric constant is an indication of the capacitive loading of a device and affects the transistor terminal impedances. This enables a wide bandgap device to be larger in area for a given impedance. Increased area leads to larger RF currents and higher RF power to be generated. Thermal conductance of the material is extremely important since this parameter indicates the ease with which dissipated power can be extracted from the device. Good thermal conductivity results in device operation at elevated temperature [1] requiring less stringent (and less expensive) thermal management solutions for the packaging of high power amplifiers.

Gallium Nitride has also a high activation energy for acceptors doping (about 170meV); therefore doping densities larger than two orders of magnitude are needed to achieve free hole concentration desired. This high doping density causes an extremely low hole mobility (on the order of 10 $cm^2V^{-1}s^{-1}$). On the other hand, GaN presents high electron mobility that, in conjunction with high breakdown field, is advantageous in high-speed and high-power electronics. Electrical properties of GaN

are presented in table 1.1 compared with other materials used for microwave applications.

	μ	ε	E_g	T_{max} [°C]	μ_n[cm^2/V·s] @300°K	θ [W/°K-cm]	BDV [MV/cm]
Si	1300	11.4	1.1	300	1400	1.5	0.6
GaAs	5000	13.1	1.4	300	8500	0.54	0.65
SiC(4H)	260	9.7	9.7	600	900	4	3.5
GaN	1500	9.5	9.5	700	440	1.3	3.5

Table 1.1: electrical properties of GaN

1.2 HEMT device

The High Electron Mobility Transistor is a field effect device based on a heterostructure, that is a junction between two semiconductor materials with different band-gap energies. To describe the structure and operation of HEMT devices a GaAs HEMT is considered. The heterostructure is obtained by contacting n-doped AlGaAs and undoped GaAs: the band diagram of this heterostructure is illustrated in Fig. 1.1.

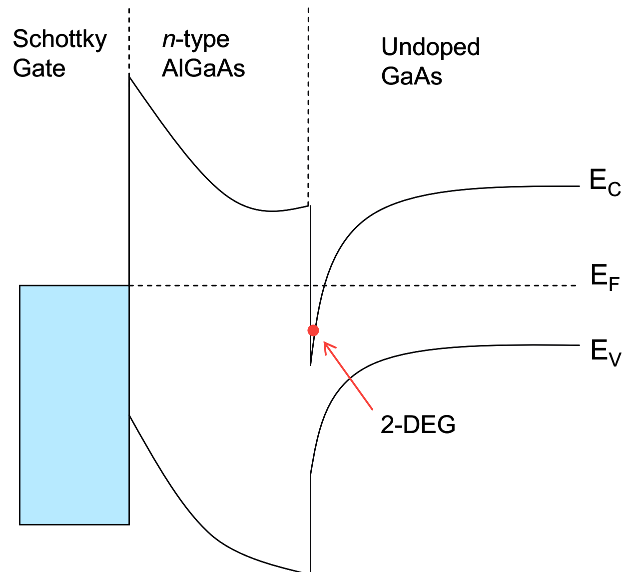

Fig. 1.1: Band diagram of the AlGaAs/GaAs heterostructure in the HEMT, under conditions of zero gate bias.

The wide-band-gap material is doped n-type, but is depleted of free carriers by the reverse or zero-biased Schottky contact, while the narrow-band-gap material is undoped or slightly doped p-type. At the boundary between the two materials the

band-gap discontinuities cause the conduction band of the GaAs to dip below the Fermi level, creating a potential well with a very high carrier concentration. This region of high carrier density is very thin, so that it is named two-dimensional electron gas (2-DEG). The electrons of the 2-DEG travel into an undoped material, thus without encountering ionized donor atoms: this makes them to have the highest mobility, favouring fast response times and high-frequency operation.
The whole conventional HEMT structure is reported in Fig. 1.2. Three metal electrode contacts are made on the surface of the semiconductor structure: as in the MESFET, the source and drain contacts are ohmic, while the gate is a Schottky junction. The presence of the heterostructure makes the structure of a HEMT much more complex with respect to a MESFET, leading to higher fabrication difficulties and costs and lower yields. Nevertheless, the 2-DEG-based current transport provides important improvements in terms of noise figure and high-frequency performances. In Fig. 1.2, a spacer undoped AlGaAs layer is also inserted in the heterojunction, in order to limit the scattering effects on the 2-DEG electrons at the interface, due to ionized donor of the doped AlGaAs.

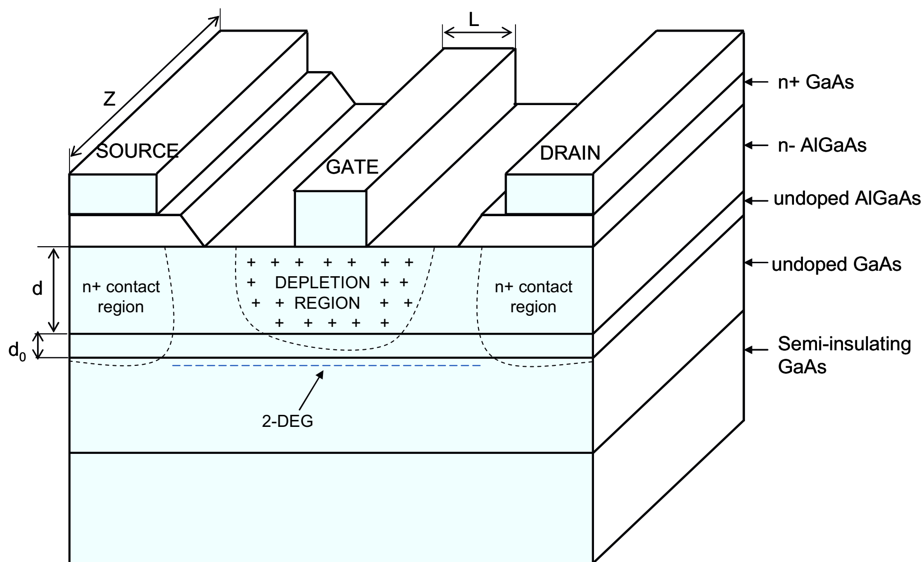

Fig. 1.2: A conventional HEMT structure.

Important geometric parameters of the device are the surface geometry dimensions, especially the ones labelled L and Z in Fig. 1.2. The gate length L is the most important parameter because determines, in fact, the maximum frequency limits for the HEMT. The device current, instead, is directly proportional to the gate width Z, thus relatively small-gate-width devices are used for low-noise and low-current

applications, while large-gate-width devices are typically employed in power applications. Actual device layout are, anyway, more complex: a T-shaped gate allows to decrease the gate length without excessively increasing the gate parasitic resistance, the use of recessed gate structure decreases the source and drain parasitic resistances, the gate width is extended by repeating the same elementary cell in a multiple-fingers layout (as, for instance, in Fig. 1.3)

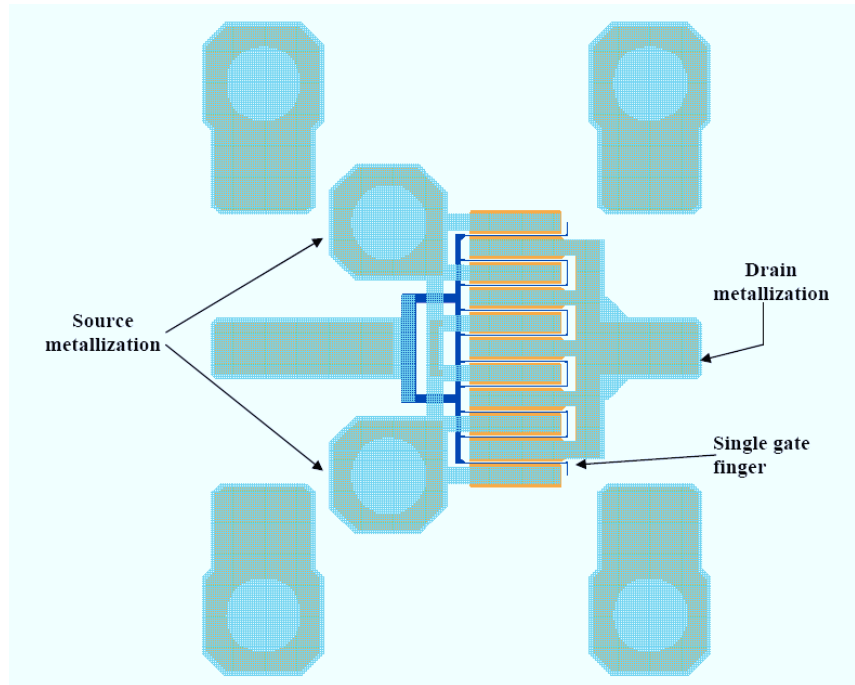

Fig. 1.3: Metallization layout for an actual FET device. The device has a gate width of 1 mm, made up of ten 100-μm fingers.

The device behaviour is also determined by the thickness of both the n-type and the undoped AlGaAs spacer layer, labelled in Fig. 1.2 as d and d_0, respectively. These dimensions are on the order of 0.03 to 0.2 μm for the n-type layer and around 50 Å for the spacer layer. In particular, the thickness of the n-type AlGaAs is designed in such a way that this layer is completely depleted from free electrons under normal operating conditions.

Most microwave FETs are depletion mode device, that is in the absence of applied reverse gate bias, current can flow between the drain and source contacts. In this conditions, current can flow between the drain and source contacts when no reverse gate bias is applied. Zero gate bias the band diagram is like in Fig 1.1, and the 2-DEG is formed. Under this bias condition a sharp dip in the conduction band edge

occurs in the HEMT at AlGaAs\GaAs boundary, this implies a high carrier concentration in a narrow region along the GaAs side of the heterojunction. The high free electron concentration occurs over a thin region that is referred as 2-DEG and characterized in terms of a sheet carrier density. Contact with the 2-DEG is made by means of heavily doped, low-resistance source and drain wells. Electrons travelling in 2-DEG do not encounter ionized donor atoms because the GaAs is undoped. In order to avoid problems related to dopant ions in the wide band gap semiconductor a pseudomorphic HEMT (PHEMT) device is largely exploited where InGaAs channel layer is put between the AlGaAs spacer and the GaAs. In this way higher mobility and increased saturation velocity are obtained.

For low value of drain-source voltage a current flows from drain to source through the electron gas. This current is initially proportional to the drain-source voltage, but as the electron velocity reaches the saturation for increasing voltage values, also the current levels saturate. The saturation current level is determined primarily by the sheet carrier density of 2-DEG. To control the 2-DEG density, gate bias is exploited: as the negative gate voltage increases, the depth of the potential well decreases, resulting in decreasing of the 2-DEG electron density and, thus, of the current levels, until reaching the pinch-off voltage. Fig 1.4 shows the static drain current characteristic measured for a 0.25 µm GaAs PHEMT.

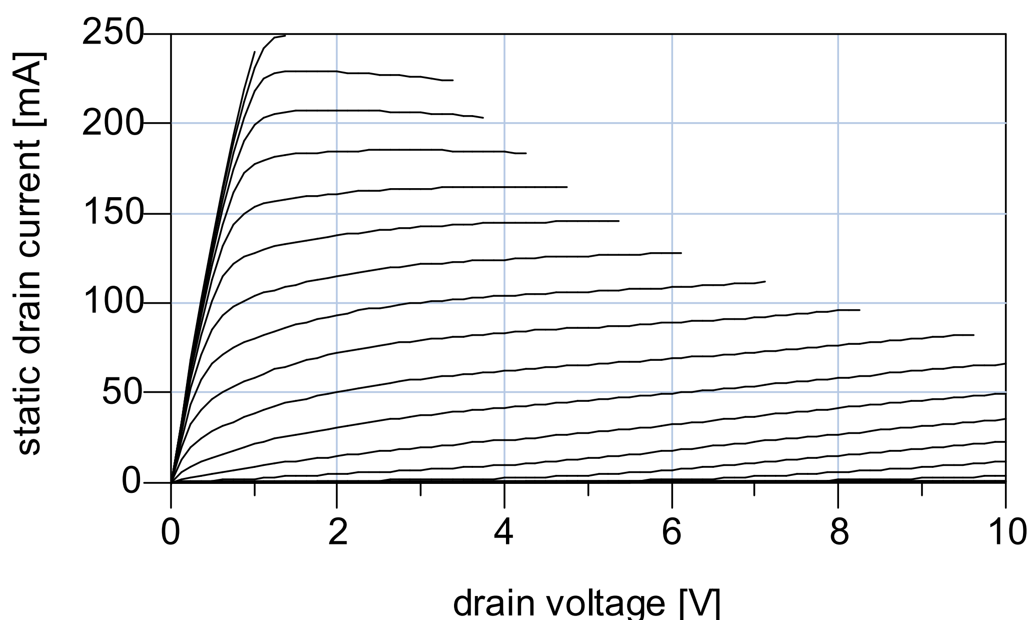

Fig. 1.4: Static drain current measurements of a 0.25-µm Triquint GaAs PHEMT with V_{g0} [-1.5; 0.5] step 0.1 V.

Important information on the device can be also obtained by the derivative of the current-voltage characteristic, that is from the output conductance and the transconductance, defined as

$$g_{ds} = \frac{1}{r_{ds}} = \left.\frac{\partial I_{ds}}{\partial V_{ds}}\right|_{V_{gs}=constant} \quad (1.1)$$

$$g_m = \left.\frac{\partial I_{ds}}{\partial V_{gs}}\right|_{V_{ds}=constant} \quad (1.2)$$

respectively. The output conductance plays an important role in determining the maximum voltage gain obtainable from the device and in determining the optimum output matching conditions: in general, a low value of the output conductance is desirable for a good device. On the contrary, the highest is the transconductance, the best are the gains and the high-frequency device performances. Both conductance are, of course, affected by device dimensions and channel material properties.

Finally, it must be observed that the charge distribution in the channel, that is the shape of the depletion region, is determined by both the gate-drain and gate-source potential. This leads to define two important capacitances:

$$C_{gs} = \left.\frac{dQ_g}{dV_{gs}}\right|_{V_{ds}=constant} \quad (1.3)$$

$$C_{gd} = \left.\frac{dQ_g}{dV_{gd}}\right|_{V_{gs}=constant} \quad (1.4)$$

where Q_g is the charge in the depletion region, shared between gate-source and gate-drain capacitance. The gate-source capacitance has a significant impact on the input impedance and on the high frequency performance: in fact, at a high enough frequency this capacitance becomes nearly a short circuit and in these conditions the device does not produce useful gain. Thus, a low value of the gate-source capacitance increases the maximum operative frequency. The gate-drain capacitance is mainly responsible of the reverse isolation of the device, thus a low value is desirable too. The two capacitance values are strongly affected by the gate dimensions: they are directly proportional to the gate width, while they do not scale strictly linearly with the gate-length.

1.2.1 GaN HEMT device

GaN- based transistors have greatly evolved since their first demonstration in 1993 [2]. In less than 15 years, they have developed from device with less than 20 mA mm^{-1} of output current and virtually no high-frequency performance, to world-wide commercialization as power amplifiers at high frequencies. Device with maximum drain current densities of 2 A mm^{-1} and a critical breakdown electric field of 3MV cm^{-1} are fabricated. Fig. 1.5 shows an example of cross-sectional view of a GaN HEMT device.

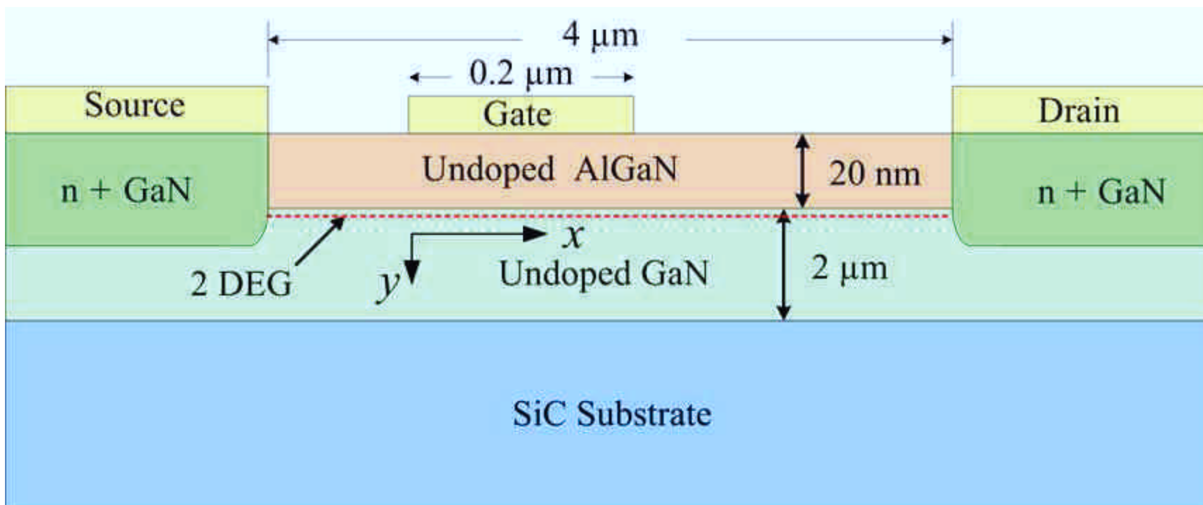

Fig. 1.5 Cross section of a basic GaN-on-silicon high electron mobility transistor (HEMT)

This structure consists of a 2 µm thick GaN buffer layer overgrown with nominally undoped 20 nm AlGaN layer. The source and drain contacts are ohmic, whereas the gate is composed of a Schottky barrier with gold as the gate material. Ohmic contacts for the source and the drain are made of n^+ GaN and gold. Due to the bandgap difference between AlGaN and GaN a potential well is formed in the GaN layer at the interface. The spontaneous polarization and the piezoelectric polarization due to lattice mismatch between Al-GaN and GaN create positive sheet charges in AlGaN at the heterointerface. Larger gate-drain separation is provided to achieve high breakdown voltage. Fig 1.6 show the band diagram of the Al-GaN/GaN and GaN/SiC heterointerface. Due to the positive sheet charges, electrons appear and remain confined in the potential well forming the 2-DEG [3]. In AlGaN/GaN HEMTs, the 2-DEG conduction channel exists even with zero gate bias. The concentration of

the 2-DEG in the channel can be modulated by varying the voltage applied at the external gate terminal.

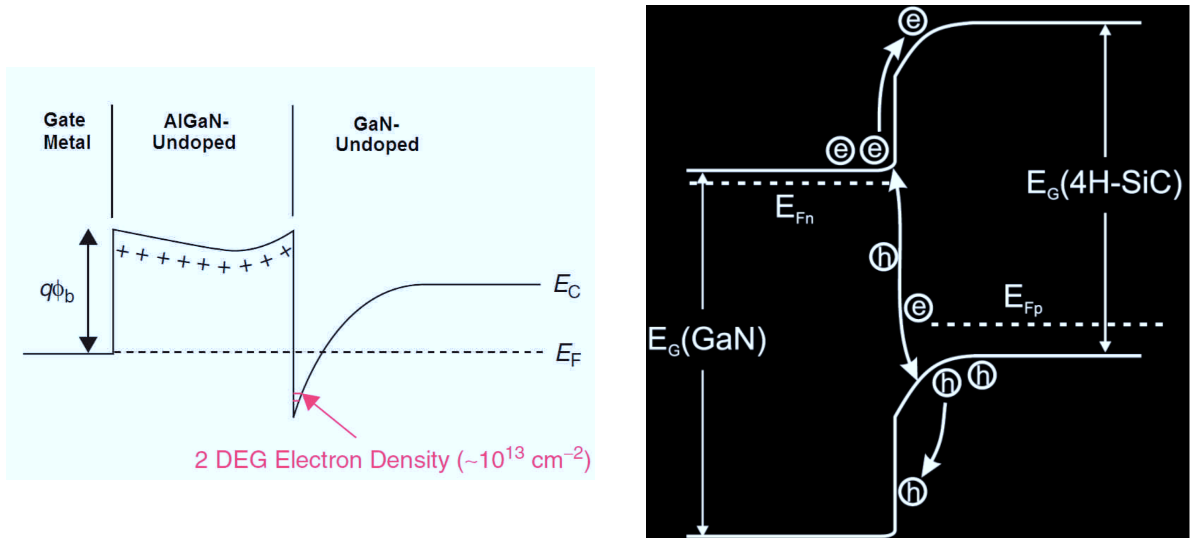

Fig. 1.6 a) Conduction band edge at AlGaN/GaN heterointerface showing quantum well and 2DEG. b) band diagram of a GaN/SiC heterojunction, where the injection process and the tunneling assisted recombination process have been indicated with arrows

Static drain current characteristic, measured for a 0.25 μm GaN HEMT, is shown in Fig 1.7. It can be noticed that the current level and bias voltage reached are larger compared to a GaAs device with the same periphery.

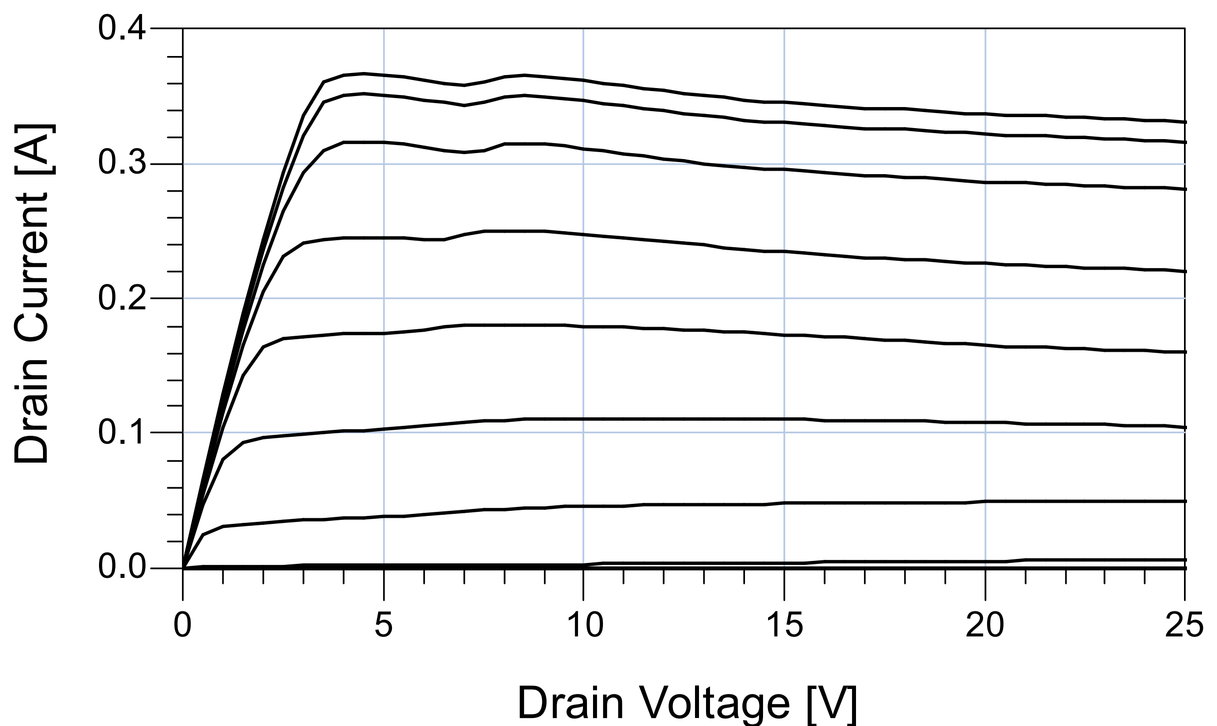

Fig. 1.7: Static drain current measurements of a 0.25-μm GaN HEMT with V_{g0} [-8; 0] step 0.5 V.

AlGaN/GaN HEMT device performance demonstrates power densities of 6-9 W mm^{-1} [4-6] , about one order improvement over conventional HEMTs.

1.3 Low frequency dispersion effect

Important issues related to III-V field effect devices are the low frequency dispersion effects. These phenomena are related to thermal effects, such as self-heating, and to the presence of electronic traps in the device structure. Both in GaAs and in AlGaN/GaN HEMTs, the parasitic charge moving in and out of the traps, on the surface and/or in the bulk of the heterostructure, affects the density of the two-dimensional electron gas (2DEG) in the channel, causing effects such as current collapse [7-9], drain lag [10-11], gate and light sensitivity [9] and output conductance and transconductance frequency dispersion [12,13,14]. The time constants associated to the recharging process depend strongly on the technology: they range around microseconds for GaAs devices and from nanoseconds up to seconds in GaN devices, although for the GaN, discussion on the importance of this time constant is still an open issue. As a result, the trapping effects can limit device performance even at relatively low frequencies. In addition, the thermal state of device can influence the trap status thereby making the problem even more complicated. Thermally activated traps further contribute significantly to the device low-frequency noise [15,16].

The electrical evidence of trapping effects can be seen by observing the frequency dependence of the transconductance and output conductance. In Fig. 1.8 transconductance frequency dependence of a GaAs HEMT device is reported.

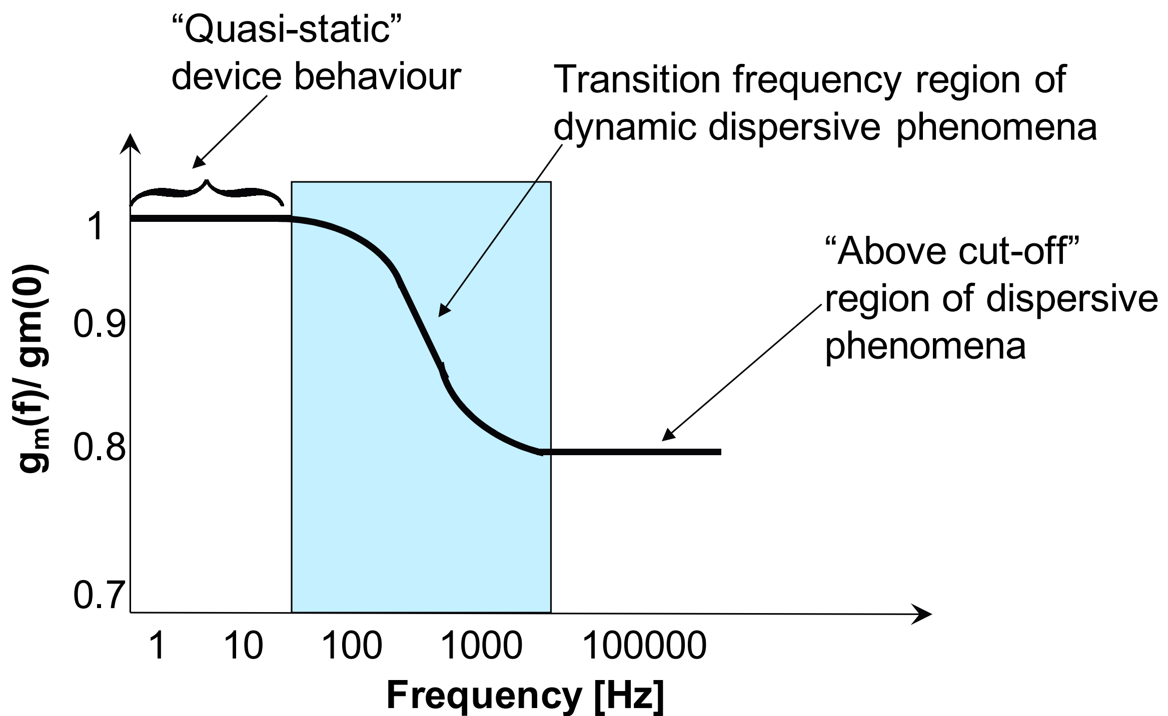

Fig. 1.8 Dispersive dynamic behavior of GaAs electron devices.

As it can be seen the frequency shift happens passing from few hertz to some hundreds of kilohertz; for higher frequencies the transconductance value remains constant until high frequency reactive phenomena do not occur. This is simply due to the fact that the deep level occupation state for low-frequency signal is able to change according to the signal "speed", while at higher frequencies it remains *frozen* and is not capable of further following signal frequency change. From Fig. 1.8 we can say that the dispersion has a cut-off frequency between 100 kHz and 1 MHz (for GaAs FETs).

Many papers deal with the issue of low frequency dispersion for GaN devices. Someone [17] argue that there are very short time constants and therefore the settling of the output conductance happens at higher frequency with respect to GaAs. On the other hand, other papers [18] assume that frequencies in the neighbourhood of hundreds of kHz are sufficient to characterize the dispersive phenomena in GaN, because changes for higher frequencies can be neglected.

Fig 1.9 a) and b) show the output conductance frequency dependence for the GaN technology used in this thesis. Measurements were carried out on 0.25 μm GaN HEMT device. As it can be clearly noticed there are little changes in the output conductance from 1 MHz up to 40 MHz . These variations, when compared with the

DC value, appear to be negligible, actually placing the cut-off frequency of dispersive phenomena of the GaN device to values similar to those of GaAs, according to [18].

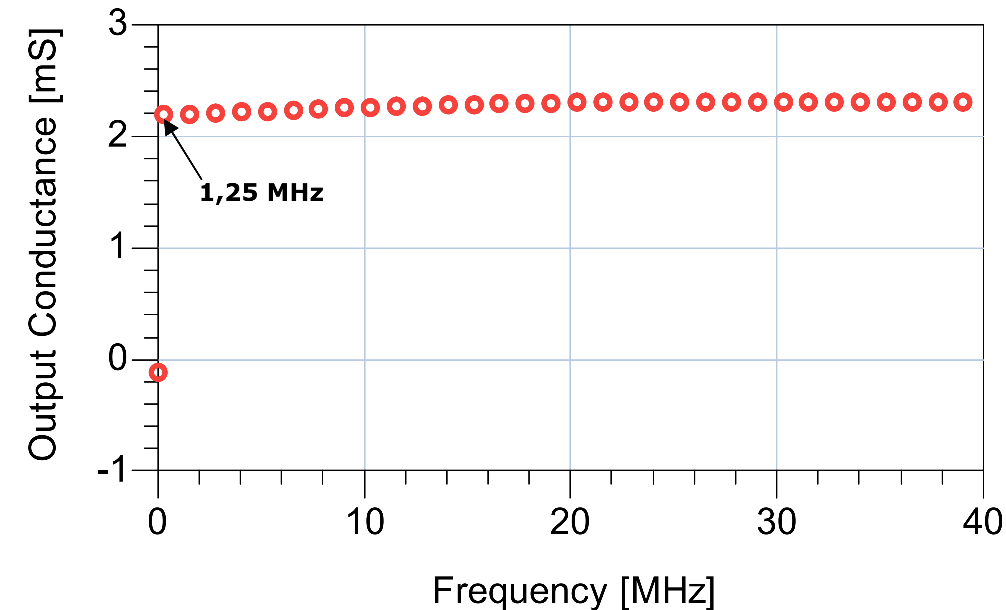

a)

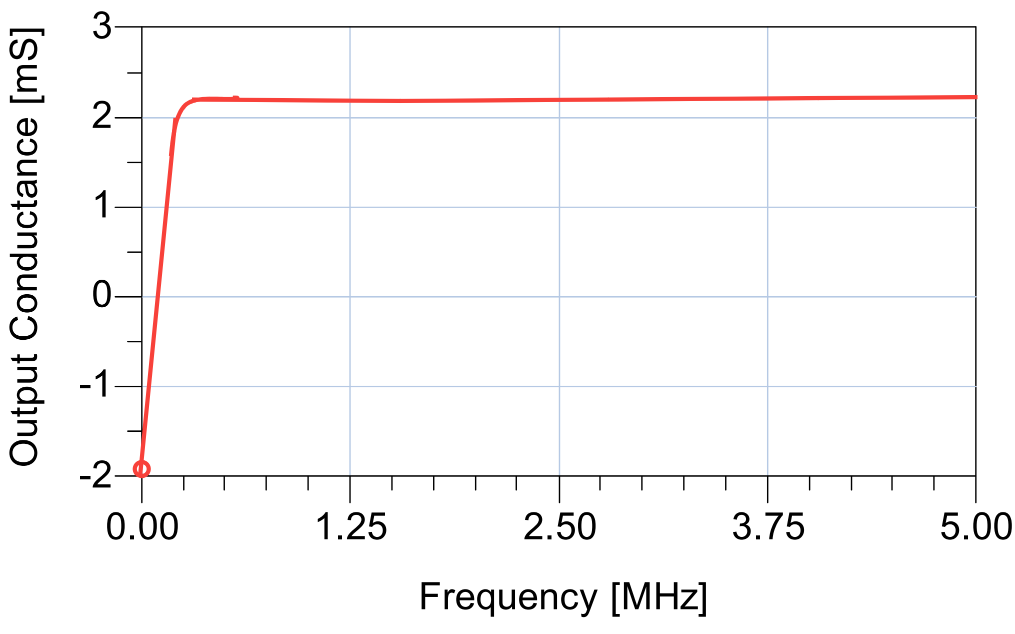

b)

Fig 1.9: a) Output Conductance of 0.25 um GaN HEMT device for V_{g0} = -3 V, V_{d0} = 20 V. b) Zoom of the same characteristics

The presence of dispersive phenomena results in a deviation between the static and the low-frequency device behaviour. Fig. 1.10 compares static and dynamic characteristics of a GaN HEMT device starting from two different bias conditions corresponding to class A and class AB amplifier operation. Dynamic measurements were carried out by exploiting a pulsed I/V measurement system which allows to

measure the drain current characteristics leaving unchanged the average values of the electrical variables at the device ports. This implies, for example, that in all the measured points the device thermal condition coincides with its static condition. Changing the electron device bias condition also implies different thermal and trapping states.

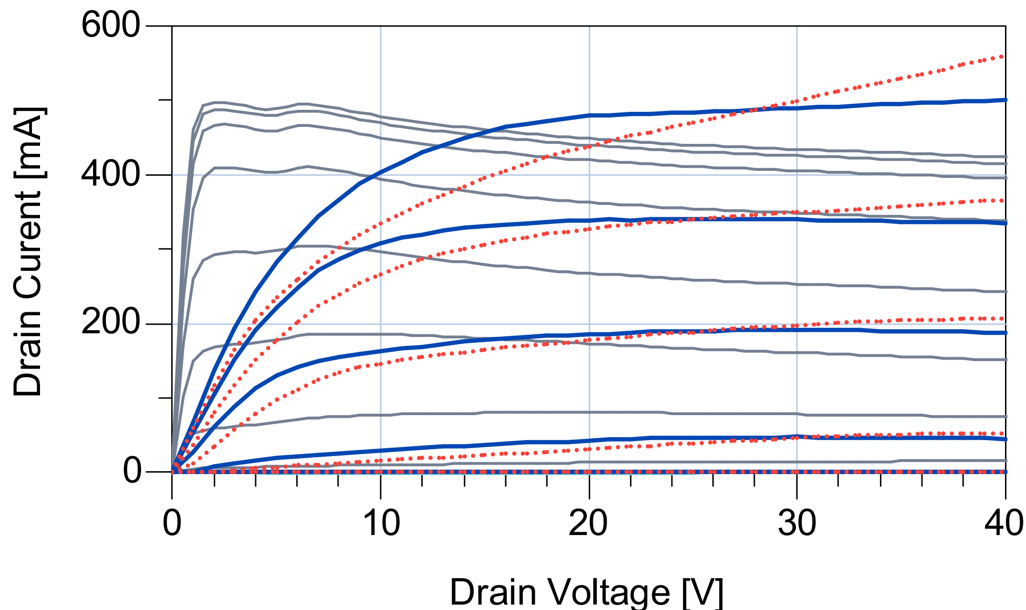

Fig 1.10: Pulsed drain current characteristics of a 0.25-μm GaN HEMT starting from two different bias conditions: V_{g0} = -3 V , V_{d0} = 35 V (red lines) and V_{g0} = -2 V , V_{d0} = 25 V, versus static drain current characteristics (grey lines).

As an understood matter of fact, accurate modelling of low-frequency dispersive effects is fundamental to obtain good prediction capabilities of device behaviour in microwave large signal operation.

As for every new technology process, the GaN one is strongly affected by dispersive phenomena. For example, drain current collapse in GaN HEMT device can reach up to 70% of the maximum drain current. In recent years, a great progress has been made in the development of high performance AlGaN/GaN high electron mobility transistors but still much work must be done. More considerations on this topic will be provided in chapter 2, where the impact of dispersion phenomena on device performance has been clearly documented.

1.4 Non linear modeling

Models for active devices belong to two categories: physical and empirical models. Physical models describe the device in terms of its physical structure and parameters and predict its behaviour by means of electromagnetic and charge transport equations. The most important advantage is that the behaviour of device can be predicted without fabricate the device itself. This kind of modeling is useful to device designers. Empirical models are extracted from data measured on the fabricated device. They may include some knowledge of the physical structure of the device and they are usually referred as equivalent-circuit models, or they may be a powerful and flexible extrapolating/interpolating scheme, and referred as black-box models.
Empirical models are the best solution for accurate CAD simulations of non linear circuits. The work done for a exhaustive characterization of the device pays for itself with great flexibility and accuracy in CAD applications. Equivalent- circuit models are the most successful empirical models for CAD application. Many equivalent circuits models are available in literature for microwave devices; an example of equivalent circuit representation for a FET large signal model is shown in Fig. 1.11.

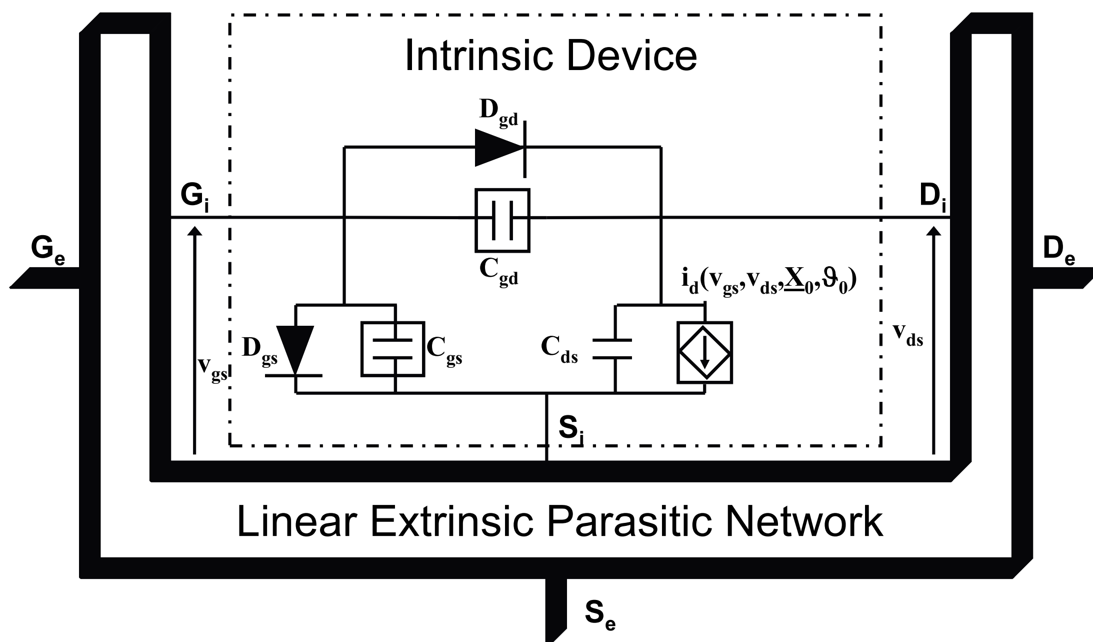

Fig. 1.11 An equivalent circuit representation for a FET nonlinear model.

The linear extrinsic parasitic network in Fig. 1.11 describes the access passive structure to the device active area and accounts for metallization and dielectric

losses, as well as for associated inductive and capacitive effects. Its correct modeling is a fundamental issue to obtain accurate model predictions. Parasitic elements can be characterized by exploiting conventional lumped descriptions [19,20], which can be identified by only using small-signal measurements, or, alternatively, by adopting electromagnetic simulations of the device layout [21,22]. Once parasitic de-embedding has been carried out, the intrinsic device results accessible.

As clearly shown in Fig. 1.12, the intrinsic device of Fig. 1.11 can be divided into two parts, which can be considered strictly in parallel: a *capacitive core* describing the nonlinear dynamic phenomena, and a *resistive* core accounting for the dc and LF I/V device characteristics.

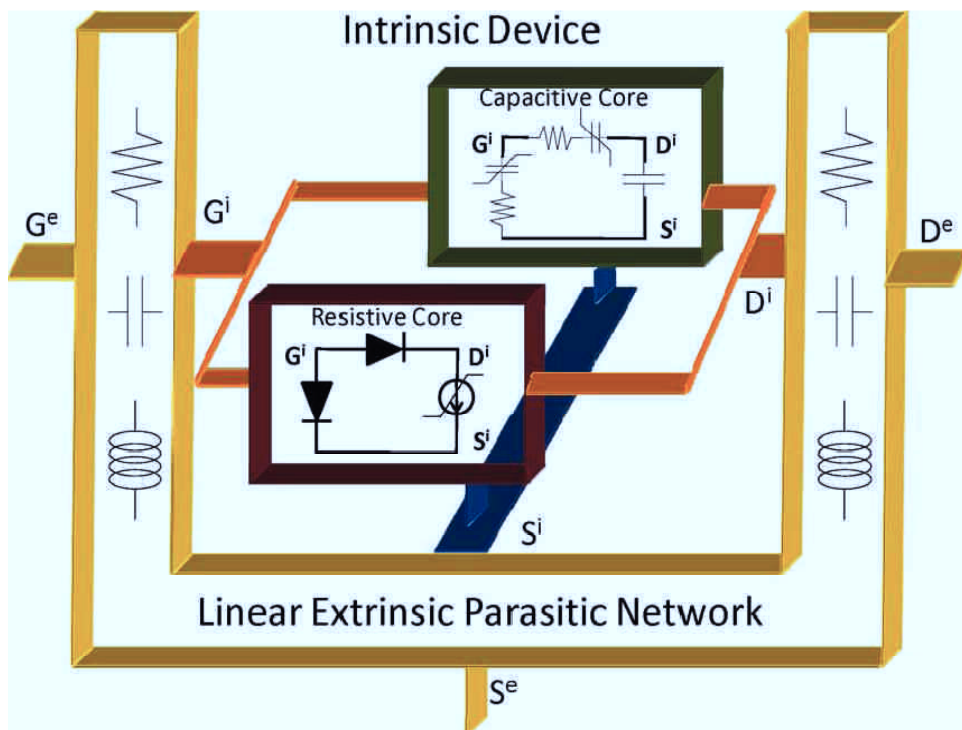

Fig. 1.12: Nonlinear equivalent circuit for an FET Electron Device.

The nonlinear capacitances of *capacitive core* are only C_{gs} and C_{gd} which describe how the depletion region charge beneath the gate is affected by the gate-source potential and the gate drain potential. The drain-source capacitance C_{ds} is included in the equivalent circuit to account for geometric capacitance effects between the source and drain electrodes. It is usually not considered to be bias dependent for the purposes of device modelling.

LF I/V device characteristics, that can be obtained from the *resistive core*, differ from the dc response due to surface state densities, deep-level traps, and thermal phenomena, extensively discussed previously. More rigorously, a dynamic term should also be considered for the LF device behaviour, but the most commonly adopted equivalent-circuit models do not accurately model such dynamics and accounts only for device response at dc and above the trap cut-off frequency.

The electron device *resistive core* modeling is extremely complex, not only because a number of important nonlinear phenomena must be considered (e.g., breakdown, forward conduction of the gate–source diode, knee of the I/V curves, etc.), but also due to the non negligible presence of dispersive effects [23-27], which impose the exploitation of nonlinear dynamic measurements in order to obtain good prediction capabilities. Several approaches were proposed by the research community with difference in terms of accuracy and efficiency. In chapter 4 a new approach developed during this PhD thesis will be presented.

References

[1] R. J. Trew "Wide Bandgap semiconductors. Transistor for microwave power amplifier". Microwawe Magazine; March 2000

[2] M. Asif Khan, A. Bhattarai, J. N. Kuznia, and D. T. Olson "High electron mobility transistor based on a GaN-Al_x,Ga_{1-x},N heterojunction", Appl. Phys. Lett. 63, pp.1214-15 (1993)

[3] Ambacher O, Smart J, Shealy JR, Weimann NG, Chu K, Murphy M, et al. "Two-dimensional electron gases induced by spontaneous and piezoelectric polarization charges in N- and Ga-face AlGaN/GaN heterostructures". J Appl Phys 1999;85(6):3222–33.

[4] S. Keller, Y.-F. Wu, G. Parish, N. Zhang, J. J. Xu, B. P. Keller, S. P. DenBaars, and U. K. Mishra, "Gallium nitride based high power heterojunction field effect transistor: Process development and present status at UCSB," *IEEE Trans. Electron Devices*, vol. 48, pp. 552–559, Mar. 2001.

[5] S. T. Sheppard, K. Doverspike, W. L. Pribble, S. T. Allen, and J. W. Palmour, "High power microwave GaN/AlGaN HEMTs on silicon carbide," *IEEE Electron Device Lett.*, vol. 20, pp. 161–163, Apr. 1999.

[6] Y.-F.Wu, D. Kapolnek, J. P. Ibbetson, P. Parikh, B. P. Keller, and U. K. Mishra, "Very-high power density AlGaN/GaN HEMTs," *IEEE Trans. Electron Devices*, vol. 48, pp. 586–590, Mar. 2001

[7] M.A. Khan, M.S. Shur, Q.C. Chen, J.N. Kuznia, "Current/voltage characteristic collapse in AlGaN/GaN heterostructure insulated gate field effect transistors at high drain bias", Electron. Lett. 30 (1994) 2175.

[8] P.B. Klein, J.A. Freitas Jr., S.C. Binari,A.E.Wickenden, "Observation of deep traps responsible for current collapse InGaN metal–semiconductor field-effect transistors", Appl. Phys. Lett. 75 (1999) 4014.

[9] S.C. Binari, et al., "Fabrication and characterization of GaN FET's", Solid-State Electron. 41 (1997) 1549–1554.

[10] S.C. Binari, J.M. Redwing, G. Kelner, W. Kruppa, "AlGaN/GaN HEMT's grown on SiC substrates", Electron. Lett. 33 (1997) 242–243.

[11] S. Trassaert, et al., "Trap effects studies in GaN MESFET's by pulsed measurements", Electron. Lett. 34 (1999) 1386–1388

[12] W. Kruppa, S.C. Binari, K. Doverspike, "Low-frequency dispersion characteristics of GaN HFETs", Electron. Lett. 31 (1995) 1951.

[13] I. Daumiller, D. Theron, C. Gaquiere, A. Vescan, R. Dietrich, A. Wieszt, H. Leier, R. Vetury, U.K. Mishra, I.P. Smorchkova, S. Keller, N.X. Nguyen, C.N. Nguyen, E. Kohn, "Current instabilities in GaN-based devices", IEEE Electron. Dev. Lett. 22 (2001) 62.

[14] A. Raffo, V. Vadalà, D. M. M.-P. Schreurs, G. Crupi, G. Avolio, A. Caddemi, G. Vannini, “Nonlinear Dispersive Modeling of Electron Devices Oriented to GaN Power Amplifier Design” Accepted on IEEE Trans. Microw. Theory Tech.

[15] D.V. Kuksenkov, H. Temkin, R. Gaska, J.W. Yang, “Low-frequency noise in AlGaN/GaN heterostructure field effect transistors”, IEEE Electron. Dev. Lett. 19 (1998) 222.

[16] S.L. Rumyantsev, N. Pala, M.S. Shur, E. Borovitskaya, A.P. Dmitriev, M.E. Levinshtein, R. Gaska, M.A. Khan, J. Yang, X. Hu, G. Simin, “Generation-recombination noise in GaN/AlGaN heterostructure field effect transistors”, IEEE Trans. Electron. Dev. 48 (2001) 530.

[17] F. De Groote, J.-P. Teyssier, O. Jardel, T. Gasseling, J. Verspecht, “Introduction to measurements for power transistor characterization,” IEEE Microwave Mag., vol. 9, no. 3, pp. 70–85, Jun. 2008.

[18] W. Ciccognani, F. Giannini, E. Limiti, P.E. Longhi, M.A. Nanni, A. Serino, C. Lanzieri, M. Peroni, P. Romanini, V. Camarchia, M. Pirola, G. Ghione, “GaN Device Technology: Manufacturing, Characterization, Modelling and Verification,” in Proc. IEEE 14th Conference on Microwave Techniques, Prague, 2008, pp. 1–6.

[19] G. Dambrine, A. Cappy, F. Heliodore, and E. Playez, “A new method for determining the FET small-signal equivalent circuit,” IEEE Trans. Microw. Theory Tech., vol. 36, no. 7, pp. 1151–1159, Jul. 1988.

[20] N. Rorsman, M. Garcia, C. Karlsson, and H. Zirath, “Accurate small signal modeling of HFET’s for millimeter-wave applications,” IEEE Trans. Microw. Theory Tech., vol. 44, no. 3, pp. 432–437, Mar. 1996.

[21] B. Cetiner,R. Coccioli, B. Housmand, and T. Itoh, “Combination of circuit and full wave analysis for pre-matched multifinger FET,” in Proc. 30th Eur. Microw. Conf., Paris, France, 2000, pp. 1–4.

[22] D. Resca, A. Santarelli, A. Raffo, R. Cignani, G. Vannini, F. Filicori, and D. M. M.-P. Schreurs, “Scalable nonlinear FET model based on a distributed parasitic network description,” IEEE Trans. Microw. Theory Tech., vol. 56, no. 4, pp. 755–766, Apr. 2008.

[23] A. Raffo, A. Santarelli, P. A. Traverso, M. Pagani, F. Palomba, F. Scappaviva, G. Vannini, and F. Filicori, “Accurate pHEMT nonlinear modeling in the presence of low-frequency dispersive effects,” IEEE Trans. Microw. Theory Tech., vol. 53, no. 11, pp. 3449–3459, Nov. 2005.

[24] A. Raffo, V. Vadalà, G. Vannini, and A. Santarelli, “A new empirical model for the characterization of low-frequency dispersive effects in FET electron devices accounting for thermal influence on the trapping state,” in IEEE MTT-S Int. Microw. Symp. Dig., Atlanta, GA, 2008, pp. 1421–1424.

[25] W. Struble, S. L. G. Chu, M. J. Schindler, Y. Tajima, and J. Huang, “Modeling intermodulation distortion in GaAs MESFETs using pulsed I–V characteristics,” in Proc. GaAs IC Symp., Monterey, CA, 1991, pp. 179–182.

[26] T. Roh, Y. Kim, Y. Suh, W. Park, and B. Kim, “A simple and accurate MESFET channel-current model including bias-dependent dispersion and thermal phenomena,” IEEE Trans. Microw. Theory Tech., vol. 45, no. 8, pp. 1252–1255, Aug. 1997.

[27] C. Camacho-Penalosa, “Modeling frequency dependence of output impedance of a microwave MESFET at low frequencies,” Electron. Lett., vol. 21, no. 12, pp. 528–529, Jun. 1985.

CHAPTER II :

Non-Linear Measurement Systems for LF Dispersion Characterization and Modelling

Introduction

In the telecommunication industry, amplifiers are indispensable components and they get the best performance when working under non-linear regime. Understanding and characterizing the nonlinear behavior of electron devices and circuits is a very important task in the context of microwave circuits, in order to obtain increasingly accurate models of the devices to be used in high-performance amplifier design. In this context, non linear measurements represent a powerful aid, although all those systems are complex and expensive.

Large-signal measurement systems are used to characterize the non linear dynamic behaviour of electron devices. As a matter of fact, nonlinear setups allow to experimentally evaluate device and circuit performance under actual operation. The experimental data gathered by adopting such a kind of setups have been largely and successfully adopted by the microwave community not only to identify the optimum device operating conditions but also to extract and validate different device models. Moreover, nonlinear measurement systems are able to highlight particular phenomena such as low frequency dispersive effects, harmonic distortion and reliability issues (e.g., power slump, breakdown walkout).

The most important non linear microwave measurement systems will be discussed in this chapter: pulsed, load / source-pull, and Large Signal Network Analyzer

measurement systems. These setups are all quite expensive and complex to use but provide very useful information that otherwise would not be found easily.

2.1 Pulsed measurements

Pulsed measurement systems are used both for characterization of dispersive effects and for their modeling. This type of setup allows to plot device output characteristics similar to those in DC, but with very specific properties: for every bias point a "set" of isothermal and isodynamic I-V characteristics can be obtained. Fig. 2.1 shows a schematic diagram of a pulsed measurement system.

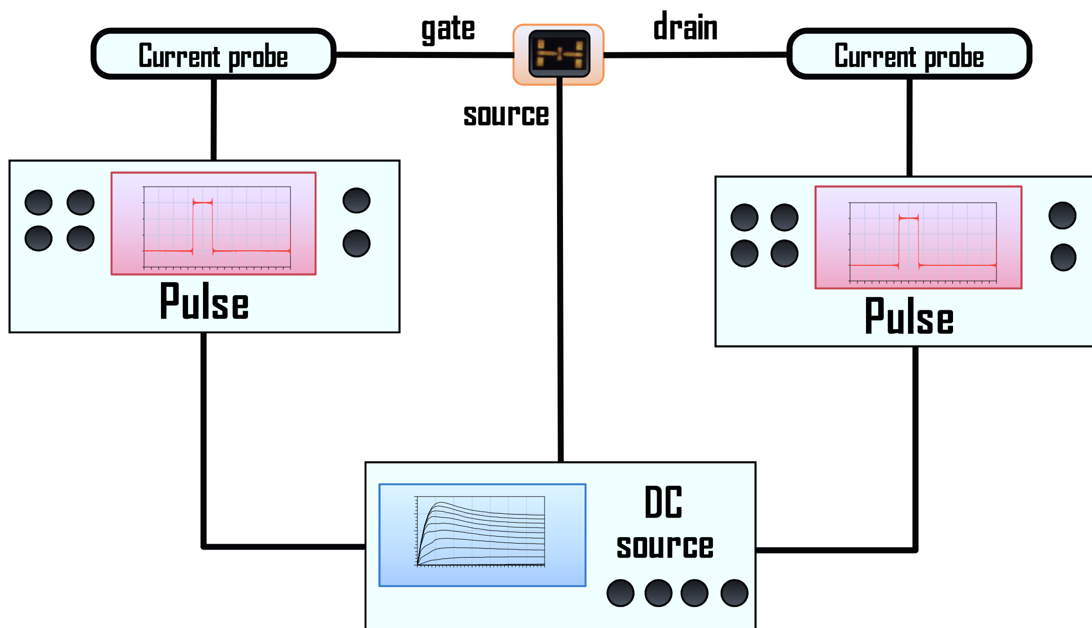

Fig. 2.1 Measurement setup used to carry out pulsed measurements.

This setup is based on the application of short voltage pulses (both positive and negative) superimposed on fixed DC levels. The pulse amplitude varies from small to large amplitudes so every bias condition can be reached dynamically. A critical issue in time definition of pulse measurements is related to the pulse period, that must be large enough to guarantee adequately little duty cycle to allow isothermal data acquisitions, buy also quite small to ensure that acquisition time doesn't become too long. Typically the pulse width is chosen sufficiently short so that self heating (arising from the dynamic bias conditions) does not alter the device electrical characteristics and LF dispersion effects can be considered as frozen. In addition, pulsed

characterization may allow for separation of charge trapping effects from thermal effects in electron devices. Starting from different bias conditions, but with the same power dissipation (and hence same thermal status), and maintaining the same time property of pulses, different I-V characteristic sets are obtained. Changes in these characteristics may be attributed to trap effects related to bias conditions (for example strong and soft pinch-off bias have very different trap status). An example of this capability of pulsed measurement systems is shown in Fig. 2.2, where two different measurement sets were obtained starting from two different bias conditions with the same dissipated power. Furthermore, by varying the pulse duration, the thermal condition of the device is changed; for instance, an increase of pulse duration causes a channel temperature rise and, for a FET device, the current levels decrease until they reaches the DC values. Properly set the timing of pulse measurements depends on devices and technologies. Many papers [1,2,3] deal with the choice of the correct setting of these parameters. For GaAs devices there is more confidence on timing; instead on GaN devices the situation is a little bit controversial although 500 us period and 500ns pulse width are deemed acceptable in most papers [4].

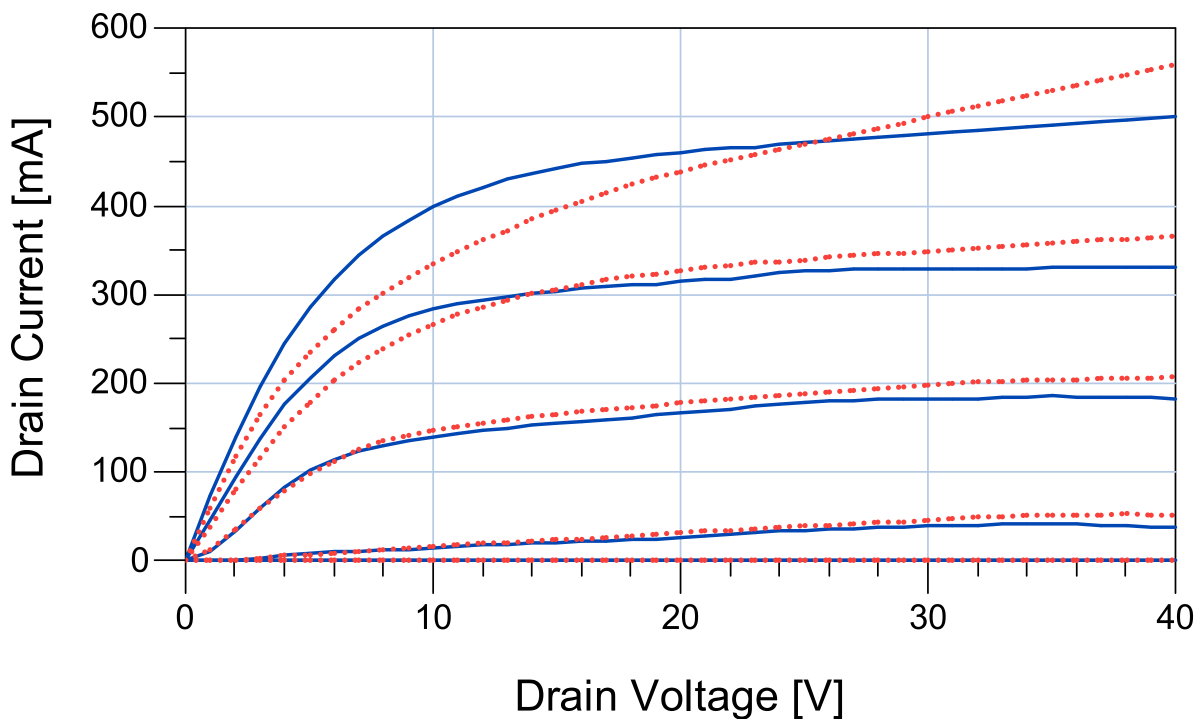

Fig 2.2 Pulsed drain current characteristics of a 0.25-μm GaN HEMT starting from two different bias condition with the same dissipated power: V_{g0} = -7 V , V_{d0} = 16 V (blue continues lines) and V_{g0} = -7 V , V_{d0} = 30 V (red dotted lines).

Pulsed setups have been widely used [5,6] to perform a device breakdown characterization under LS operating conditions; in fact a device biased so that DC avalanche is taking place is not approximating the device behavior during normal operating conditions. Pulsed setups provide for a breakdown characterization in a more realistic situation where device is biased under operating conditions well below the voltage levels needed to cause avalanche breakdown.

As previously said, pulsed measurements are largely exploited for non linear modeling of microwave electron devices. A first attempt to model frequency dispersion by using pulsed measurements was proposed by W. Struble et al. [7]. It was suggested to simply make use of a pulsed I/V characteristic from the desired DC operating point in order to model the dominant drain current nonlinearity. This LF modelling approach, in conjunction with a Materka-like description of the dynamic nonlinearities, was successfully used to predict MESFET device intermodulation distortion. The problem of this approach is that the model coincides with an isothermal measurement, completely neglecting that under actual operating conditions the thermal state is not established by the bias but also depends on the average value of applied signals (i.e., how much power is actually dissipated on the device and how much delivered to the load). This type of approach is a good choice only when the average dynamic power is similar to the static one (e.g., highly linear power amplifiers).

In order to obtain more accurate prediction capabilities, different models have successively been presented by T.M. Roh et al. in [8] and by by A.E. Parker and D.E. Root [9,10,11,12]. Some of the work of this thesis was devoted to the development of a new model for dispersive effects, described in details in chapter 4.

2.2 Load Pull measurements

A widely used characterization technique for microwave devices is the load/source-pull measurement. It allows to test transistors under actual large-signal operating conditions by imposing at the ports of the device under test (DUT) arbitrary terminations. This kind of measurements can be used directly for the design of power amplifier (PA) by exploiting the system capability of obtaining useful information about the optimal load condition for a specific device. The data obtained from load-pull systems can also be used to verify large-signal models, although they are not

suitable for use in large-signal model extraction phase, since computing-intensive non-linear optimisation in conjunction with HB simulations would be required. For wideband characterization, load-pull measurements can be taken at several frequencies within the band of interest. Current measurement systems are able to control fundamental frequencies up to 110 GHz.

For some applications, such as high-efficiency amplifiers design, it is useful to control a number of harmonics, an expensive feature for such an equipment.

Load-Pull measurement systems can be divided into two categories: active and passive ones. In both cases, it is possible to control the load either at the fundamental frequency or at harmonics. Traditional passive load pull systems use mechanical or electrical tuners, controlled by automated servomotors, to achieve the required load or source impedance. In active load-pull systems the impedance at the input and output ports is set by exploiting two phase- and amplitude-controlled RF signal generators. Fig. 2.2 shows a block diagram of a passive load-pull measurement system.

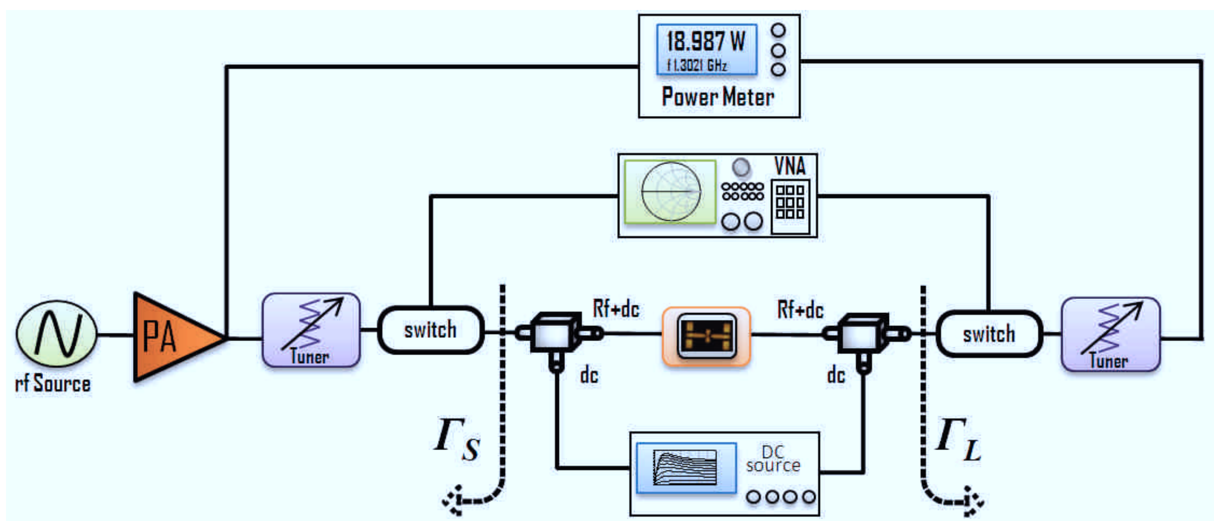

Fig. 2.2 Typical configuration of Load/source- pull passive measurement system

The input signal is sampled by a directional coupler and then measured by a power meter. The input tuner is used to optimize the input match and to assure the maximum power delivery to the device. The reflection coefficient Γ_S, that is the actual source impedance, can be set to any desired value within a certain region of the Smith chart. At the output port another tuner allows to set Γ_L; after the output tuner the signal is fed to a power meter. DC bias is supplied through the bias tees.

Before carrying out measurements, the load-pull system needs a calibration for each desired frequency. Obviously more complex systems, such as those with harmonic control, need increasingly critical calibration. The calibration of the setup is carried out through a VNA: all parts in the setup must be characterized in terms of two ports S-parameters in order to properly evaluate impedance and power levels at the DUT ports. The power level is calibrated by a power meter measurement with the DUT replaced by a through connection.

After calibration, a standard de-embedding technique can be used to calculate the correct quantities. Information obtained from the measurements are useful for tracing the *power contours* on the Smith chart, which represent a powerful tool providing information on the best performance achievable by the device. For each measured impedance a constant performance parameter (i.e. power, PAE, etc.) can be displayed as a curve on the Smith Chart. This contours are traced for one frequency at time.

An example of contours obtained by measurements carried out at different frequencies through a passive load-pull measurement system [13] is shown in fig. 2.3:

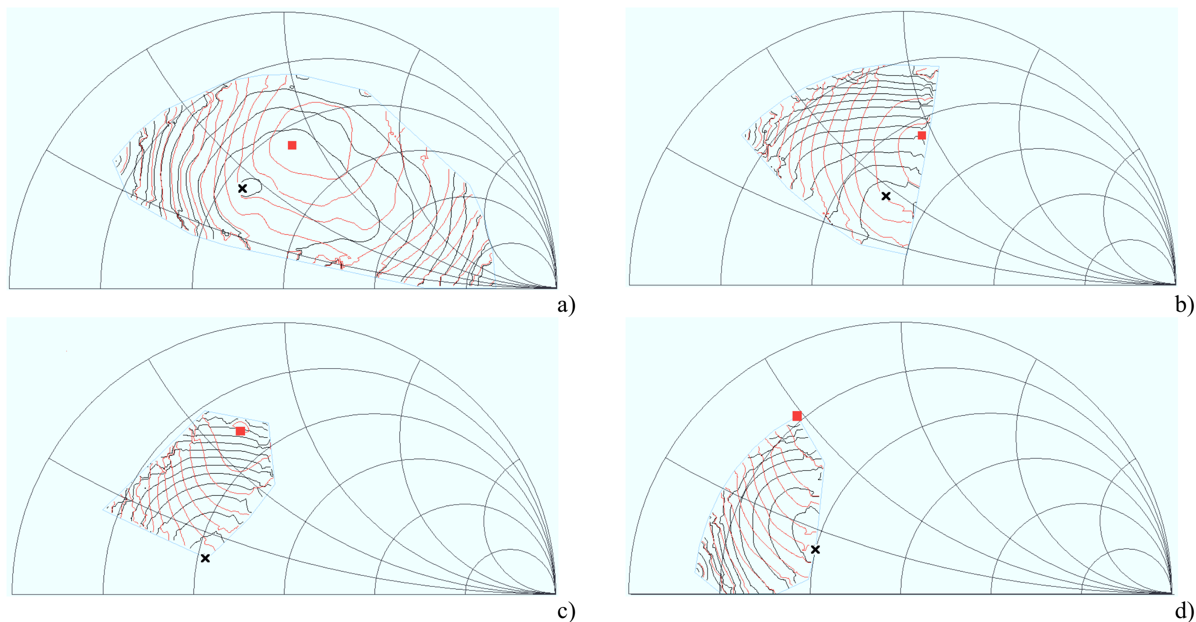

Fig. 2.3. Output-power (black) and efficiency (red) contours measured by means of a 4–26 GHz load-pull setup (at 2.5 dB gain compression) at 4 GHz a), 5 GHz b), 6 GHz c), and 7 GHz d) fundamental frequency. Best output power (cross) and best PAE (square) terminations.

Active load-pull measurement systems overcome many of the problems associated with traditional load-pull systems. The major advantage is that the load reflection coefficient obtained is not limited in amplitude. Fig 2.4 shows a diagram of an active

load/source-pull system. A large amplitude signal is provided by the RF signal generator and is divided into two signals that drive each port of the DUT. The two variable attenuators and the phase shifter control the power levels and the relative phase of the two incident waves at the input and output ports. Before the signal reaches the network analyzer bidirectional couplers, switches and filters work on lowering the power level of the signal itself to avoid damage or problems with the instrumentation. A feature which is not common to all load-pull systems is the inclusion of low-pass filters to yield the characteristic impedance to the harmonic components of the reflected waves. Isolators are used to protect sensitive components from the high power levels present. As well as for passive, calibration is also needed for the active load-pull.

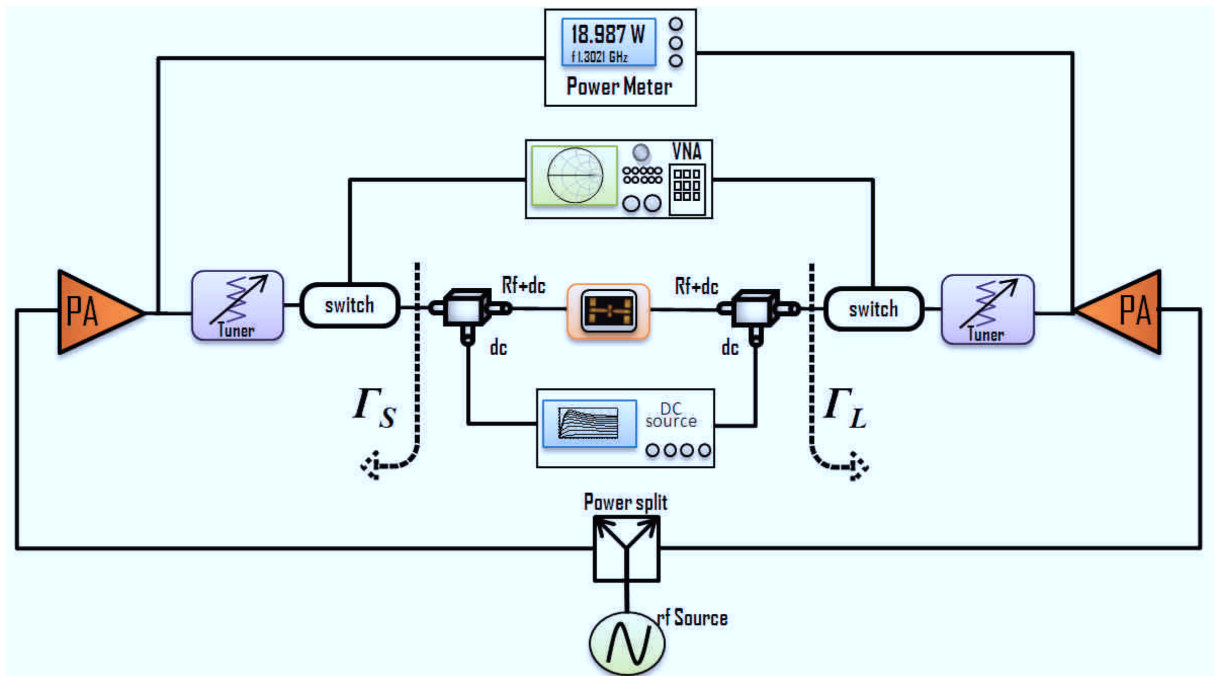

Fig. 2.4 Typical configuration of Active load/source- pull passive measurement system

Although load-pull measurement systems have been exploited for several years, the measurement equipment is still custom designed and expensive. Each system is unique, with advantages and disadvantages over other reported systems.

2.3 Large Signal Network Analyzer

Large Signal Network Analyzer (LSNA) is a powerful and complex measurement system that allows characterization of devices in non-linear condition, providing a

complete set of information on the behavior of the device that can be exploited for many applications, like transistor characterization, load-pull waveform engineering, frequency-domain modeling, state-space black-box modeling techniques, and spectral regrowth measurements. Unlike S-parameters, the LSNA works with large amplitudes of the signals applied to devices under test. S-parameters are based on the concept of superposition and can only be used to predict the behavior for a small-signal stimulus. The measured S-parameters cannot predict the behavior, for example, of the amplifier whenever the amplitude of the stimulus becomes significant compared to the operating range of the device.

LSNA has been developed to overcome the limitations of S-parameter measurements in order to provide a tool that may be used to accurately characterize nonlinear components, such as amplifiers, under large-signal excitation. This is achieved by designing instruments that can accurately and completely characterize devices under realistic large-signal operating conditions and developing software that can accurately represent the measured nonlinear device behavior in a simulator.

LSNA technology is empowered by a unique combination of two mathematical transformations. The first one is the transformation between a travelling voltage wave formalism and a voltage-current representation. The second one is the transformation between the time domain and the frequency domain. LSNA technology enables one to study the data in either domain (time or frequency) and in either representation (waves or voltage-current). Such a combination is helpful to get insights into large-signal behavior of nonlinear components. Signals can be also represented as spectra that vary over time (envelope domain). This kind of representation is useful if the signals are modulated carriers.

Fig. 2.5 shows a simplified block diagram of the hardware architecture of the LSNA. Four couplers are used for sensing the spectral components of the incident and scattered voltage waves at both DUT signal ports. The sensed signals are attenuated to an acceptable level before being sent to the input channels of a four-channel broadband RF–IF converter. This RF-IF converter operates based on the harmonic sampling principle and converts all of the spectral components coherently to a lower frequency copy (below 4 MHz). The resulting IF signals are digitized by a set of four high-performance analog-to-digital converters (ADCs). A computer does all the processing needed to transform the calibrated data into one of the three formats (AB or VI, time, frequency, or envelope domain).

The specifications of the first developed LSNA prototype are as follows: the calibrated RF frequency range is from 600 MHz to 50 GHz, the maximum RF power is 10 W, and the maximum bandwidth of the modulated signal is 8 MHz . The repetition frequency of the modulation is typically a few kilohertz. Synthesizers and tuners for the signal generation can be (and usually are) added externally. They are not considered part of the LSNA. DC bias circuitry is also present in the LSNA architecture.

Obviously a system calibration is needed to obtain the quantities of interests at the device ports. All calibration procedures are based on an *error model* based on the fact that quantities at DUT ports are related to acquired quantities by a linear relationship. Another important assumption is that no cross-coupling happens between the two ports of the LSNA. In order to identify the error model the calibration procedure needs three steps: a classical VNA calibration; an amplitude calibration; and a harmonic phase calibration.

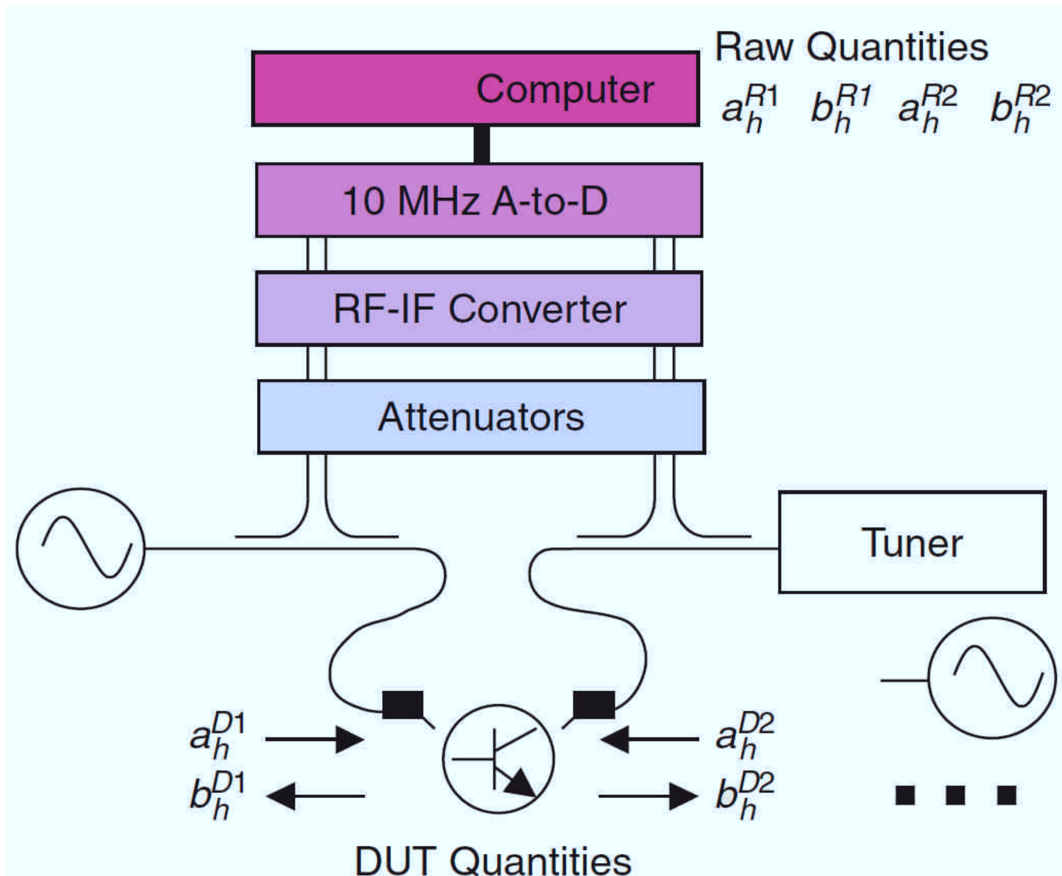

Fig. 2.5 Block diagram of a Large Signal Network Analyzer

Fig. 2.6 and 2.7 shows an example of measurements with a LSNA for power amplifier design. With waveform engineering, different harmonic impedances at the

DUT signal ports are applied, and specific performance parameters, like power-added efficiency (PAE), are optimized by looking at the voltage and current waveforms. In [14] by exploiting the combination of an LSNA with a tuner and using the waveform engineering technique for power amplifier design the authors demonstrate an increase of the PAE of a metal semiconductor FET (MESFET) Class F amplifier from 50% to 84%.

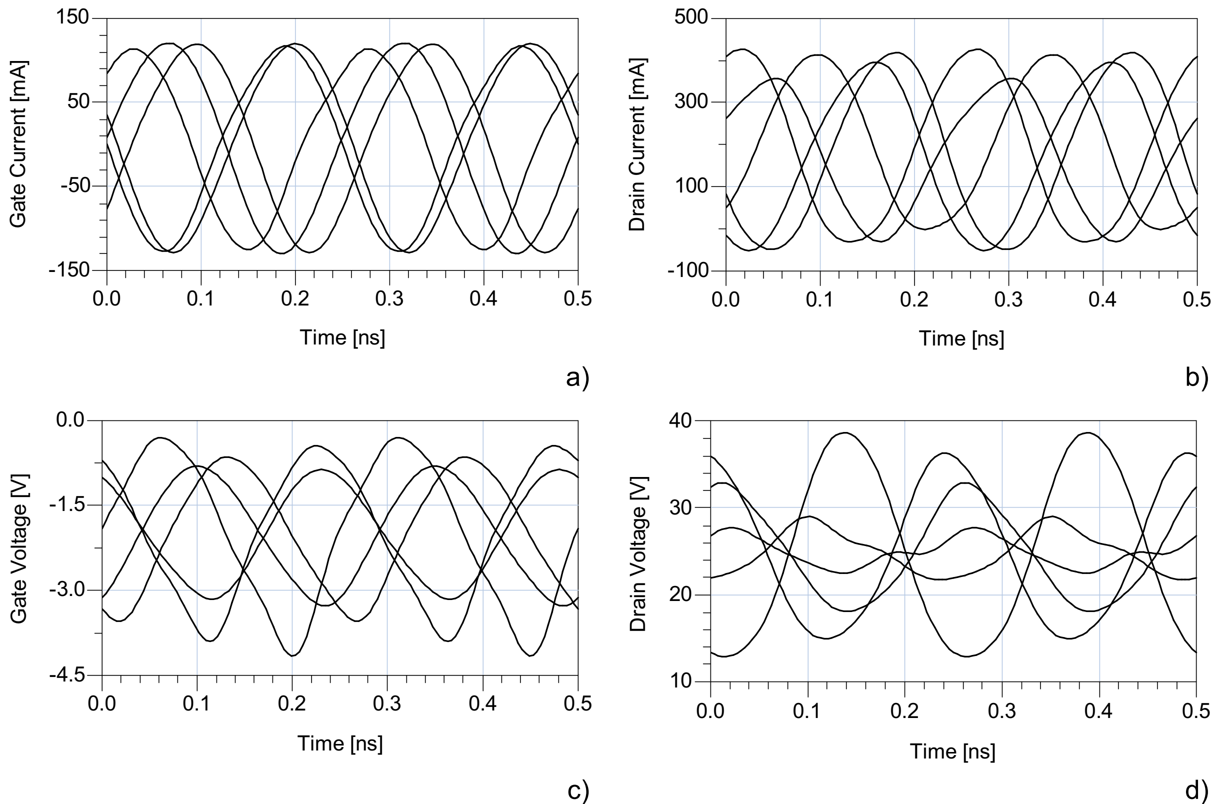

Fig 2.6 Large Signal Network Analyzer measurements. Harmonic load-pull voltage and current waveforms.

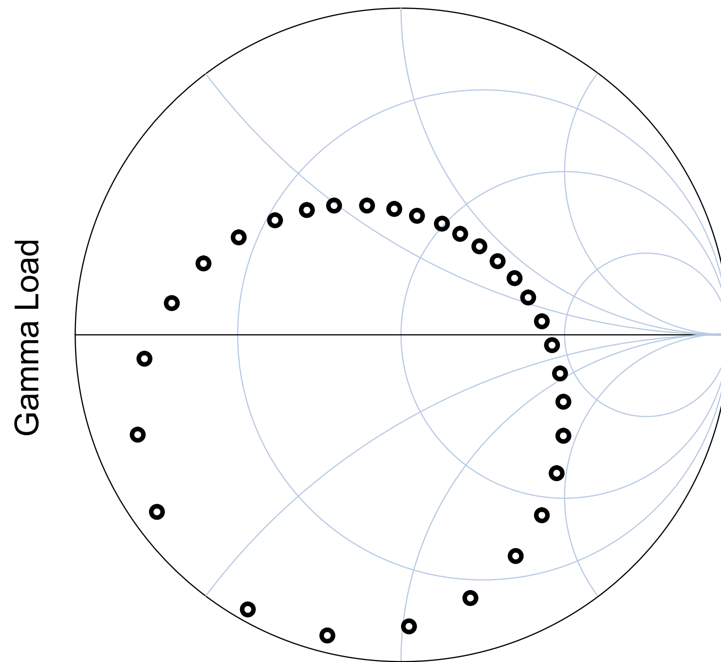

Fig 2.7 Load Impedances corresponding to measurement in Fig. 2.6

The Large Signal Network Analyzer was also largely used for non-linear electron device modeling. First models that have been identified with LSNA measurements were empirical models. In these models a large number of parameters must be identified starting from the knowledge of the physical description of the transistor. An example is provided by the device description proposed by John Wood and David Root and is based on state-space models [15]. These models are black-box time-domain models that are typically used in physics for describing all kinds of nonlinear dynamical processes. David Root was the first one who used a simple version of the more general state-space function model approach for implementing a microwave transistor model based on Large Signal Network Analyzer measurements.

In a state-space function approach, one assumes that the port currents of a device are a general nonlinear function of a limited set of state variables. The state variables are the port voltages, the first- and higher-order derivatives of the port voltages, and the first- and higher-order derivatives of the port currents. By performing an adequate number of LSNA measurements, by processing the gathered data, it can be identified the relevant set of state variables and the functions themselves. One of the main challenges is the experiment design. In order to have a good fit to the state-space functions, it is necessary to have a dense coverage of the state-space over a meaningful range. An original solution to this problem was developed by Schreurs in

[16]. She simultaneously applied excitation tones having different frequencies to the gate and the drain of a microwave transistor. The two-tone experiment allows dense coverage of the gate and drain voltage state-space over a meaningful range. It might be interesting to note that the two-tone technique was actually invented several decades ago by mechanical engineers dealing with the characterization of nonlinear mechanical structures.

References

[1] J. Rodriguez-Tellez, T. Fernandez, A. Mediavilla and A. Tazon, "Characterization of Thermal and Frequency-Dispersion Effects in GaAs MESFET Devices", IEEE Trans. Microwave Theory and Techn., vol. 49, No. 7, pp. 1352 – 1355, Jul. 2001.

[2] A. Parker and J. Scott, "Method to determine correct timing for pulsed I/V measurement of GaAs Fets", Electron. Lett., vol. 31 , No. 19 , pp. 1697 - 1698, Sept. 1995.

[3] J.B. Scott, J.G. Rathmell, A.E. Parker, and M. Sayed, "Pulsed device measurements and applications", IEEE Trans. Microwave Theory and Techn., vol. 44, pp. 2718-2723, Dec. 1996.

[4] W. Ciccognani, F. Giannini, E. Limiti, P.E. Longhi, M.A. Nanni, A. Serino, C. Lanzieri, M. Peroni, P. Romanini, V. Camarchia, M. Pirola, G. Ghione, "GaN Device Technology: Manufacturing, Characterization, Modelling and Verification," in Proc. IEEE 14th Conference on Microwave Techniques, Prague, 2008, pp. 1–6.

[5] J. Michael Golio, "Microwave MESFETs and HEMTs", published by Artech House.

[6] S.H. Wemple et al., "Control of Gate-Drain Avalanche in GaAs MESFET's ", IEEE Trans. Electron Devices, vol. 27 No. 6, pp. 1013 – 1018, June. 1980.

[7]. W. Struble, S.L.G. Chu, M.J. Schindler, Y. Tajima, J. Huang, " Modeling intermodulation distortion in GaAs MESFETs using pulsed I-V characteristics", Proc. GaAs IC Symposium, pp. 179 - 182, Oct. 1991

[8] T. Roh, Y. Kim, Y. Suh, W. Park, B. Kim, "A simple and accurate MESFET channel-current model including bias-dependent dispersion and thermal phenomena", IEEE Trans. Microwave Theory and Techn., vol.45, No. 8, pp. 1252 - 1255, Aug. 1997.

[9] A.E. Parker and D.E. Root, "Pulse measurements quantify dispersion in pHEMT's", Proc. URSI/IEEE Electron. Symp. Sign. Syst., pp. 444-449, Oct. 1998.

[10] A. Santarelli, G. Vannini, F. Filicori, P. Rinaldi, "Backgating model including self-heating for low-frequency dispersive effects in III-V FETs", Electron. Lett. 34 (Oct. 1998), pp. 1974 - 1976.

[11] F. Filicori, G. Vannini, A. Santarelli, A.M. Sanchez, A. Tazon and Y. Newport, "Empirical modeling of low-frequency dispersive effects due to traps and thermal phenomena in III-V FET's", IEEE Trans. Microwave Theory and Techn., vol. 43, pp. 2972-2981, Dec. 1995.

[12] F. Filicori, G. Vannini, A. Mediavilla, A. Tazon , "Modelling of deviations between static and dynamic drain characteristics in GaAs FETs" , in 23rd European Microwave Conference, 1993.

[13] Focus Microwaves Data Manual, Focus Microwaves Inc., Montreal, Canada, 1988.

[14] D. Barataud, F. Blache, A. Mallet, P.P. Bouysse, J.-M. Nébus, J.P. Villotte, J. Obregon, J. Verspecht, and P. Auxemery, “Measurement and control of current/voltage waveforms of microwave transistors using a harmonic load-pull system for the optimum design of high efficiency power amplifiers,” IEEE Trans. Instrum. Meas., vol. 48, pp. 835–842, Aug. 1999.

[15] J. Wood, D.E. Root, and N.B. Tufillaro, “A behavioral modeling approach to nonlinear model-order reduction for RF/microwave ICS and systems,” IEEE Trans. Microwave Theory Tech., vol. 52, pp. 2274–2284, Sep. 2004.

[16] D. Schreurs, S. Vandenberghe, J. Verspecht, B. Nauwelaers, and A. Van de Capelle, “Direct extraction of the nonlinear hemt model from vectorial large-signal measurements,” in Proc. Int. Workshop Advanced Black-Box Techniques Nonlinear Modeling, Belgium, July 1998, pp. 228–233.

CHAPTER III :

A Novel Measurement Technique Oriented to the Characterization of low-Frequency Dispersive Effects

Introduction

In this chapter, an alternative, technology independent large-signal measurement set-up is proposed for the experimental investigation on the low frequency (LF) dispersion of current/voltage (I/V) characteristics in micro- and millimetre-wave electron devices and for their modeling. As previously said, low-frequency dispersion effects are an important issue in characterization and modeling of electron devices. The experimental characterization procedures aimed at the performance evaluation and large-signal (LS) empirical modeling of microwave electron devices should accurately take into account the low-frequency (LF) dispersion of the transistor current/voltage characteristics. These effects, which are directly observable at the electrical terminals in terms of important deviations between the LF dynamic I/V curves and the static ones, are mainly due to self-heating (i.e., power dissipation within the physical structure of the device) and carrier (de-)trapping phenomena, the latter ones related to the presence of spurious energy levels both at the surface interfaces and in the semiconductor deep layers. This issue, sometimes neglected in the past years, has proved as extremely important in the context of empirical nonlinear modeling of electron devices for microwave integrated circuit design. In fact, the accurate description of LF dispersive phenomena strongly enhances the capability of obtaining accurate predictions also at millimetre-wave frequencies.

Many efforts have been made by several research groups to take into account LF dispersion, both in the framework of look-up table- and equivalent circuit-based device models [e.g., 1-4]. Beside dc I/V and bias-varying small-signal parameter measurements, many of these modeling approaches also need pulsed I/V measurements during the identification phase for improved prediction accuracy. Such techniques, besides requiring rather complex, special-purpose measurement setups [5-6], also introduce reliability issues, as discussed in the next Section.

In the proposed measurement system, by means of conventional laboratory components and instrumentation, the device under test (DUT), which can be either a field-effect- or a bipolar-technology transistor, is excited at both input and output ports through LF sinusoidal sources and its operation monitored, in terms of current/voltage instantaneous value evolutions (dynamic I/V loci, in the following), mean values, and power dissipation. The empirical information needed for the characterization of the DUT LF dispersion is collected under reliable operating conditions, by exploiting simple calibration techniques and without exciting the high-frequency nonlinear dynamic effects of the device, which have an important role in the transistor behavior at microwaves, but represent perturbing phenomena when the investigation is focused on LF I/V characteristics.

In this chapter, after discussing the theoretical background of low-frequency dispersion that affects microwave electron devices the proposed measurement technique will be presented describing its hardware and software implementations. Finally different experimental examples are provided, on both field-effect and bipolar transistors, to definitely demonstrate the effectiveness of the proposed electron-device characterization technique.

3.1 Characterization of LF dispersion in microwave devices

The microscopic effects of spurious, trapping energy levels distributed throughout the physical structure of an electron device propagate up to the electrical ports, causing the perturbation of the instantaneous values of the currents, according to the following general description [7]

$$\mathbf{i}(t) = \mathbf{F}_{LF}[\mathbf{v}(t), \mathbf{x}(t), \vartheta(t)] \qquad (3.1)$$

where **v(t)** are the instantaneous voltages applied at the device ports and **x(t)** is a set of state variables, chosen to suitably describe, at the instant ***t***, the overall distribution of carriers within the traps. Owing to the long time constants associated with the (de-)trapping phenomena, the vector of state variables usually presents a slow dynamics with respect to the voltage time-evolutions, which can be properly described by means of transfer functions with frequency-band from dc up to about 100 kHz. The average (channel) junction temperature is also included in Eq. (3.1), in order to account for the thermal state of the (field-effect) bipolar transistor. This temperature, too, is characterized by a slow dynamics with respect to the power dissipated within the device, with time constants approximately of the same order as those considered in the case of trapping phenomena.

Clearly the purely algebraic representation of Eq. (3.1), which is referred to as the LF dynamic I/V characteristics of the electron device, is valid in the presence of operating conditions which only involve moderately low frequency components, i.e., still too low to significantly excite the reactive nonlinear effects typical of microwaves. However, when high-frequency nonlinear operation is considered, as in the case of the circuit applications to which the device is oriented (e.g., microwave power amplifiers, mixers), the currents at the device intrinsic ports can be still described by Eq. (3.1), provided that dynamic terms are introduced in order to take into account the high-frequency nonlinear dynamics of the transistor. LF dynamic I/V models can usually be embedded easily in equivalent circuits or other empirical models suitable for large-signal microwave device description.

From a general standpoint, the modeling of LF dispersive phenomena would involve the investigation of the nonlinear device behavior in the presence of port excitations having a totally general spectral component allocation over the frequency-band [dc – 100 kHz]. However, by considering above cut-off conditions, the vector of state variables can be assumed coincident with its mean value, i.e., $\mathbf{x}(t) \cong \mathbf{X}_0$. In addition, the empirical evidence shows that no significant direct ac-to-dc conversion of voltage harmonics affects the mean values of the state variables, that is, $\mathbf{X}_0 \cong \mathbf{H}(\mathbf{V}_0)$, where $\mathbf{V}_0$ are the mean values of voltages applied at the device ports [1]. Similar considerations lead to the hypothesis $\vartheta(t) \cong \vartheta_0$, i.e., the channel/junction temperature can be considered as a constant quantity during the device microwave operation,

and thus its value expressed in terms of average dissipated power P_0, thermal resistance and case/substrate temperature ϑ_c. Under these assumptions, the dynamic I/V characteristics of Eq. (3.1) can be expressed, above the cut-off of LF dispersion, as

$$\mathbf{i}(t) = \mathbf{F}'_{LF}[\mathbf{v}(t), \mathbf{V}_0, P_0, \vartheta_c] = \mathbf{F}_{DC}[\mathbf{v}(t), \vartheta_c] + \Delta\mathbf{i}[\mathbf{v}(t), \mathbf{V}_0, P_0, \vartheta_c] \quad (3.2)$$

where the dynamic I/V curves are explicitly described in terms of deviations with respect to the static I/V characteristics $\mathbf{F}_{DC}$ (at a given case temperature). It has been largely demonstrated in the literature that the deviation term $\Delta\mathbf{i}$ in (32), which is inherently related to thermal and trapping phenomena, introduces important discrepancies with respect to dc current characteristics. These deviations have to be accurately accounted for in order to identify models that guarantee adequate prediction capability under nonlinear operation [1-7].

3.2 Electron device characterization under nonlinear operation

In order to experimentally characterize the effects of low-frequency dispersion on the electron device characteristics, pulsed current/voltage measurements are often exploited by the microwave community. Starting from a given quiescent point, very short voltage pulses are superimposed to the bias values $\mathbf{V}_0$ in order to dynamically achieve the voltage excitation $\mathbf{V}$; correspondingly, the currents at the device ports are measured, assuming that the long time constants associated with LF dispersion preserve from any change of the state of traps and channel/junction temperature with respect to the corresponding values in the starting quiescent operation. By varying the bias point on a suitable grid, pulsed characterization leads to isothermal and isodynamic I/V curve sets, each one being a reasonable description of the “local” device behavior in the neighbourhood of a particular quiescent condition. It should be noticed that, according to Eq. (3.2), the trapping status corresponding to a particular large signal class of operation can be reproduced in an equivalent pulsed regime by choosing the same quiescent condition $\mathbf{V_0}$. However, the same consideration does not apply for the thermal status. Under narrow pulsed operation, the device thermal status corresponds to the total dissipation of the power supplied by the bias system

in the selected quiescent condition. Instead, under large signal dynamic operation, part of the power supplied by the bias system is actually delivered to the load. Thus, it is evident that the device thermal condition forced under pulsed operation cannot be considered as equivalent to the thermal status of the device under large signal regime. Moreover, the application of voltage pulses also presents some drawbacks. For example, a critical point is related to the extremely wide spread of the pulsed-waveform spectral components. In fact, bias-dependent frequency behavior of DUT input and output impedances, bandwidth limitation of cables, bias networks and other components of the measurement setup, may actually "extend" the actual duration of pulses in such an almost unpredictable way. This leads to critical calibration procedures and possibly sub-optimal choices of the sampling times for current acquisitions [8]. Thus, the achievable measurement accuracy is often rather limited and not always easily evaluated.

On the other hand, as discussed in chapter two, in order to characterize the high-frequency nonlinear electron device behaviour, different measurement systems have been proposed [9-12]. Most of these setups are based on a purely high-frequency sinusoidal excitation superimposed to a particular bias condition, leading to device operation typical of power amplification. However, these approaches are frequency and power limited due to the complexity of the DUT (i.e., at microwave frequency the transistor is a nonlinear dynamic system) and to the significant non ideal behaviour of the microwave setups components. Moreover, their cost dramatically increases moving towards high power and/or frequency operation. A major limitation of these techniques [13] is related to the difficulty in synthesizing the full range of device terminations: especially when on-wafer devices having a large periphery are considered, passive load synthesis technique suffers from the inability to synthesize very low impedances, whereas active load synthesis may become critical from the stability point of view.

Since the operation under sinusoidal excitation is believed to be an important feature, leading to a characterisation more coherent with the final device application,

a large portion of the work done during this thesis was devoted to the development of a low-frequency large-signal sinusoidal excitation setup for the investigation of dispersive phenomena due to charge trapping effects and thermal self-heating which represents an alternative to the approaches based on pulsed excitation [5-6],

involving a rather peculiar operation, by far different from what is observed in power amplifiers or in other typical nonlinear blocks of the RF front-ends. The operating frequency is settled at few megahertz in order to characterize the device behaviour above the upper cut-off frequency ($\mathbf{f_{co}}$) associated with dispersive phenomena (typically some hundreds of kilohertz) but low enough to neglect microwave reactive effects related to the linear extrinsic parasitic network and nonlinear dynamic phenomena [7]. In the selected frequency range the transistor can be considered as a “purely-algebraic” measurand leading to a simplified characterization technique for electron device dispersion.

The measurement set-up described in the following has been adopted for the characterization of the deviations in Eq. (3.2). The evolution of the device instantaneous LS working point on the dynamic I/V characteristics is observed directly in the time-domain, in the presence of independent and fully-controllable LS voltage forcing excitations at the two ports, at frequencies sufficiently low to guarantee easy calibration procedures. Since the values ($\mathbf{V_O}$, $\mathbf{P_O}$) are monitored as well (also the case temperature can be controlled, if needed), the empirical data provided by the proposed set-up are a direct, accurate information on the LF dynamic I/V characteristics (3.2), gathered under reliable operating conditions.

3.3 Low frequency two-source large-signal measurement system

The system proposed here allows to apply low-frequency large-signal sinusoidal excitations at the input and output ports of an electron device. It can be considered as an extension of [14], although capabilities and flexibility are by far extended in this setup. The measurement procedure limitations of the original system, related to the single port excitation and the choice of a resistive loading condition, are here overcame by adopting two sources with active load synthesis capabilities. The implementation of an arbitrary loading condition is essential to quickly characterize the DUT under very different operating conditions. In Fig. 3.1 an intuitive representation of the proposed measurement technique is reported. The two signal sources, having an output impedance of 50 ohm, are able to directly control the amplitudes of the incident signals, both at the input and output device ports ($\mathbf{A_I}$, $\mathbf{A_O}$),

and their relative phase ($\Delta\varphi$). The device under test responds to these stimuli with the reflected waves ($\mathbf{B_I}$, $\mathbf{B_O}$). By acquiring incident and reflect waveforms it is possible to reconstruct voltages and currents at the device ports by equation (3.3) and (3.4):

$$V_{I\backslash O} = A_{I\backslash O} + B_{I\backslash O} \qquad (3.3)$$

$$I_{I\backslash O} = \frac{\left(A_{I\backslash O} - B_{I\backslash O}\right)}{50\,\Omega} \qquad (3.4)$$

where 50 ohm represents the system characteristic impedance. It is evident that by controlling the generator stimuli it is possible to directly synthesize very different device operations. As a consequence, a complete characterization of the device is obtainable with this instrumentation, by involving any operation of interest and by measuring dynamic I/V loci at the device ports.

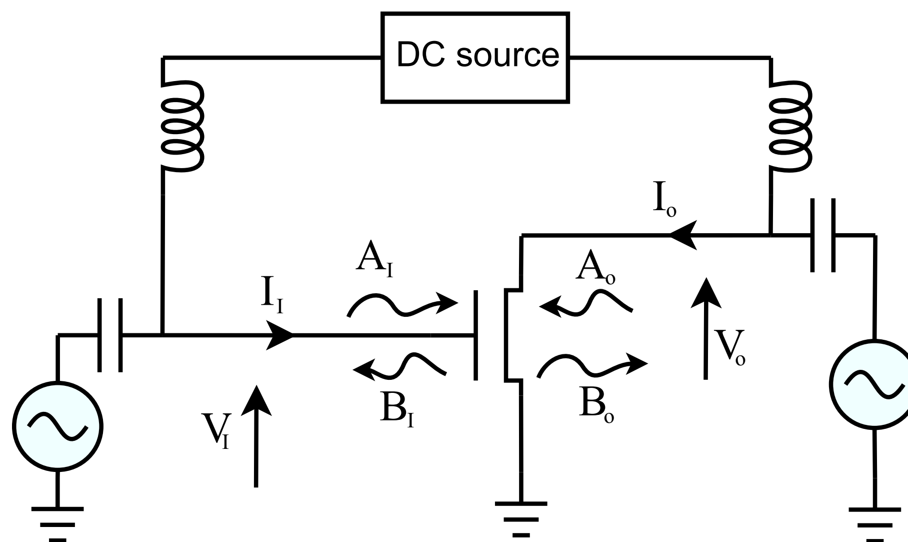

Fig. 3.1. Schematic representation of the proposed characterization technique

3.3.1 The setup architecture

The measurement system proposed is shown in Fig. 3.2. A two-channel arbitrary function generator (Tektronix AFG320) with 50 ohm output impedance is used to excite the DUT ports with low-frequency (e.g., a few megahertz) sinusoidal voltage waveforms. The operating frequency is chosen in order to characterize the device behavior above the upper cut-off frequency (f_{co}) associated with dispersive

phenomena (typically some hundreds of kilohertz). The 25-watt power amplifier (PA), cascaded with channel-2 of the function generator, allows to obtain significant load-pulling capability when high-power devices are characterized.

A four-channel sampling oscilloscope (Agilent 54835A, 2 GSa/s) provides acquisition of the DUT incident and reflected waves; an impedance of 50 ohm is selected at each input channel. Monitoring of incident and reflected waves at the DUT input and output ports is obtained by means of two wide-bandwidth (10 kHz – 1 GHz) dual directional couplers, while two 100 kHz–400 MHz bandwidth bias-tees with low-insertion loss (0.15 dB) provide both DC and RF path isolation and device stability. The DC source (HP 4155B) provides the bias and measures the average values of the electrical variables at the device ports. A microwave probe station is needed for on-wafer measurements.

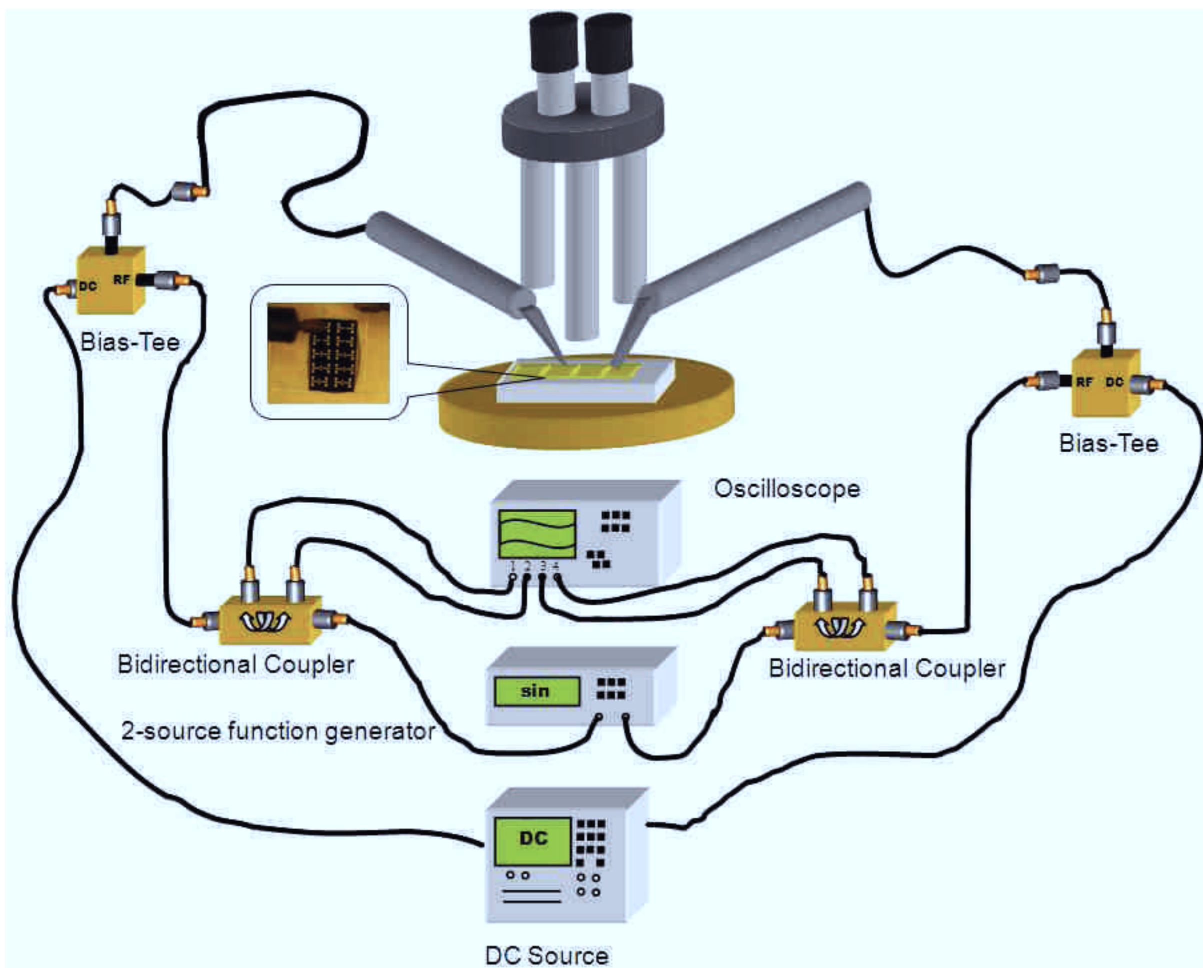

Fig. 3.2. The proposed large-signal measurement setup.

At the frequency of a few megahertz all the measurement system components well satisfy linear non-distortion conditions, greatly simplifying the calibration procedure required for the reconstruction of the dynamic I/V loci at the device ports. To this aim, the setup can be divided into six signal paths to be characterized in terms of attenuation and delay in the operating frequency range (i.e., [2 MHz – 16 MHz]): a) from channel 1 of signal generator section to DUT input port; b) from channel 1 of signal generator section to oscilloscope section (input-port incident-wave acquisition section); c) from DUT input-port section to oscilloscope section (input-port reflected-wave acquisition section); d) from channel 2 of signal generator section to DUT output-port; e) from channel 2 of signal generator section to oscilloscope section (output-port incident-wave acquisition section); f) from DUT output-port section to oscilloscope section (output-port reflected wave acquisition section). Table 3.1 shows the characterization data for each path, i.e. the average values of the attenuation and delay of each signal path over the operating frequency range. In particular, each value in Table I has been obtained by adopting the following procedure:

i. for each frequency considered in the operating range (in the present case 2 MHz ≤ frequency ≤ 16 MHz with step 2 MHz) and for each path, the quantities of interest are acquired by the oscilloscope setting the number of averages to 1024;
ii. the average values are obtained by averaging the quantities measured at the different frequencies.

Path	a	b	c	d	e	f
Delay [ns]	**11.0 (0.1)**	**8.4 (0.3)**	**10.8 (0.1)**	**10.5 (0.1)**	**8.2 (0.3)**	**10.8 (0.1)**
Attenuation [dB]	**0.43 (0.01)**	**39.98 (0.03)**	**40.31 (0.04)**	**0.53 (0.03)**	**40.16 (0.02)**	**40.28 (0.05)**

Tab. 3.1 .Characterization of elementary signal-paths of the measurement setup averaged over the operating frequency range.

The standard deviations are also reported in Table 3.1 (in brackets), in order to quantify the dispersion around the mean value deriving from the two-steps averaging process.
Once the characterization procedure has been carried out, a linear model of the measurement system can be easily implemented into a commercial CAD environment oriented to microwave circuit design (e.g., Agilent Advanced Design System), as shown in Fig. 3.3.

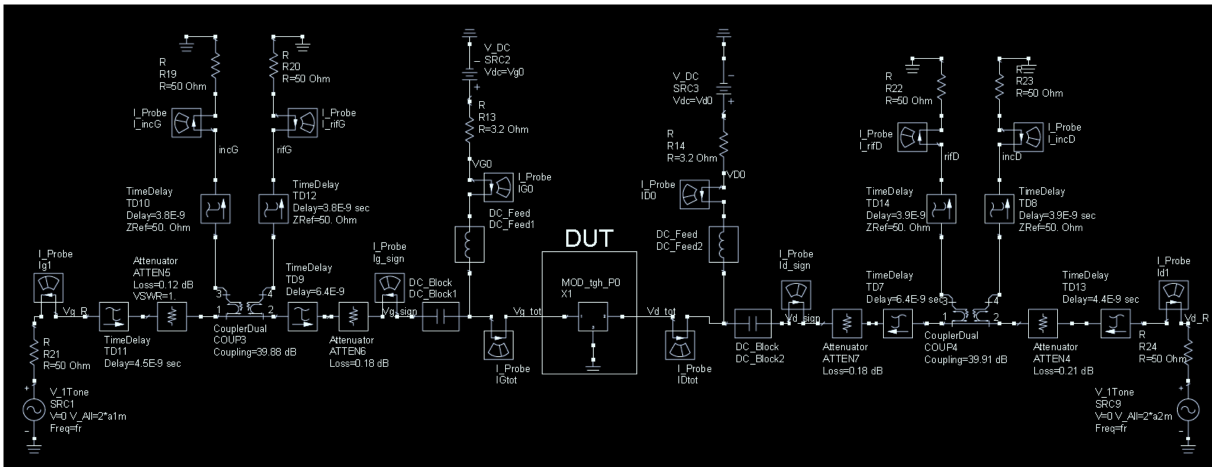

Fig 3.3. Model of the proposed measurement system implemented into a commercial CAD tool.

The validity of the calibration procedure has been tested by replacing the DUT with two isolated 12.5 Ω resistances connected at the input and the output ports. The selected resistances make part of an alumina calibration substrate and are designed to properly work up to 110 GHz. These two terminations are therefore purely resistive at few megahertz. The incident and reflected waveforms were measured under sinusoidal excitation at different frequencies and the reconstructed I/V loci were compared with the corresponding simulated results. Output current loci at selected frequencies within the operating range are shown in Fig. 3.4. Measurements and simulations are here compared both at the oscilloscope section and at the device port.

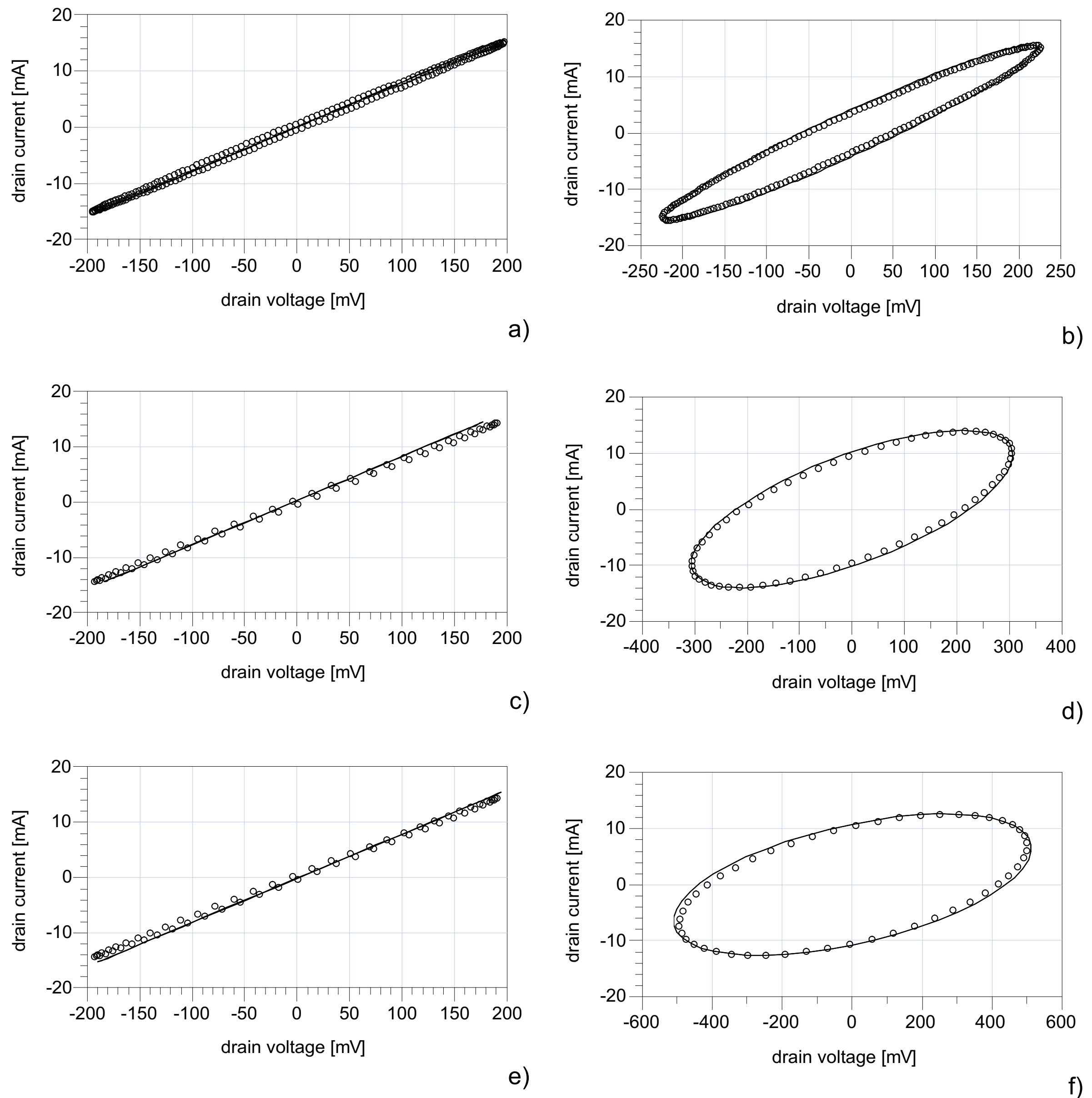

Fig. 3.4. I/V loci at the device (a-c-e) and oscilloscope (b-d-f) sections. Comparison between measures (circles) and simulations (continuous lines). Frequency of excitations: 2 MHz (a-b), 8 MHz (c-d) and 6 MHz (e-f).

The impedances measured at the device section are reported in Table 3.2. Perfect instrument calibration is achieved. Identical results were obtained at the input port.

	2 MHz	8 MHz	16 MHz
Measured impedance	$13\angle 2°$	$13.4\angle 2°$	$13.6\angle 3°$

Tab. 3.2. Impedances at the device section corresponding to the loci shown in Fig. 3.4

An alternative characterization procedure can be carried out by Low Frequency S-parameters measurements of the input and output paths. In this case the entire

measurement system can be divided in two four-port networks (for input and output system paths, respectively) as shown in Fig. 3.5.

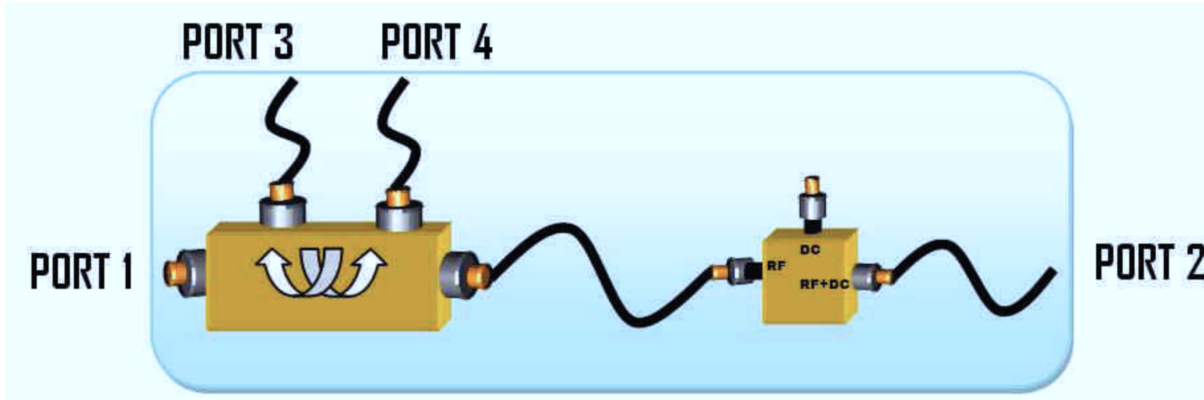

Fig 3.5 Four port representation of input (or output) path.

The port 1 corresponds to the reference plane of the sinusoidal signal source, port 2 is the DUT reference plane and ports 3 - 4 represent the oscilloscope reference planes for the incident and reflected waveforms, respectively.

In this representation gate and drain paths can be described by means of a 4x4 S-parameters matrix:

$$S_{gate/drain} = \begin{pmatrix} S_{11} & S_{12} & S_{13} & 0 \\ S_{21} & S_{22} & 0 & S_{24} \\ S_{31} & 0 & S_{33} & 0 \\ 0 & S_{42} & 0 & S_{44} \end{pmatrix}$$

where zero denotes that the corresponding ports are not coupled. All parameters were measured by means of a HP 4195A Network Analyzer in the range of frequencies from 300 kHz to 140 MHz . In Fig 3.6 are shown some of the S-parameters measured for the gate path:

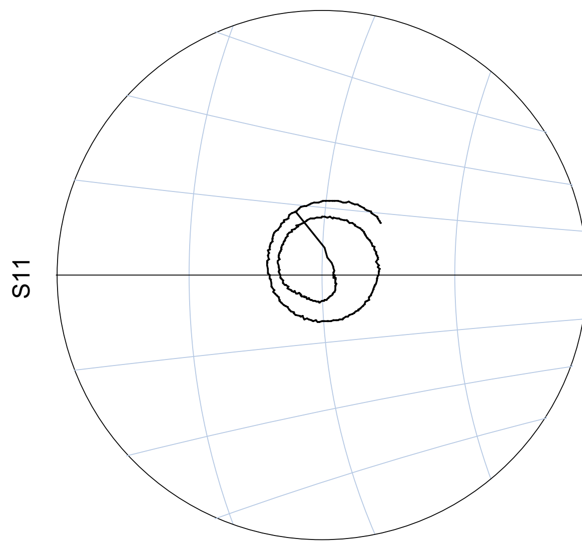

a)

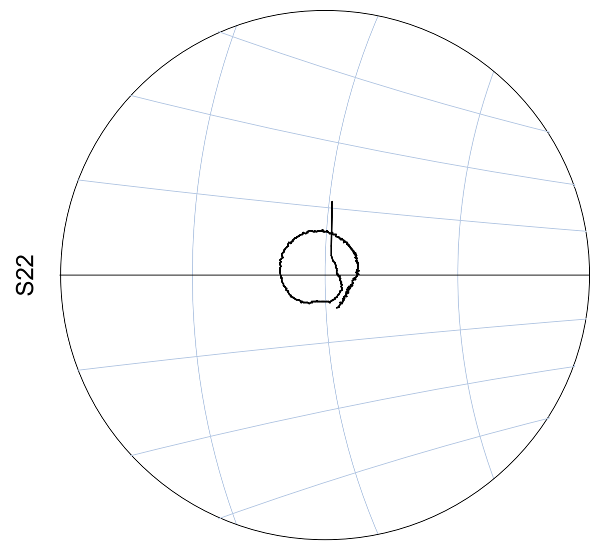

b)

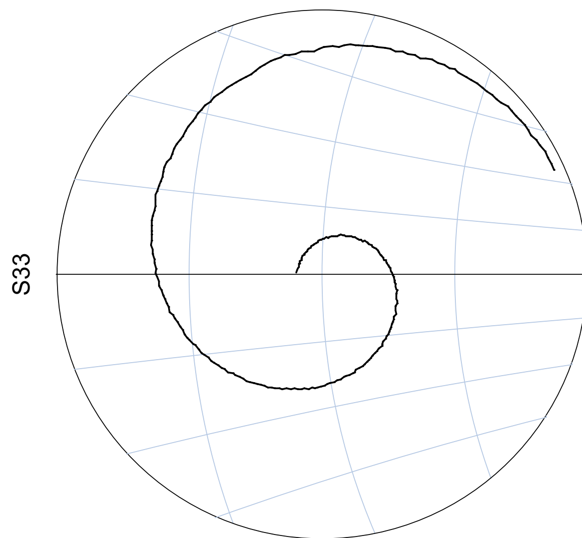

c)

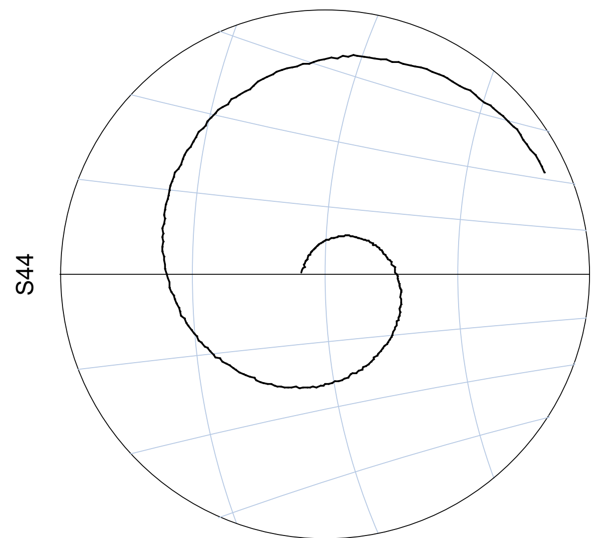

d)

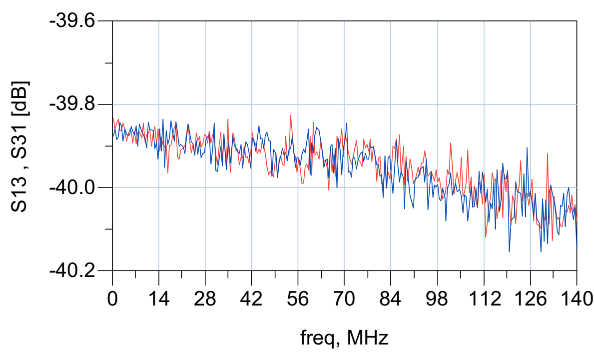

e)

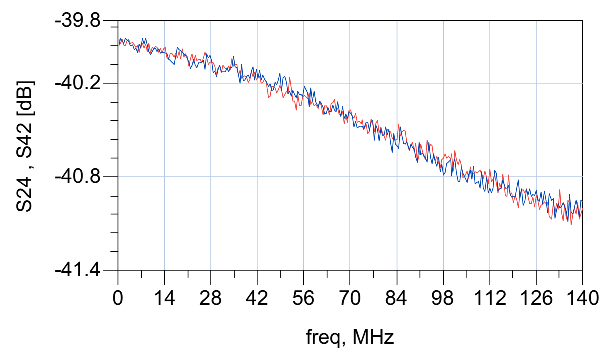

f)

Fig 3.6. Measured S-parameters of input path over 300 kHZ – 140 MHz.

After measuring S-parameters the calibrated quantities at the device ports can be easily calculated by means of equations (3.5), (3.6) and (3.7), considering that b_3 and b_4 are known terms because are the incident and reflected waves acquired at the oscilloscope reference planes:

$$a_1 = \frac{b_3}{S_{31}} \quad , \quad a_2 = \frac{b_{34}}{S_{42}} \tag{3.5}$$

$$b_1 = S_{11} \times a_1 + S_{21} \times a_2 \tag{3.6}$$

$$b_2 = S_{21} \times a_1 + S_{22} \times a_2 \tag{3.7}$$

Currents and voltages at the input and output DUT reference planes can be calculated by applying Eq. (3.3) and (3.4).
Such a characterization technique reaches the same accuracy level compared to the one previously discussed, even though the characterization procedure is greatly simplified.

3.3.2 The Control Software

The measurement setup is fully controlled via an IEEE488 standard interface by means of a commercial instrument automation software running on a PC (e.g., NI LabVIEW). The developed control-software allows the user to make data acquisitions under nonlinear dynamic regime by automatic controlling all the instruments in the system. The developed Graphical User Interface (GUI) is shown in Fig. 3.7: both dc parameters, such as bias values and corresponding compliances, and ac parameters, such as amplitudes and relative phase of the generated signals, are easily defined by means of the GUI. The controlling program enables acquisitions in two measurement-modes, which will be referred to in the following as “list-mode” and “sweep-mode”.

In the list-mode, the user manually defines the desired sequences of DC and AC parameters to be used for bias and signal generation. This is very useful when just a few measurements are needed, as when a preliminary device performance evaluation has to be carried out. Alternatively, in the sweep-mode, the program asks the user for grids of: DC bias points, signal amplitudes and relative phases (both for

list- and sweep-mode, DC and AC sections are labeled as “A” and “B”, respectively, in Fig. 3.7). This operation mode is essential for an extensive characterization of device dispersive phenomena, since it allows to carry out measurements in a systematic way, by sequentially adopting bias points on a selected grid and by sweeping amplitudes and phases of input and output signals according to arbitrarily complex schemes.

Fig. 3.7. Main input panel of the control-software Graphical User Interface.

An example of the capability of the measurement setup is shown in Fig. 3.8. Experimental data at the DUT ports are for a 0.25-μm GaAs PHEMT. The advantages of the sweep-mode are here clearly put in evidence. For example, measurements shown in Fig. 3.8 a) were carried out by applying the same bias condition (class-A device operation: V_{g0} = -0.6 V, V_{d0} = 5 V) and the same amplitudes of the input and output incident-signals (A_I = 0.05 V, A_O = 1 V), while sweeping their relative phase over the range 0° ≤ $\Delta\varphi$ ≤ 300° (step 60°). Another example is shown in Fig. 3.8 b). In this case, measurements were carried out by maintaining constant bias conditions (the same class-A operation), constant relative phase of the incident signals ($\Delta\varphi$ = 180°), constant amplitude of the drain incident signal (A_O = 1 V), while the amplitude of the gate incident signal was swept over the range 0.05 V ≤ A_I ≤ 0.25 V (step 0.05 V).

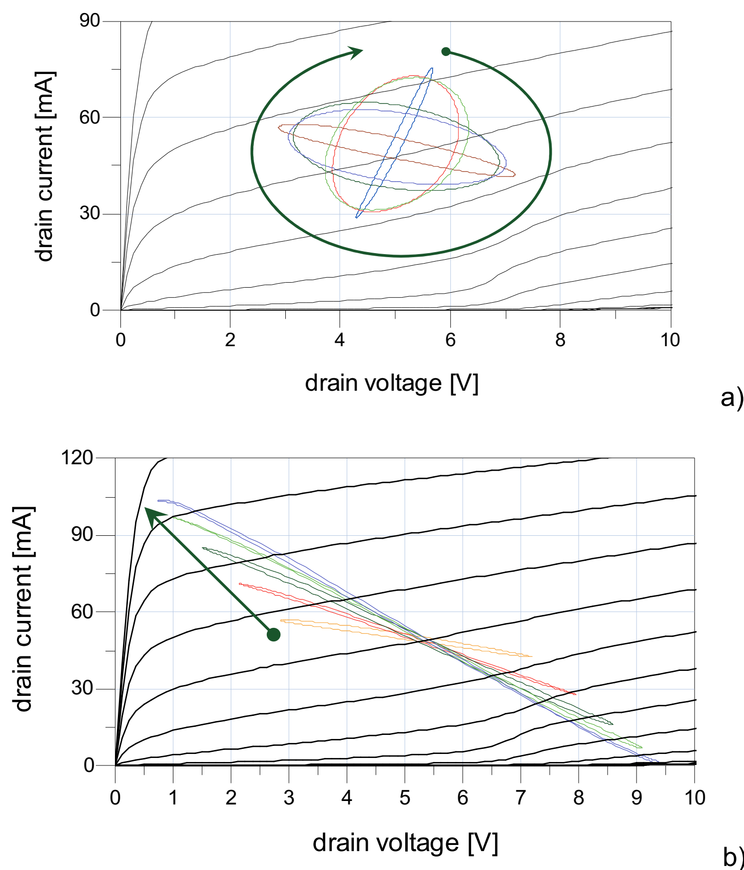

Fig. 3.8. I/V loci at the DUT sections obtained through the measurement setup operated in the sweep-mode (see text). Example a): bias conditions and amplitudes of the incident signals kept constant, relative phase swept. Example b): bias conditions, relative phase of the incident signals and amplitude of the drain incident signal kept constant, amplitude of the gate incident signal swept.

3.4 Experimental Results

As a practical application example of the proposed measurement setup, the dispersion effects associated with two different technological processes are compared. To this aim, different I/V loci are presented in Fig. 3.9 and 3.10 in the cases of two devices, a GaAs-based PHEMT (total periphery: 600 μm) and a GaN-based HEMT (total periphery: 800 μm), respectively. The presented loci (four for each device), correspond to very different operating conditions, i.e. to different bias and/or signals applied at the device ports.

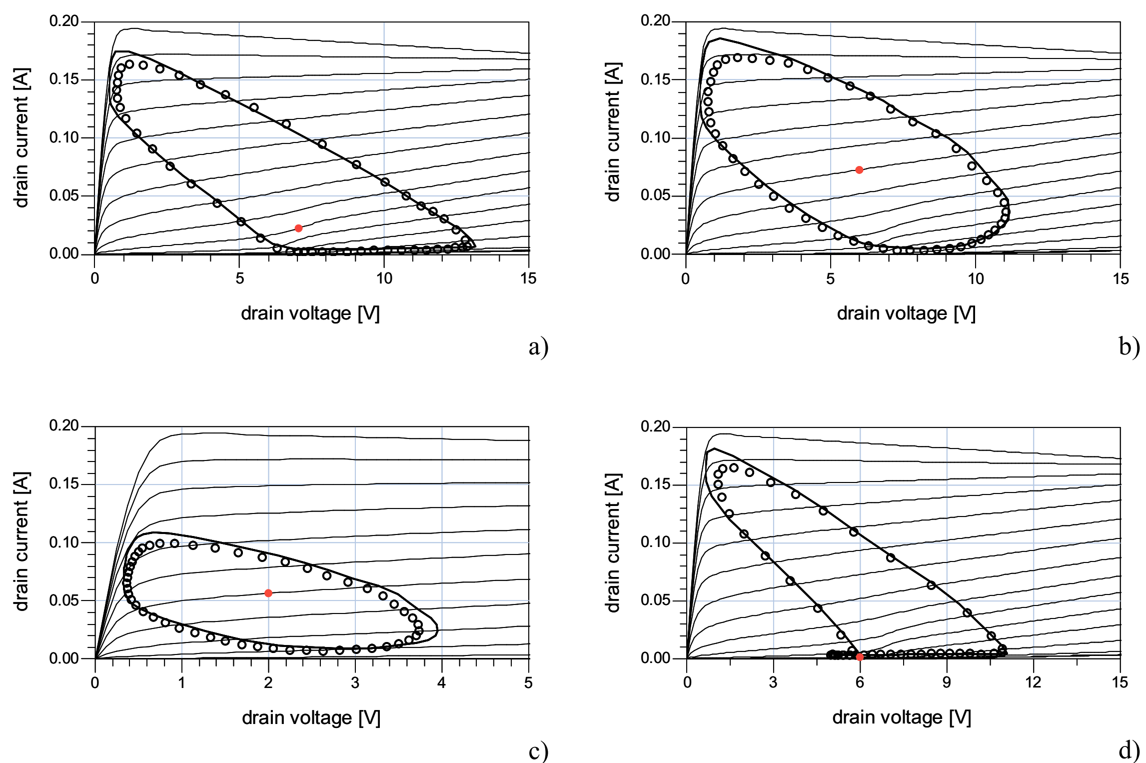

Fig. 3.9. Dynamic I/V loci of a GaAs PHEMT. Measurements (circles) vs. model predictions based on purely-static I/V characteristics (continuous lines). Dc characteristics plotted in the background. a) - (V_{g0} = -0.9 V, V_{d0} = 7 V, A_I = 0.45 V, A_O = 2 V, $\Delta\varphi$ = 110°), b) - (V_{g0} = -0.6 V, V_{d0} = 6 V, A_I = 0.3 V, A_O = 2 V, $\Delta\varphi$ = 270°), c) - (V_{g0} = -0.6 V, V_{d0} = 2 V, A_I = 0.15 V, A_O = 1 V, $\Delta\varphi$ = 300°), and d) - (V_{g0} = -1.5 V, V_{d0} = 6 V, A_I = 0.75 V, A_O = 2 V, $\Delta\varphi$ = 300°).

The measured I/V loci are compared in Fig. 3.9 and 3.10 to theoretical simulation results obtained by describing the low-frequency behavior of each device through the purely static I/V characteristics (plotted as background in each figure).

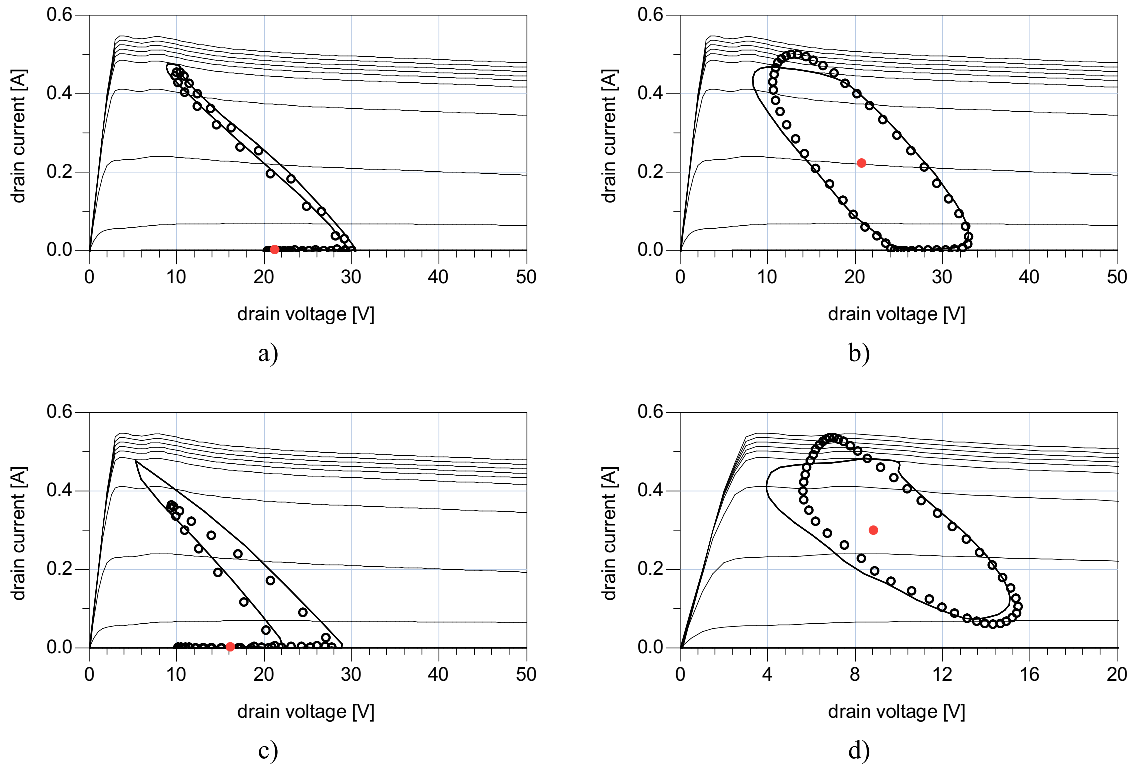

Fig. 3.10. Dynamic I/V loci of a GaN HEMT. Measurements (circles) vs. model predictions based on purely-static I/V characteristics (continuous lines). Dc characteristics plotted in the background. a) - (V_{g0} = -5 V, V_{d0} = 21 V, A_I = 2.5 V, A_O = 3.5 V, $\Delta\varphi$ = 30°), b) - (V_{g0} = -2 V, V_{d0} = 21 V, A_I = 1 V, A_O = 4.5 V, $\Delta\varphi$ = 60°), c) - (V_{g0} = -7 V, V_{d0} = 16 V, A_I = 3.5 V, A_O = 5 V, $\Delta\varphi$ = 30°), and d) - (V_{g0} = -1.5 V, V_{d0} = 10 V, A_I = 0.75 V, A_O = 4.5 V, $\Delta\varphi$ = 30°).

As it can be noted, deviations between dynamically-measured and statically-simulated current loci are minor in the case of the GaAs-based device than in the other case. Since these deviations may be somehow correlated to the settlement of the corresponding technological processes (minor deviations observed, the more settled the process), figures 3.9 and 3.10 give clear indications about the relatively young GaN-based technology. In order to quantify the influence of low-frequency dispersion, the differences between the synthesized impedance values measured and simulated (on the basis of a static I/V model) at the fundamental frequency at the device output port are reported in Table 3.3 and 3.4.

Load impedance	**a**	**b**	**c**	**d**
Measured	$70.5\angle 38°$	$61.2\angle 51°$	$37.5\angle 60°$	$45.5\angle 55°$
Simulated	$72.3\angle 36°$	$62.3\angle 48°$	$38.8\angle 56°$	$44.8\angle 51°$

Tab. 3.3 Comparisons between synthesized impedance values measured and simulated (on the basis of a static I/V model) at the fundamental frequency at the device output port for the different loci shown in Fig. 3.9

Load impedance	a	b	c	d
Measured	$20.2\angle 14°$	$38.6\angle 37°$	$33.5\angle 109°$	$20.1\angle 35°$
Simulated	$22.6\angle 12°$	$42.6\angle 39°$	$23.3\angle 74°$	$21.6\angle 50°$

Tab. 3.4 Comparisons between synthesized impedance values measured and simulated (on the basis of a static I/V model) at the fundamental frequency at the device output port for the different loci shown in Fig. 3.10.

Low-frequency dispersive phenomena on GaN devices was investigated more detail in this work. As previously explained the *resistive core* (ref Figure 1.10 in chapter one) represents the “portion” of the electron device accounting for the DC and LF I / V device characteristics. In order to directly characterize the device “*resistive core*” it is convenient to operate at frequencies where the dynamic effects associated to charge storage variations and/or finite transit times can be neglected. Moreover, it is of primary interest to characterize the device response above the cut-off of low-frequency dispersion (for such a reason pulsed setups exploit very short pulse duration). In order to meet these requirements, the choice of 2 MHz fundamental frequency has been verified, for the electron devices considered in this work, on the basis of S-parameter measurements carried out by exploiting a low-frequency VNA (HP4195A). More precisely, Fig. 3.11 shows the measured output conductance, for a 0.25-μm GaN HEMT device having a periphery of 400 μm, under two different bias conditions corresponding respectively to class-A and AB operation. In the same figure also the output conductance static values are reported to put in evidence the negligibility of frequency variations observable in the range of 2 MHz – 100 MHz. This confirms that a 2 MHz frequency is sufficient to operate above the cut-off of low-frequency dispersion coherently with the large number of papers (e.g., [15]) devoted to microwave device characterization where pulsed measurements with pulse width of 500 ns or more have been adopted.

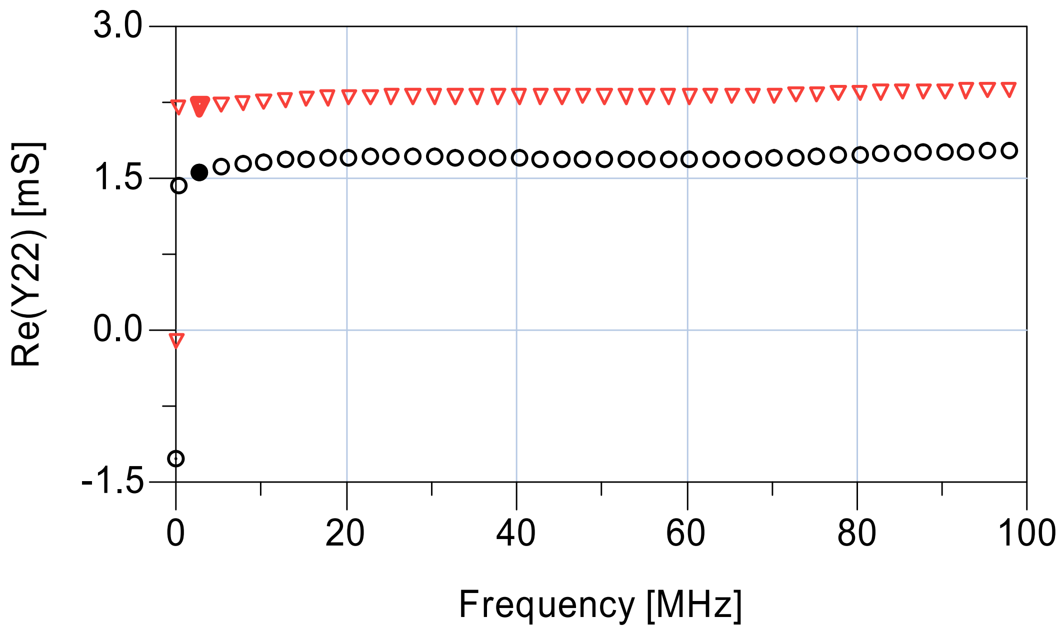

Fig. 3.11 Real part of the Y22 parameter versus frequency for two different bias conditions: Vg0 = -3 V, Vd0 = 20 V (triangles), and Vg0 = -2 V, Vd0 = 25 V (circles). The filled symbols represent the output conductance value at 2 MHz.

Low-frequency measurements carried out by exploiting the low frequency setup are shown in Figs. 3.12 and 3.13. In particular, Fig. 3.12 puts in evidence the current collapse dependence on the average value of the gate voltage V_{g0}. The crosses in the enlarged view within the inset correspond to the same values of the instantaneous voltages (v_g = 0 V, v_d = 5.4 V); if dispersion were not present the same instantaneous current value (corresponding to the DC one) should be measured. Instead, it is well evident that as the quiescent gate voltage V_{g0} moves into the off state region the instantaneous drain current goes down.

Another important dispersive effect is the “knee walkout” [16]. In Fig. 3.13 different measurement sets are reported to characterize such a phenomenon. In particular, measurements were carried out with different drain voltage quiescent conditions and setting the amplitude of the input incident signals in order to dynamically reach the value v_g = 0 V. It is well evident that the knee region is subject to a shift as the average value of the drain voltage increases.

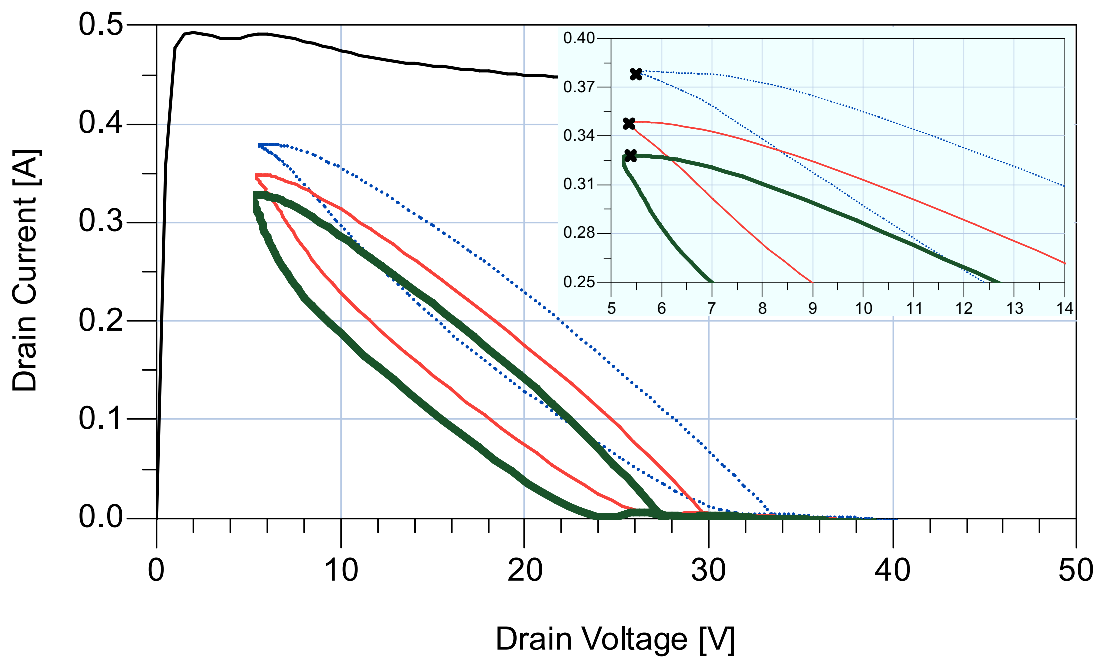

Fig. 3.12. Measurements performed by exploiting the adopted large-signal measurement system on a 800-µm GaN HEMT device, quiescent condition V_{d0} = 25 V and V_{g0} = -3 V (dotted line), V_{g0} = -4 V (continuous thin line), V_{g0} = -5 V (continuous thick line). The measured load lines are superimposed to dc characteristics at V_{g0} = 0 V. The crosses in the enlarged view within the inset correspond to the same instantaneous voltage pair (v_g = 0 V, v_d = 5.4 V).

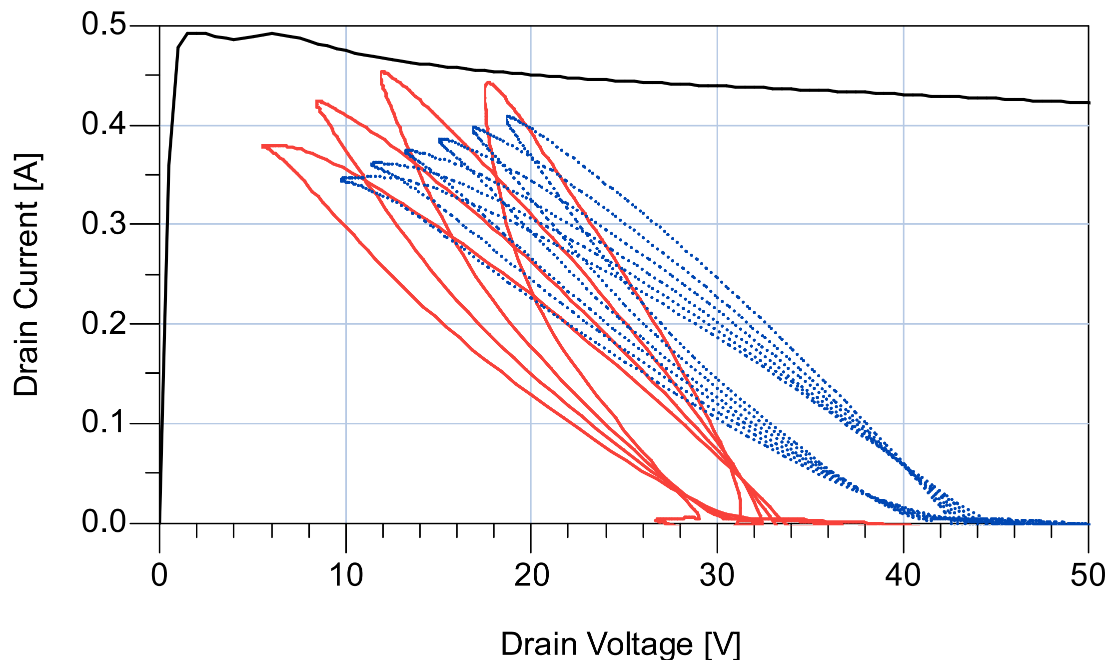

Fig. 3.13. Measurements performed by exploiting the adopted large-signal measurement system on a 800-µm GaN HEMT device, quiescent condition V_{g0} = -3 V and V_{d0} = 25 V (continuous lines), V_{d0} = 35 V (dotted lines). Amplitude of the gate incident signal phasor A_g = 1.5 V. Relative phase between gate and drain incident signal phasors $\Delta\varphi$ = 180 °. Different load lines are obtained by varying the amplitude of the output incident signal phasor. Measurements are superimposed to dc characteristics at V_{g0} = 0 V

In Fig. 3.14 the I/V dynamic loci measured at the input port of a GaAs pHEMT (total periphery: 300 μm) under two different operating conditions are shown. It is well evident the voltage shift between the curves, which is essentially related to the different device thermal state [17-18]. Such a voltage shift is not described (see figure) when using a static I/V model: in this case the two simulated curves practically coincide, since the thermal dependence of the gate current is not taken into account.

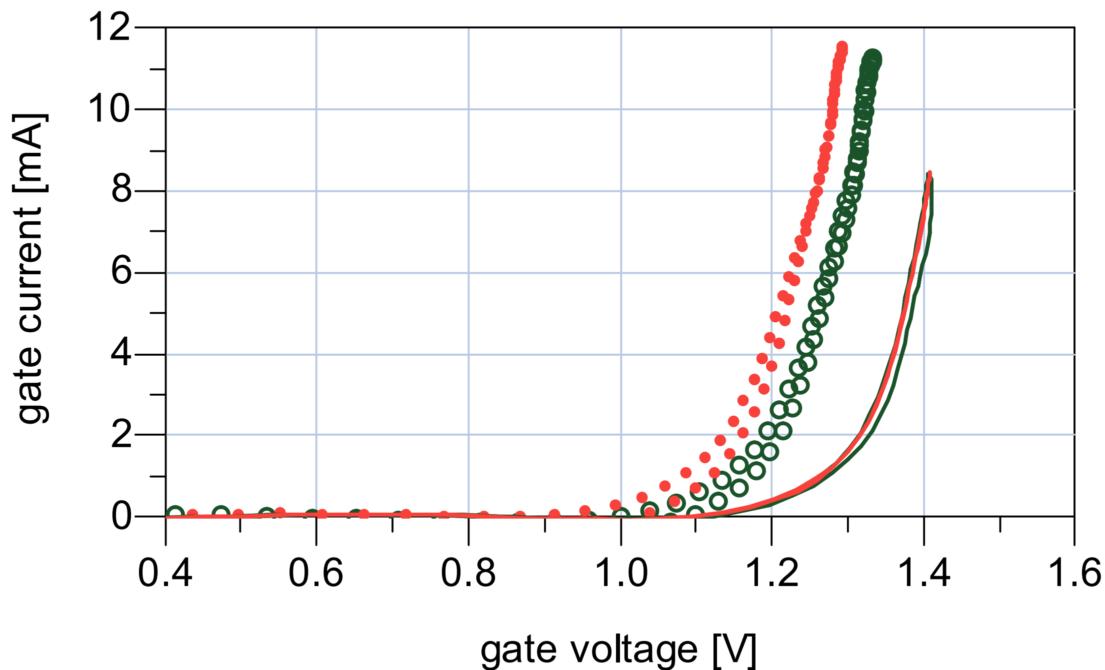

Fig. 3.14. I/V dynamic (symbols) loci measured at the input port of a GaAs pHEMT. Dots - (V_{g0} = -0.4 V, V_{d0} = 8 V, A_I = 1.15 V, A_O = 0 V). Circles - (V_{g0} = -0.4 V, V_{d0} = 12 V, A_I = 1.15 V, A_O = 0 V). Continuous lines – model predictions based on purely-static I/V characteristics.

The proposed measurement setup has the important feature of being technology-independent, that means it can be exploited for the nonlinear dynamic characterization of both field-effect and bipolar transistors. Indeed, large-signal measurements were also carried out on a 2-μm HBT (total emitter periphery: 160 μm). In particular, in Fig. 3.15 the I/V loci associated to four different operations are presented.

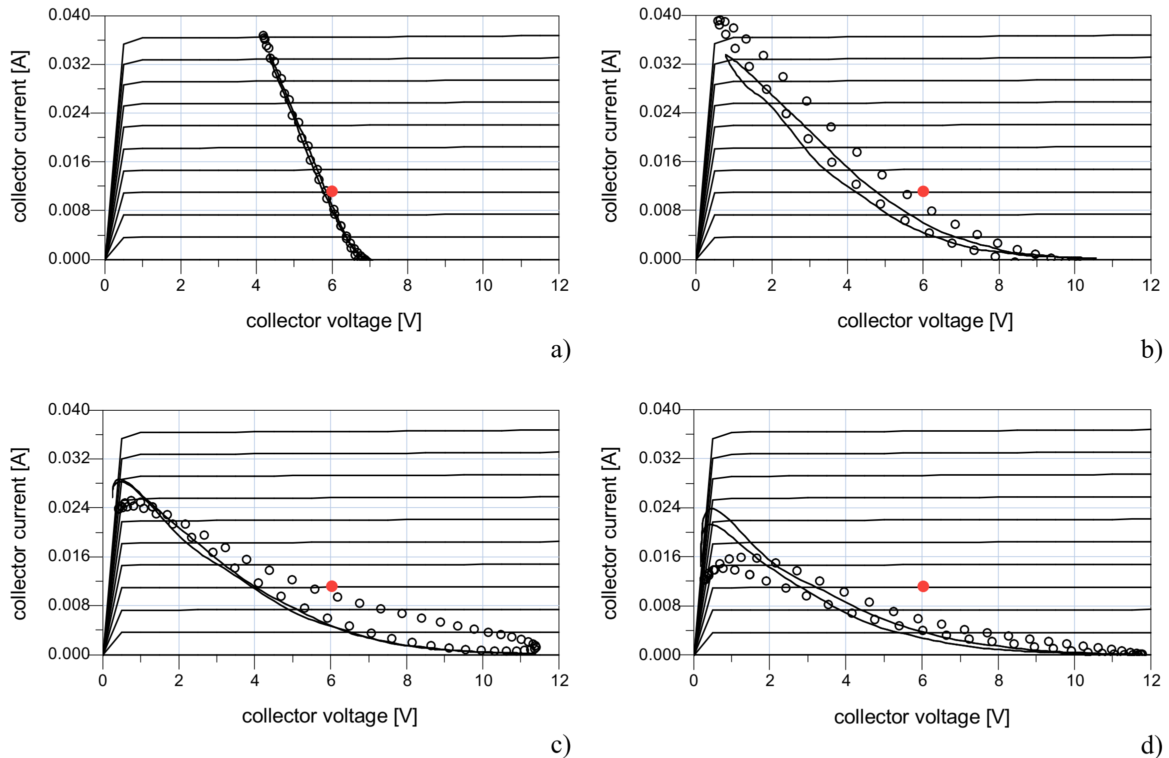

Fig. 3.15. Dynamic I/V loci of a GaAs HBT. Measurements (circles) vs. model predictions based on purely-static I/V characteristics (continuous lines). Dc characteristics plotted in the background. a) (I_{b0} = 0.15 mA, V_{c0} = 6 V, A_I = 0.05 V, A_O = 0 V), b) (I_{b0} = 0.15 mA, V_{c0} = 6 V, A_I = 0.05 V, A_O = 1.25 V, $\Delta\varphi$ = 180°), c) (I_{b0} = 0.15 mA, V_{c0} = 6 V, A_I = 0.05 V, A_O = 2.75 V, $\Delta\varphi$ = 180°), d) (I_{b0} = 0.15 mA, V_{c0} = 6 V, A_I = 0.05 V, A_O = 3 V, $\Delta\varphi$ = 180°)

In this experimental example it is well evident that very different conditions can be synthesized by simply sweeping the amplitude of the output incident-signal: starting from the 50-Ω loading condition (A_O =0 V), the curve-slope can be gradually reduced by increasing the power injected at the device output-port. The measured loci are compared in the figure to model predictions and simulation results based on purely static I/V characteristics. Table 3.5 shows also in this case the comparison between the synthesized impedance values measured and simulated (on the basis of a static I/V model) at the fundamental frequency at the device output port.

Load impedance	a	b	c	d
Measured	76.3∠0°	235.0∠37°	428.9∠10°	776.4∠15°
Simulated	78.8∠0.6°	276.2∠1°	397.8∠5°	585.9∠35°

Table 3.5 Comparisons between synthesized impedance values measured and simulated (on the basis of a static I/V model) at the fundamental frequency at the device output port for the different loci shown in Fig. 3.15

According to the highlighted features, acquisitions of dynamic I/V loci through the proposed instrumentation are believed to be potentially helpful in the development of accurate nonlinear models describing the complex low-frequency dynamics of III-V-based transistors.

Conclusions

An original measurement system that allows to fully characterize LF dispersive effects which strongly affect the nonlinear dynamic behavior of microwave semiconductor device has been proposed. The setup is particularly useful to investigate new device technologies.

In the chapter, the hardware and software system implementations have been widely described, by giving emphasis to the fundamental characteristics of the proposed setup of being accurate and inexpensive. Finally, different experimental examples have been carried out, on both field-effect and bipolar transistors, to definitely confirm the effectiveness of the proposed setup for the development of accurate nonlinear device models

References

[1] A. Raffo, A. Santarelli, P.A. Traverso, M. Pagani, F. Palomba, F. Scappaviva, G. Vannini, F. Filicori, “Accurate PHEMT Nonlinear Modeling in the Presence of Low-Frequency Dispersive Effects,” *IEEE Trans. Microw. Theory and Tech.*, vol. 53, no. 11, pp. 3449-3459, Nov. 2005.

[2] W. Struble, S.L.G. Chu, M.J. Schindler, Y. Tajima, J. Huang, ”Modeling intermodulation distortion in GaAs MESFETs using pulsed I-V characteristics”, in *Proc. GaAs IC Symposium*, pp. 179 - 182, Oct. 1991.

[3] J.-W. Lee and K.J. Webb, “A Temperature-Dependent Nonlinear Analytic Model for AlGaN–GaN HEMTs on SiC”, *IEEE Trans. Microw. Theory and Tech.*, vol. 52 , No. 1, pp. 2–9, Jan. 2004.

[4] K. Jeon, Y. Kwon, and S. Hong, “A frequency dispersion model of GaAs MESFET for large-signal applications,” *IEEE Microw. Guided Wave Lett.*, vol. 7, no. 3, pp. 78–80, Mar. 1997.

[5] A.E. Parker and D.E.Root, Pulse measurements quantify dispersion in pHEMT's, in *Proc. URSI/IEEE Electron Symp Sign Syst*, 444-449, Oct. 1998.

[6] J.B. Scott, J.G. Rathmell, A.E. Parker, and M. Sayed, Pulsed device measurements and applications, *IEEE Trans Microwave Theory and Techn*, vol. 44, pp. 2718-2723, Dec. 1996.

[7] F. Filicori, A. Santarelli, P. A. Traverso, A. Raffo, G. Vannini, and M. Pagani, “Non-linear RF device modelling in the presence of low frequency dispersive phenomena,” *Int. J. RF Microw. Comput.-Aided Eng., vol. 16, no. 1, pp. 81–94, Jan. 2006*.

[8] V. Camarchia, et al., “Fabrication and nonlinear characterization of GaN HEMTs on SiC and sapphire for high-power applications”, *Int. Journal of RF and Microwave CAE*, Vol. 16, pp. 70 – 80, 2006.

[9] Jan Verspecht, “Large-signal network analysis” *IEEE Microwave Magazine*, vol.6, pp 82 – 92, 2005.

[10] D. Schreurs, K. Van der Zanden, J. Verspecht, W. De Raedt, and B. Nauwelaers, “Real-time measurement of InP HEMTs during large-signal RF overdrive stress,” in *Proc. European Gallium Arsenide and related III-V compounds Application Symposium*, Amsterdam, 1998, pp. 545-550.

[11] V. Teppati, A. Ferrero, D. Parena, U. Pisani, “Accuracy Improvement of Real-Time Load-Pull Measurements”, *IEEE Transactions on Microwave Theory and Techniques,* vol. 56, pp. 610 – 613, 2007.

[12] F. De Groote, J.-P. Teyssier, O. Jardel, T. Gasseling, J. Verspecht, “Introduction to measurements for power transistor characterization,” *IEEE Microwave Mag.*, vol. 9, no. 3, pp. 70–85, Jun. 2008.

[13] F. Giannini, G. Leuzzi, Nonlinear Microwave Circuit Design. Chichester, England: Wiley, 2004.

[14] A. Raffo, A. Santarelli, P. A. Traverso, M. Pagani, G. Vannini, F. Filicori, "Accurate Modelling of Electron Device I/V Characteristics Through a Simplified Large-Signal Measurement Setup," *Int J RF and Microwave CAE,* vol. 15, no. 5, pp. 441-452, Sep. 2005.

[15] W. Ciccognani, F. Giannini, E. Limiti, P.E. Longhi, M.A. Nanni, A. Serino, C. Lanzieri, M. Peroni, P. Romanini, V. Camarchia, M. Pirola, G. Ghione, "GaN Device Technology: Manufacturing, Characterization, Modelling and Verification," in Proc. IEEE 14th Conference on Microwave Techniques, Prague, 2008, pp. 1–6.

[16] P. McGovern, J. Benedikt, P.J. Tasker, J. Powell, K.P. Hilton, J.L. Glasper, R.S. Balmer, T. Martin, M.J. Uren, "Analysis of DC-RF dispersion in AlGaN/GaN HFETs using pulsed I-V and time-domain waveform measurements," in Proc. IEEE MTT-S Int. Microwave Symp., Long Beach, 2005. [CD ROM]

[17] I. Angelov, C. Karnfelt, "Direct Extraction Techniques for Thermal Resistance of MESFET and HEMT Devices," in *Proc. IEEE Radio Frequency Integrated Circuits Symp.*, Honolulu, 2007, pp. 351–354.

[18] I. Schmale, G. Kompa, "A novel thermal resistance extraction technique for temperature-dependent FET modelling," in *Proc. Gallium Arsenide and Other Compound Semiconductor Application Symp.*, Amsterdam, 1998, pp. 416–420.

CHAPTER IV :

New Low-Frequency Model for Microwave Devices

Introduction

In this chapter a new modeling approach is presented accounting for the nonlinear description of low-frequency dispersive effects (due to thermal phenomena and traps) affecting electron devices. The model will be identified on the basis of measurements carried out with the measurement system described in the previous chapter.

The design of nonlinear amplifiers represents a fundamental topic for the microwave community as clearly demonstrated by the increasing number of books [1-5] dedicated to this issue in recent years. This is justified by the important role that power amplifiers play in microwave systems (e.g., satellite front-ends, base stations, mobile phones). The advent of GaN technology [6-8] has provided new stimuli in this design field foreseeing unbelievable performance in terms of power density, available power, drain efficiency, high voltage and high temperature operation.

A widely adopted tool for power amplifier design is represented by load-pull measurements [9-14], based on both passive or active load synthesis. Such a type of measurement systems, being able to synthesize the optimum load and source conditions at the design frequency, supplies the designer with very useful information. Nevertheless, a model is needed for different reasons: simulating the device behavior at the intrinsic device ports to assess the actual load-line at the

device resistive core (this is a fundamental issue especially for high-efficiency amplifier classes), verifying process dispersion influence on device performance, investigating device stability and wide-band behavior, and so on.
The identification of an electron device model, which aims to be a powerful design tool under different classes of amplifier operation, cannot neglect the dispersion presented by the electron device current\voltage characteristics related to traps and thermal effects [15-19]. These effects have to be accurately characterized especially when new, and as consequence immature, technologies are considered (e.g., GaN, InP), since low-frequency (LF) dispersion unquestionably represents a bottleneck in device performance.
Different models have been proposed by the microwave community in the last twenty years to correctly account for low-frequency dispersion: from the simplest, and probably the first one, [20] proposed by Camacho-Penalosa (which adopts an RC network) to more complex models based on look-up-table approaches (e.g., [21-22]). The major problem related to the last mentioned approaches is that, despite the great level of accuracy obtainable, they are rarely used by designers due to the considerable simulation time required and convergence problems.
As a matter of fact, models which are based on bias-independent parameters [23-29] represent the optimum compromise between accuracy and simulation time. Such a kind of descriptions is typically based on simplifying approximations of the complex phenomena related to low-frequency dispersion, as a consequence it can be inadequate when new technologies (where dispersive effects play a major role) have to be investigated. The aim of the model described in this chapter is to introduce a very general analytical formulation for the description of low-frequency dispersion affecting microwave devices, which clearly demonstrates as different approaches [24-27] published in recent years, can be enhanced in order to obtain acceptable prediction capability also in the presence of strong dispersion. In particular, the proposed formulation, which is justified both by theoretical and empirical considerations, allows to identify a limited set of bias-independent parameters which guarantees an excellent compromise between accuracy and simulation time. As a consequence, this modeling approach are particularly suitable for the design of power amplifiers based on the latest device technologies (e.g., GaN).

In order to demonstrate the goodness of the proposed approach, after describing the theoretical model formulation and discusses the effects of the single correction terms introduced, a large variety of experimental results are provided as validation.

4.1 Non linear modeling of Low frequency dispersion: model formulation

When dealing with operating frequencies where the dynamic effects associated to charge storage variations and/or finite transit times can be neglected (i.e., low-frequency dynamic regime), the vector i of the instantaneous currents of a microwave FET device (i.e., MESFET or HEMT) can be formulated as:

$$\underline{i} = \begin{bmatrix} i_g(t) \\ i_d(t) \end{bmatrix} = \begin{bmatrix} f_g\left(\underline{v}, X_\vartheta\right) \\ f_d\left(\underline{v}, X_T, X_\vartheta\right) \end{bmatrix} \qquad (4.1)$$

where $\underline{v}$ is the vector of the instantaneous voltages at the device ports while X_ϑ and X_T are state variables describing the device thermal state and trap state, respectively. The thermal state influences the gate current as demonstrated by different papers devoted to the thermal resistance characterization (e.g., [30]), which exploit the gate I\V characteristic as a thermal sensor. On the other hand the major influence of the trap and thermal states on the drain current has been widely discussed and demonstrated in the literature [15-29].

By considering microwave single- or two-tone[1] device operation with frequency components lying above[2] the cut-off frequencies of the LF dispersive effects (some hundreds of kilohertz), the device thermal and trap states can be considered as frozen to their average values, since they cannot change according to instantaneous signal variations. In this operating regime Eq. (4.1) can be rewritten as:

$$\underline{i} = \begin{bmatrix} i_g(t) \\ i_d(t) \end{bmatrix} = \begin{bmatrix} f_g\left(\underline{v}, X_\vartheta^0\right) \\ f_d\left(\underline{v}, X_T^0, X_\vartheta^0\right) \end{bmatrix} \qquad (4.2)$$

[1] In the case of two tone excitation the tone spacing has to be greater than the highest cut-off frequency associated to LF dispersive effects.

[2] Practically all of the models available in the literature do not deal with the problem of accurate modeling of the dynamic device response within the “trap bandwidth” and usually account for the transition between dc and low-frequency operation above trap cut-off through a single time-constant RC network.

where X_ϑ^0 and X_T^0 represent average values. It has been widely demonstrated, both by theoretical considerations [21-28] and experimental results [15-16], that these two state variables, in the particular operation considered, can be assumed dependent only on the vector $\underline{V}^0$ of the average values of the voltages applied at the device ports and on the average value of the channel temperature ϑ_j^0:

$$\begin{aligned} \vartheta_j^0 &= \vartheta_c + R_\vartheta P^0 \\ P^0 &= \frac{1}{T}\int_0^T p(t)\,dt = P_{dc} - P_{load} \end{aligned} \qquad (4.3)$$

where ϑ_c is the case temperature, R_ϑ the thermal resistance, P^0 the average power dissipated, $p(t)$ the instantaneous power, P_{dc} the power supplied by the bias system, and P_{load} the active power delivered to the load. From the previous considerations, and considering Eq. (4.3), it follows that the trap and thermal state variables can be expressed as:

$$\begin{bmatrix} X_T^0 \\ X_\vartheta^0 \end{bmatrix} = \begin{bmatrix} f_T\left(\underline{V}^0, \vartheta_j^0\right) \\ f_\vartheta\left(\vartheta_j^0\right) \end{bmatrix} = \begin{bmatrix} f_T\left(\underline{V}^0, P^0, \vartheta_c\right) \\ f_\vartheta\left(P^0, \vartheta_c\right) \end{bmatrix} \qquad (4.4)$$

where the dependence of the trap state on the thermal state has also been accounted for [18], [23].

The present chapter is focused on the description of the device drain current, whereas the gate current dispersion will be neglected. Such an approximation is justified since the gate current thermal dependence does not greatly affect model prediction capability under typical power amplifier operation. As a matter of fact, to put in evidence such a dispersion, important variations of the case temperature (i.e., 40-50 °C) and\or high dissipation bias conditions (e.g., setting the gate bias voltage V_g^0 at the forward conduction threshold of the gate\source diode and the drain bias voltage V_d^0 in the saturation region) are needed: such operating regimes are clearly not particularly interesting in power amplifier design.

By considering Eq. (4.4), the drain current equation in (4.2) can be expressed as:

$$i_d(t) = f_d\left(\underline{v}, X_T^0, X_\vartheta^0\right) = F\left(\underline{v}, \underline{V}^0, P^0, \vartheta_c\right) \qquad (4.5)$$

The algebraic function F can be defined in different ways, nevertheless it has to satisfy some physical requirements. A most important one being that under DC operation it has to coincide with the device static characteristics $F\left(\underline{v}, \underline{V}^0, P^0, \vartheta_c\right)\Big|_{dc} = F_{dc}\left(\underline{v}, \vartheta_c\right)$. For such a reason it is quite intuitive to adopt a formulation which describes the dynamic current deviations with respect to DC, by modifying the device DC characteristic:

$$i_d(t) = F\left(\underline{v}, \underline{V}^0, P^0, \vartheta_c\right) = \left[1 + \Delta_m\left(\underline{v}, \underline{V}^0, P^0\right)\right] \cdot F_{dc}\left(\underline{v_x}, \vartheta_c\right)$$
$$\underline{v_x} = \begin{bmatrix} v_{gx}(t) \\ v_{dx}(t) \end{bmatrix} = \begin{bmatrix} v_g(t) + \Delta_g\left(\underline{v}, \underline{V}^0, P^0\right) \\ v_d(t) \cdot \left(1 + \Delta_d\left(\underline{v}, \underline{V}^0, P^0\right)\right) \end{bmatrix} \qquad (4.6)$$

where $\underline{v_x}$ is the vector of the modified voltages, whereas the correction terms Δ_m, Δ_g, Δ_d, account for the drain current deviations related to LF dispersion.

The particular expressions adopted to “modify” the DC characteristic are justified both by considering previous approaches [23-27] and by empirical observations; moreover, their validity is confirmed by the experimental results provided in the following. In particular, the formulation adopted for the modified drain voltage v_{dx} allows to satisfy the physical constraint that, under low-frequency operation, the drain current has to be null when the instantaneous drain voltage is null. Moreover, the dependence on the case temperature (which is considered constant under device operation) has been included only in the DC characteristic F_{dc}.

The correction terms Δ can be conveniently expressed as a function of purely dynamic terms defined as the difference between the instantaneous values of the controlling electrical quantities and the corresponding average values:

$$\begin{aligned}\Delta_m(t) &= f_{\Delta m}\left(\delta_{vg},\delta_{vd},\delta_p\right)\\ \Delta_g(t) &= f_{\Delta g}\left(\delta_{vg},\delta_{vd},\delta_p\right)\\ \Delta_d(t) &= f_{\Delta d}\left(\delta_{vg},\delta_{vd},\delta_p\right)\end{aligned} \tag{4.7}$$

with

$$\begin{aligned}\delta_{vg} &= v_g(t) - V_g^0\\ \delta_{vd} &= v_d(t) - V_d^0\\ \delta_p &= p(t) - P^0\end{aligned} \tag{4.8}$$

An analytical formulation of the functions f_Δ can be obtained by adopting a Taylor expansion. By focusing on the one-dimensional case for the sake of simplicity, we can write for any of the f_Δ functions:

$$\begin{aligned}f_\Delta(\delta_i) &= \sum_{k=0}^{\infty}\left[\left.\frac{\partial f^k}{\partial \delta_i}\right|_{\delta_i=\delta_{i0}} \cdot \frac{\left(\delta_i-\delta_{i0}\right)^k}{k!}\right] =\\ &= \sum_{r=0}^{\infty}\alpha_r \delta_{io}^r + \sum_{p=1}^{\infty}\sum_{q=1}^{\infty}\alpha_{pq}\delta_i^p\delta_{i0}^q + \sum_{n=1}^{\infty}\alpha_n\delta_i^n\end{aligned} \tag{4.9}$$

As previously observed, under DC operation the function F has to coincide with the DC one in Eq. (4.6); this implies that under DC operation the correction terms $\Delta = f_\Delta$ (δ_i) have to be null. Such a condition can be easily verified, without introducing any approximation, by posing δ_{i0} equal to zero in (4.9); thus, for the multidimensional case, the generic f_Δ function reduces to:

$$f_\Delta\left(\delta_1,\delta_2,\ldots,\delta_n\right) = \sum_{n1=0}^{\infty}\cdots\sum_{nn=0}^{\infty}{}_{\left(n1+\ldots+nn\neq 0\right)}\alpha_{n1,\ldots,nn}\delta_1^{n1}\cdot\ldots\cdot\delta_n^{nn} \tag{4.10}$$

and, finally, the correction terms become:

$$\Delta_m(t)=\sum_{gm=0}^{n1}\sum_{dm=0}^{n2}\sum_{pm=0}^{n3}{}_{(gm+dm+pm\neq 0)}\alpha_{gm,dm,pm}^{m}\delta_{vg}^{gm}\delta_{vd}^{dm}\delta_{p}^{pm}$$
$$\Delta_g(t)=\sum_{gg=0}^{n4}\sum_{dg=0}^{n5}\sum_{pg=0}^{n6}{}_{(gg+dg+pg\neq 0)}\alpha_{gg,dg,pg}^{g}\delta_{vg}^{gg}\delta_{vd}^{dg}\delta_{p}^{pg} \qquad (4.11)$$
$$\Delta_d(t)=\sum_{gd=0}^{n7}\sum_{dd=0}^{n8}\sum_{pd=0}^{n9}{}_{(gd+dd+pd\neq 0)}\alpha_{gd,dd,pd}^{d}\delta_{vg}^{gd}\delta_{vd}^{dd}\delta_{p}^{pd}$$

where the $\alpha_{x,y,z}$ coefficients are the bias-independent model parameters to be identified.

Equations (4.6) and the correction terms (4.11) define a general purpose nonlinear model for dispersive effects which satisfies physical and experimental evidence. It can be applied starting from any possible description of an electron device DC characteristics (e.g., analytical, look-up-table based, etc.). Different model formulations reduce to (4.6), (4.11) under simplifying assumptions [24-27].

In the next paragraph the effects of the correction terms (4.11) are analyzed in order to derive guidelines for the optimal choice of the model parameters.

4.2 *Correction Terms Effects*

The deviations existing between static and dynamic device output characteristics, measured at operating frequencies where the nonlinear dynamic effects associated to charge storage variations can be totally neglected, are schematically shown in Fig. 4.1. In this figure, the knee walkout (KW) of the dynamic characteristics, the negative slope (NS) of the dc characteristic in the saturation region, and the saturation current collapse (CC)[3] are put in evidence. All these effects globally contribute to decrease device performance under dynamic operation and, as a consequence, have to be correctly accounted for.

The knee walkout can be accurately predicted by modeling the different slopes shown by the dynamic characteristics in the linear region. Such a kind of discrepancy can be simply accounted for by a correction in the drain voltage dependence of the

[3] The current collapse can be also defined with respect to a pulsed characteristic measured by exploiting a bias condition which guarantees both no power dissipation and channel formation (e.g., V_g^0 = 0 V and V_d^0 = 0 V), nevertheless the definition here adopted is more congruent with the model theoretical formulation.

static characteristic, that means by the correction term[4] Δ_d in (4.6). It has been largely demonstrated (e.g., [16-18]) that the knee walkout monotonically increases by increasing the drain bias voltage V_d^0; as a consequence the contribution δ_{vd} has to be necessarily considered. If a significant dependence on the gate bias voltage is present, also the contribution δ_{vg} should be included. Since the correction term Δ_d only accounts for small deviations of the characteristic slope in the linear region, it is meaningless to exceed in its polynomial degree: a first order expansion is typically adequate.

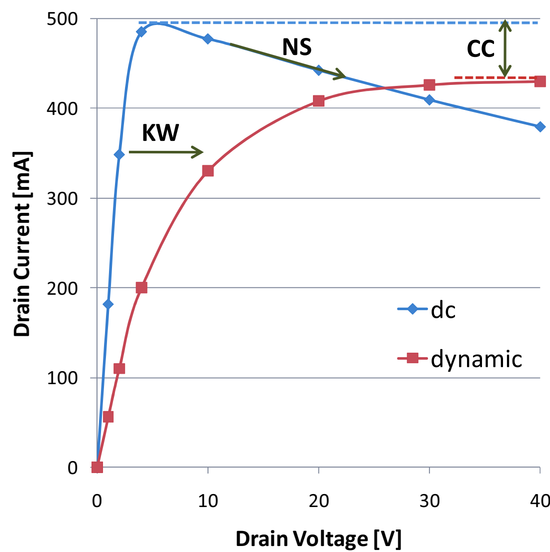

Fig. 4.1. Schematic representation of the differences existing between dc and dynamic device characteristics.

the knee walkout monotonically increases by increasing the drain bias voltage V_d^0; as a consequence the contribution δ_{vd} has to be necessarily considered. If a significant dependence on the gate bias voltage is present, also the contribution δ_{vg} should be included. Since the correction term Δ_d only accounts for small deviations of the characteristic slope in the linear region, it is meaningless to exceed in its polynomial degree: a first order expansion is typically adequate. When dynamic operation is considered, the device thermal state is defined by Eq. (4.3); thus, differently from the DC ones, the dynamic characteristics do not show any negative slope in the saturation region: this behavior can be accounted for through the multiplying

[4] This term is conceptually similar to the effect of a parasitic drain resistance which, causing a voltage drop, is able to modify the slope of the dc characteristics in the linear region.

correction term Δ_m. Since thermal effects are mainly responsible for such a deviation, the contribution δ_p has to be introduced. It can be observed that dynamic characteristics measured under the same thermal state (e.g., under no power dissipation), but starting from different bias conditions, can show different slopes in the saturation region [15-17] (e.g., in Fig. 2.2 in chapter 2). In this respect it is necessary to introduce also the contributions deriving from the deviations δ_{vg} and δ_{vd}. Since the correction term Δ_m has only to account for deviations related to the characteristic slope in the saturation region, also in this case, it is unfruitful to exceed in its polynomial degree, and a first order expansion can be adopted. It should be noticed that in [24] and [27] the authors obtained very good prediction capability without adopting such a term. This is coherent with the low-power device considered there, as can be seen looking at the DC characteristics which do not show any negative slope.

The current collapse essentially arises from the presence of surface trap states [16-17] and is accounted for by the last correction term Δ_g. Such a phenomenon is strongly dependent on both the bias condition and the device thermal state, so all the δ-deviations have to be exploited. Moreover, due to its very complex behavior, when new device technologies are investigated, a high-order polynomial degree may be required.

The theoretical formulation in equations. (4.6) and (4.11) clearly shows that the *mixed correction terms*, arising from the mixed terms in the Taylor expansion, have to be accounted for. These terms were completely and arbitrarily neglected in [26-27] and this is probably the reason why a high-order polynomial was necessary, in those particular cases, for the correction term Δ_d. Nevertheless, careful considerations are needed before increasing the order of such a correction term since, beside the motivations previously discussed, if Δ_d becomes smaller than -1, the drain current goes negative in correspondence of positive drain voltage values. Obviously such a behavior is completely unphysical under low-frequency operation. As a matter of fact, it is strongly suggested to maintain the polynomial order of the correction term Δ_d as low as possible.

Since the theoretical formulation here proposed is based on bias-independent parameters, it could be easily identified, through least-square algorithms, by

exploiting low-frequency small-signal measurements carried out under different bias-conditions at a single frequency (e.g., 40 MHz) above the cut-off of low-frequency dispersive effects (the measurement number depending on the number of parameters exploited). As a matter of fact, since the proposed approach is oriented to nonlinear amplifier design, it is preferable to base the identification procedure on large-signal measurements carried out under pulsed [15] and\or sinusoidal [31] excitations.

4.3 Experimental results

The presented model formulation was exploited to characterize the nonlinear dynamic behavior of a 0.7x800 μm^2 GaN HEMT device. As a first step a suitable parasitic network was extracted by adopting a conventional technique based on "cold" scattering parameter measurements (V_d^0 = 0 V).
In the characterization phase the low-frequency time-domain load-pull measurement system presented in previous chapter, based on sinusoidal excitations at 2 MHz [31], was adopted. Two 50 Ω signal sources allow to impose the amplitudes of the incident-waves applied at the gate and drain ports and their relative phase. As previously said the operating frequency has been chosen above the cut-off of LF dispersive effects but low enough to neglect dynamic effects related to the device reactive parasitic elements and the high-frequency capacitive effects. Different papers (e.g., [14]) document the influence of dispersive phenomena (essentially related to thermal effects) at frequencies above the frequency exploited in the present work. As demonstrated in Chapter 2, for frequencies greater than 2MHz changes in the output conductance is negligible compared to the value in DC.
Nevertheless, to further validate this hypothesis, measurements were carried out at three different fundamental frequencies (2 MHz, 10 MHz, and 20 MHz) on the selected GaN device under class-A operation and 50 Ω loading condition. Fig. 4.2 shows the results of these measurements. Once again it is evident that no major deviations arise by changing the characterization frequency. This confirms the correctness of the chosen frequency (i.e., 2 MHz) to characterize dispersion effects and that negligible uncertainty is introduced by neglecting "faster dynamics" of low-

frequency dispersion[5].

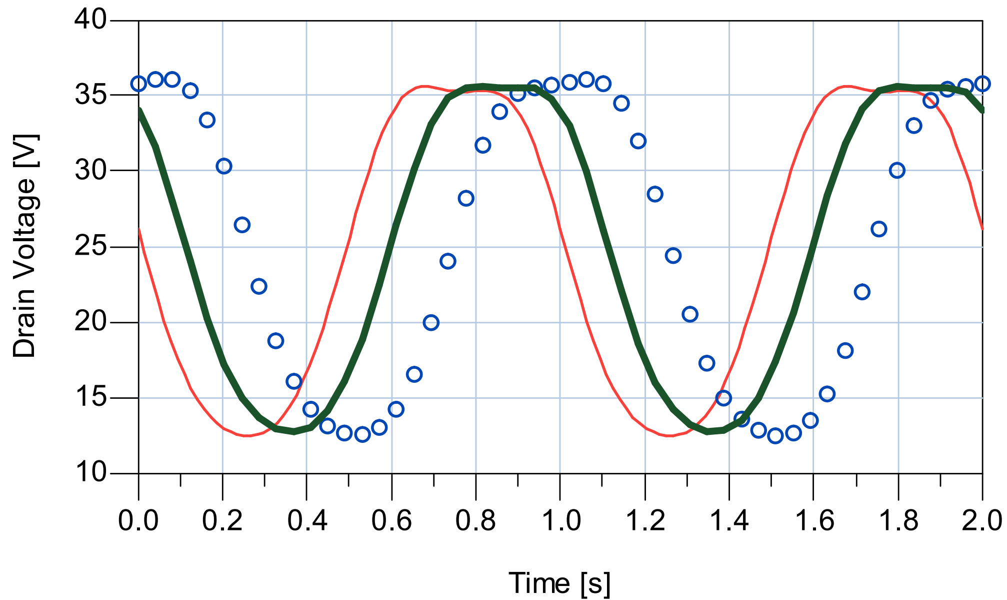

Fig. 4.2. Measurements carried out at different frequencies to assess the correctness of the chosen characterization frequency (thin line - 2 MHz, thick line - 10 MHz, circles - 20 MHz). The waveform time scale has been properly normalized to fit two periods; moreover a time shift has been introduced between waveforms to make appreciable the differences

Fig. 4.3 shows two measurement sets, carried out by means of the low-frequency load-pull setup, starting from two different bias conditions: V_g^0 = -4 V, V_d^0 = 25 V (corresponding to class-B operation) and V_g^0 = -2 V, V_d^0 = 25 V (corresponding to class-A operation). For each set the different load-lines were obtained by imposing constant amplitude of the gate incident signal (which is chosen to dynamically reach the device output characteristic at v_g = 0 V) and sweeping the amplitude of the drain incident signal. The relative phase is maintained constant to 180°. Also the DC characteristic for v_g = 0 V is reported in order to put in evidence the current collapse. As can be clearly seen in Fig. 4.3, the device shows negligible dependence of the knee-walkout on the gate bias condition.

[5] This is also confirmed by the large number of papers devoted to GaN device characterization (e.g., [17]) which, for the low-frequency characterization, adopt pulsed measurements setting the pulse width to 500 ns or more.

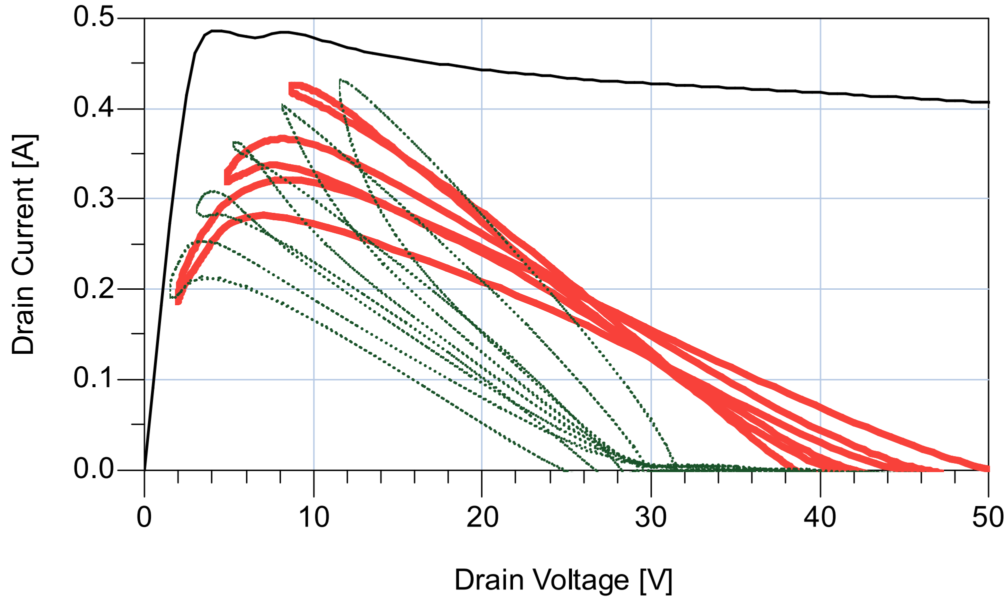

Fig. 3. Measurements performed on the GaN device under test at 2 MHz, the two sets have the same drain bias condition (V_d^0 = 25 V) and different gate bias values V_g^0 = -2 V (continuous line) and V_g^0 = -4 V (dotted line). Class-A operation: amplitude of the input incident signal A_g = 1 V, amplitude of the output incident signal 3.1 V < A_d < 11 V, relative phase $\Delta\phi$ = 180°. Class-B operation: A_g = 2 V, 1.4 V < A_d < 9.8 V, $\Delta\phi$ = 180°. Also the dc characteristic for v_g = 0 V is shown

Following the guidelines discussed in the previous section, the formulation adopted for the considered case study is:

$$\begin{aligned}
\Delta_m(t) &= \alpha_{1,0,0}^{m}\delta_{vg} + \alpha_{0,1,0}^{m}\delta_{vd} + \alpha_{0,0,1}^{m}\delta_{p} \\
\Delta_g(t) &= \alpha_{1,0,0}^{g}\delta_{vg} + \alpha_{0,1,0}^{g}\delta_{vd} + \alpha_{0,0,1}^{g}\delta_{p} + \alpha_{2,0,0}^{g}\delta_{vg}^{2} + \alpha_{0,2,0}^{g}\delta_{vd}^{2} + \\
&\quad + \alpha_{0,0,2}^{g}\delta_{p}^{2} + \alpha_{1,1,0}^{g}\delta_{vg}\delta_{vd} + \alpha_{1,0,1}^{g}\delta_{vg}\delta_{p} + \alpha_{0,1,1}^{g}\delta_{vd}\delta_{p} \\
\Delta_d(t) &= \alpha_{0,1,0}^{d}\delta_{vd}
\end{aligned} \tag{4.12}$$

where, for the gate voltage correction term Δ_g , a second order polynomial has been found adequate. Moreover, in the drain voltage correction term Δ_d, the contribution deriving from the deviations δ_{vg} has been neglected accordingly to the negligible dependence of the knee-walkout on the gate bias condition shown in Fig. 4.3.

Although the correction technique here presented can be applied to any DC drain current description [27], in this paper a look-up-table approach has been used for the static characteristic F_{dc} with the specific aim of quantifying the level of accuracy achievable with the deviation model presented. In particular this avoids introducing

errors related to the static behavior approximation through analytical functions (e.g., smoothing functions and the absence of kink effects which are instead present in the DC behavior as shown in Fig. 4.3).

Two sets of low-frequency measurements were exploited in the identification phase (bias conditions: V_g^0 = -4 V, V_d^0 =25 V and V_g^0 = -3 V V_d^0 = 35 V). The values obtained for the model parameters are reported in Table 4.1.

Parameter	**Value**	**Parameter**	**Value**
$\alpha^m_{1,0,0}$	0.016 V^{-1}	$\alpha^g_{0,2,0}$	0 V^{-1}
$\alpha^m_{0,1,0}$	0.017 V^{-1}	$\alpha^g_{0,0,2}$	0.0043 $A^{-2}V^{-1}$
$\alpha^m_{0,0,1}$	0.059 W^{-1}	$\alpha^g_{1,1,0}$	0.00037 V^{-1}
$\alpha^g_{1,0,0}$	-0.024	$\alpha^g_{1,0,1}$	0.019 W^{-1}
$\alpha^g_{0,1,0}$	-0.012	$\alpha^g_{0,1,1}$	0.0054 W^{-1}
$\alpha^g_{0,0,1}$	-0.077 A^{-1}	$\alpha^d_{0,1,0}$	0.025 V^{-1}
$\alpha^g_{2,0,0}$	-0.032 V^{-1}		

Table 4.1 Low-Frequency Model Parameters for the Considered 0.7-μm GaN HEMT Device

Fig. 4.4 compares the model prediction with one of the identification measurement sets, while in Table 4.2 predicted values of the average drain current are listed. As well known it is very difficult to correctly estimate such a quantity, which is of critical importance in nonlinear amplifier design. A maximum percent deviation of 5% is observed here between measurements and predictions.

A_d [V]	***Measured value [mA]***	***Predicted value [mA]***
1.4	127	132
2.6	121	125
4.5	114	118
7.1	101	106
9.8	80	84

Table 4.2. Model Prediction of the Average Drain Current Under Dynamic Operation (V_g^0 = -4 V , V_d^0 = 25 V)

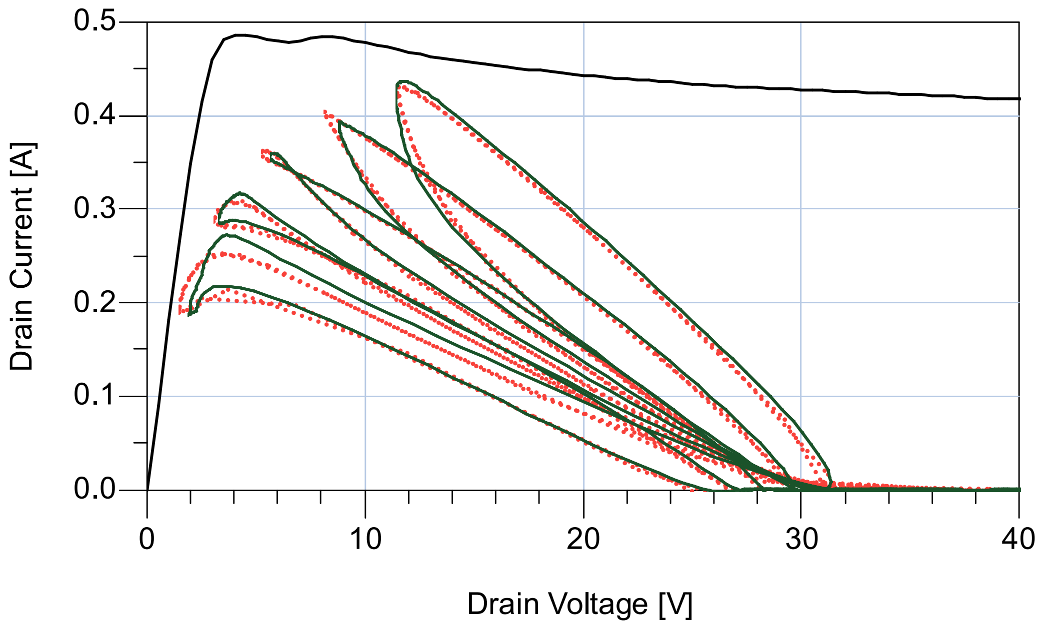

Fig. 4.4. Measurements (dotted line) carried out on the GaN device under test are compared with model predictions (continuous line). Frequency of operation 2 MHz, class-B bias condition (V_g^0 = -4 V, V_d^0 = 25 V), amplitude of the input incident signal A_g = 2 V, amplitude of the output incident signal 1.4 V < A_d < 9.8 V, relative phase $\Delta\phi$ = 180°.

In Table 4.3 the predicted and measured values of total harmonic distortion (THD) are compared. Also in this case the agreement is excellent. Identical results were obtained for the other measurement sets exploited in the identification phase.

A_d [V]	Measured value [%]	Predicted value [%]
1.4	23.1	22.2
2.6	15.0	14.2
4.5	10.4	10.2
7.1	7.3	7.6
9.8	5.6	6.5

Table 4.3. Model Prediction of the Total Harmonic Distortion (V_g^0 = -4 V , V_d^0 = 25 V)

The proposed approach was validated by carrying out several measurements under very different classes of operation to put in evidence the model accuracy.

In Fig. 4.5 measurements carried out starting from a strong pinch-off quiescent condition (V_g^0 = -7 V, V_d^0 = 30 V) are shown. Such a regime of operation strongly emphasizes the influence of trapping states. In fact the very important knee walkout and current collapse are well evident. The excellent prediction capability of the developed formulation is also confirmed in Tables 4.4 and 4.5 where the comparisons between measured and predicted values of the average drain current and total harmonic distortion are reported.

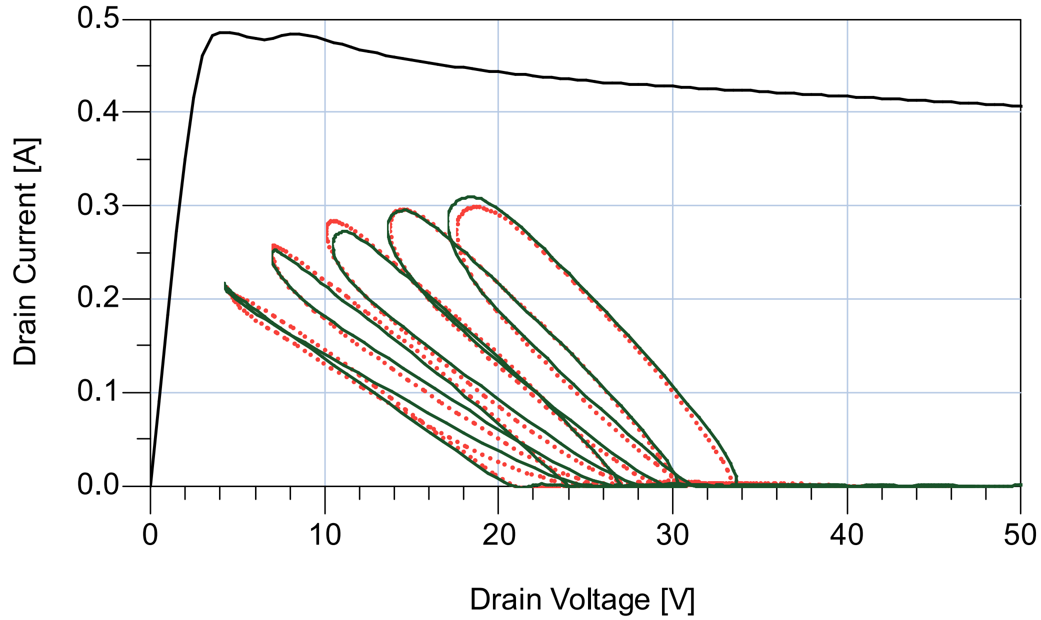

Fig. 4.5. Measurements (dotted line) performed on the GaN device under test are compared with model predictions (continuous line). Frequency of operation 2 MHz, strong pinch-off bias condition (V_g^0 = -7 V, V_d^0 = 30 V), amplitude of the input incident signal A_g = 3.5 V, amplitude of the output incident signal 1.1 V < A_d < 9.8 V, relative phase $\Delta\phi$ = 180°.

***A_d* [V]**	***Measured value [mA]***	***Predicted value [mA]***
1.1	56	60
3.2	56	57
5.3	54	54
7.5	50	51
9.8	43	46

Table 4.4. Model Prediction of the Average Drain Current Under Dynamic Operation (V_g^0 = -7 V , V_d^0 = 30 V)

***A_d* [V]**	***Measured value [%]***	***Predicted value [%]***
1.1	60.6	61.6
3.2	32.6	34.4
5.3	21.6	22.5
7.5	14.9	16.0
9.8	9.6	11.6

Table 4.5. Model Prediction of Total Harmonic Distortion (V_g^0 = -7 V , V_d^0 = 30 V)

In Fig. 4.6.a) the time-domain drain waveforms, for the particular case of output incident signal amplitude A_d = 1.1 V, are shown: the 40% current collapse is correctly predicted by the proposed approach.

Fig. 4.6.b) shows the time-domain drain waveforms for the class-A bias condition (V_g^0 = -2 V, V_d^0 = 25 V). Also in this case the high level of prediction accuracy is evident. In particular in the knee region the current sinking in correspondence to the voltage minimum peak is perfectly reproduced.

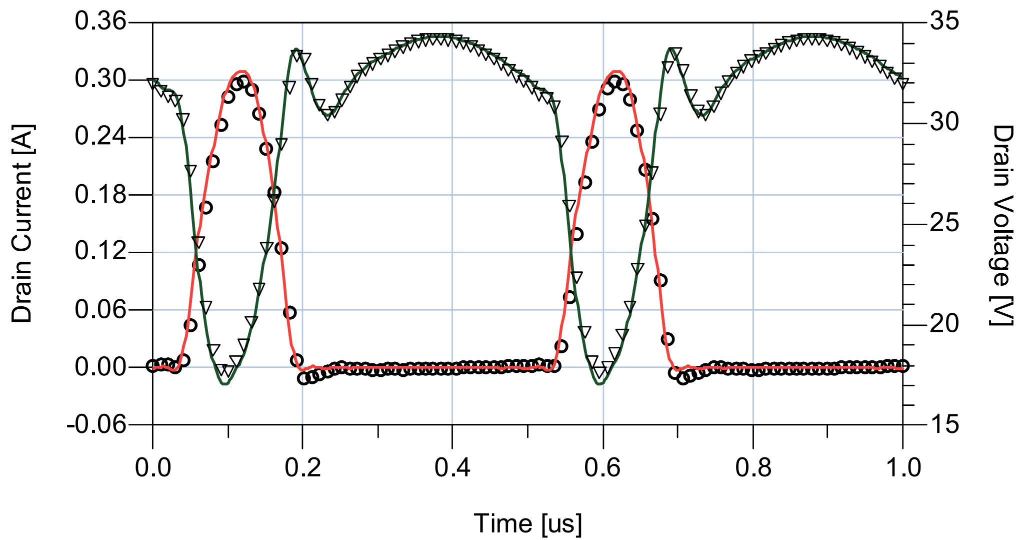

a)

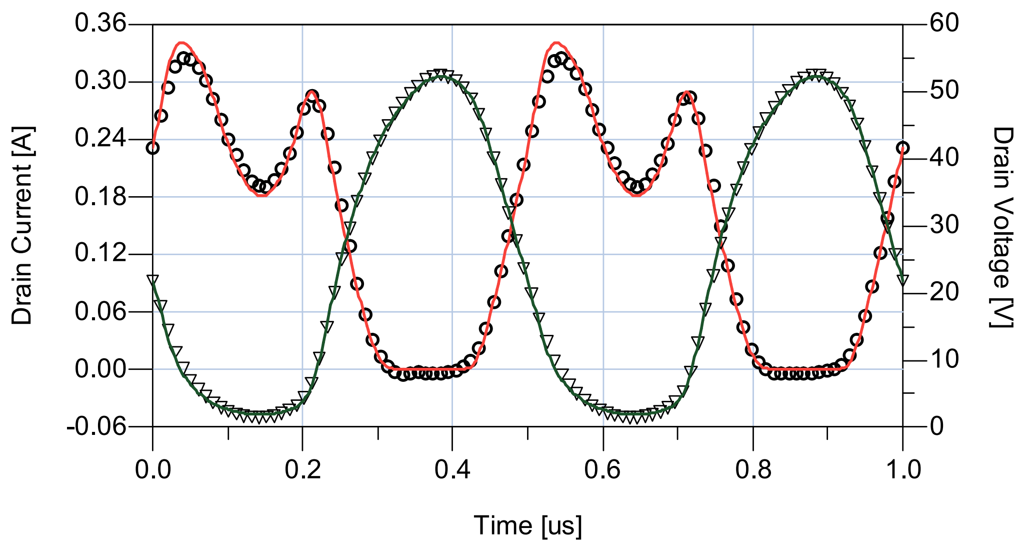

b)

Fig. 4.6. Measured drain current (circles) and voltage (triangles) compared to respective model predictions (continuous line). a) V_g^0 = -7 V, V_d^0 = 30 V, A_g = 3.5 V, A_d = 1.1 V, $\Delta\phi$ = 180°. b) V_g^0 = -2 V, V_d^0 = 25 V, A_g = 1 V, A_d = 11 V, $\Delta\phi$ = 180.

In order to assess the accuracy level obtainable by the proposed approach under high-frequency operation, the identified LF model was embedded into a large-signal

device model for microwave applications[6] [32]. To this aim, bias- and frequency-dependent S-parameter measurements were carried out in the frequency range 40 MHz – 40 GHz by means of an Anritsu 37397D vector network analyzer. From a theoretical point of view also dispersion on capacitance should be accounted for, nevertheless such a kind of effect is of minor extent with respect to the dynamic deviations of the drain current. As a matter of fact, capacitance dispersion has been regularly neglected so far in electron device models oriented to power amplifier design [33-34]. The developed approach was validated by exploiting a time-domain load-pull system [13]. More precisely, a LSNA-based active load-pull setup has been employed for this work. The drain load was synthesized by sending toward the device output port a power wave, at the fundamental frequency of 4 GHz, with properly controlled amplitude and phase. Moreover, to cover a wide region of the DUT characteristic and synthesize loads close to the edge of the Smith chart, power amplifiers were inserted at the input and output device ports. Also in this context the model predictions were found in good agreement with measurements under different bias conditions as clearly shown in Fig 4.7.

[6] It is worth noticing that under high-frequency operation the term *p(t)* has to be calculated by considering only the purely algebraic part of the drain current (6).

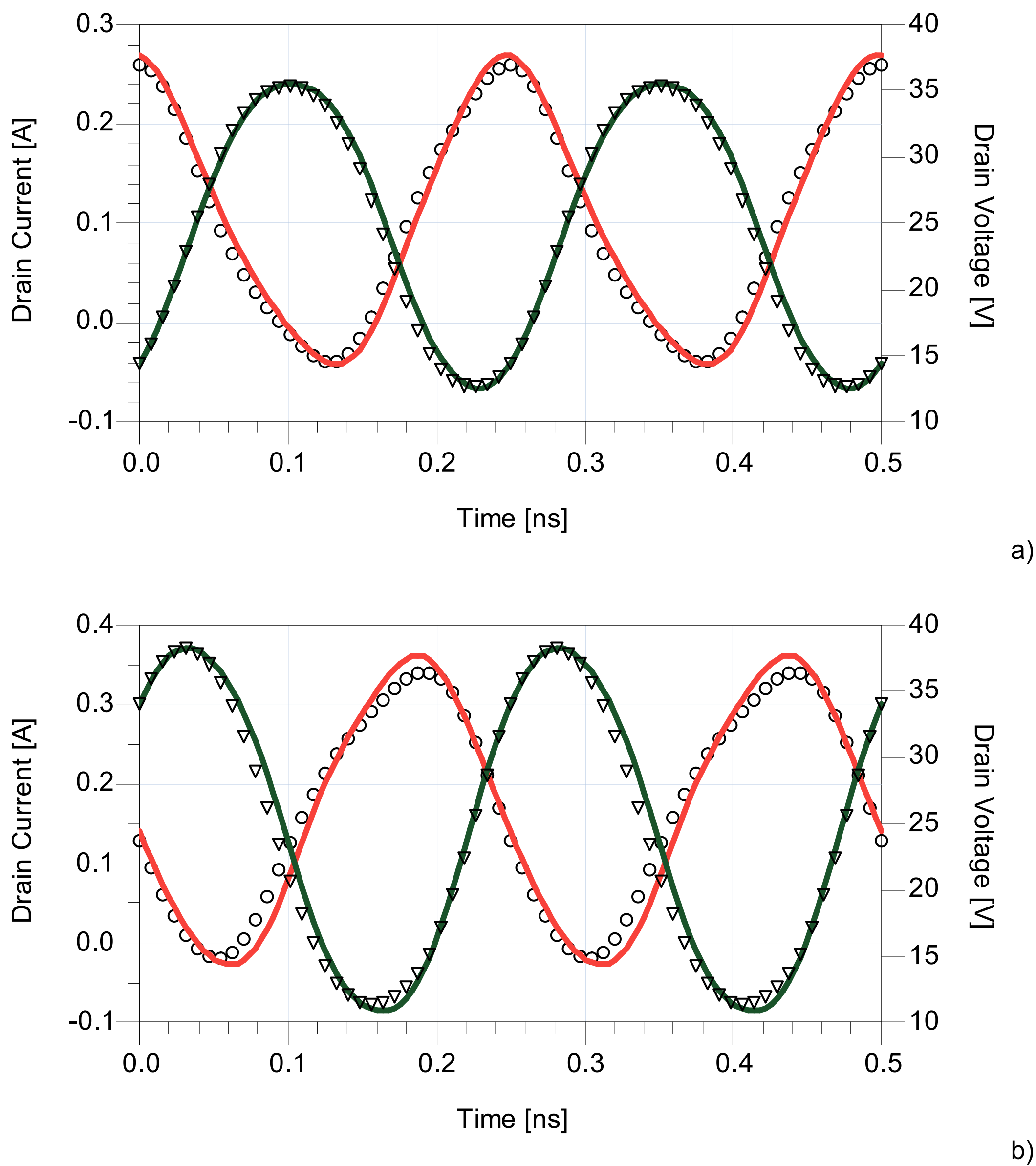

Fig. 4.7. Active load-pull measurements at 4 GHz. Measured drain current (circles) and voltage (triangles) compared to corresponding model predictions (continuous line). a) V_g^0 = -3.25 V, V_d^0 = 25 V, Z_L = 71.9 + j*39.4 Ω. b) V_g^0 = - 2.25 V, V_d^0 = 25 V, Z_L = 66.6 + j*41.5 Ω

Load-pull measurements were also carried out by exploiting a 4-26 GHz load-pull system [11], which enables device source and load impedances at the fundamental frequency to be controlled. In particular, third-order intermodulation (IMD) measurements were performed at 4 GHz (tone spacing 10 MHz) under class A operation (Fig. 4.8.a and 4.8.b). The level of IMD components is referred to the carrier level. The prediction accuracy clearly puts in evidence that the provided description is adequate to accurately model higher-order partial derivatives of the nonlinear electrical variables.

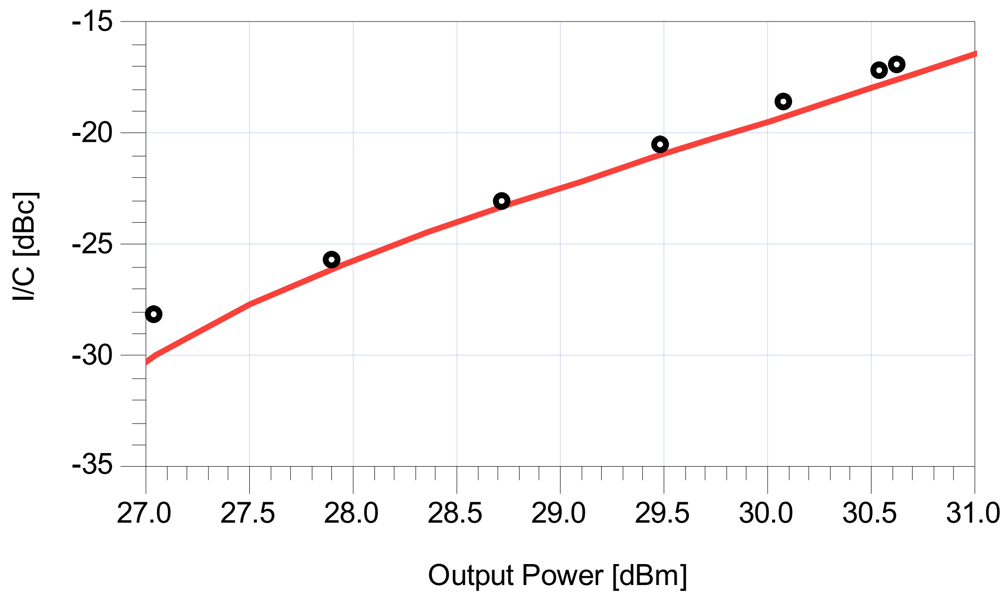

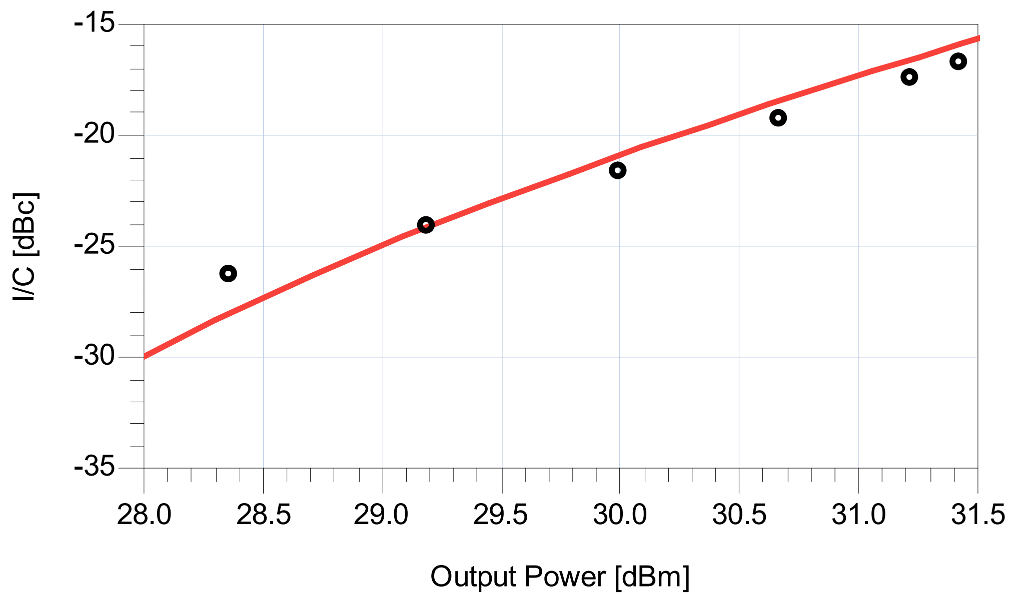

Fig. 4.8. Third-order I/C versus output power measurements (symbols) carried out at 4 GHz and model predictions (continuous lines) obtained by the proposed formulation. Bias condition V_g^0 = -2 V, V_d^0 = 25 V, source impedance Z_S = 9.07 + j*14.62 Ω and load impedance a) Z_L = 63.23 + j*4.63 Ω and b) Z_L = 82.37 + j*33.93 Ω.

Single tone measurements were also performed at 4 GHz choosing two typical operating conditions: class A (Fig. 4.9.a) and 4.9.b)) and class AB (Fig. 4.10.a) and 4.10.b)). The good agreement obtained between model predictions and measurements for all the considered figures of merit (gain, output power, average drain current, and PAE) as well as the fast simulation times demonstrates the optimum compromise achievable by adopting the present formulation.

In order to assess the accuracy improvement achieved by (4.12), Fig. 4.9 and 4.10 also show the prediction results obtained through a simplified formulation where only the three correction terms reported in Table 4.6 are considered. This formulation practically coincides with [25] that can be considered representative of models [23-27]. The two formulations show the same high accuracy level under small-signal condition, nevertheless under nonlinear operation the improvement deriving from considering additional model parameters is well evident.

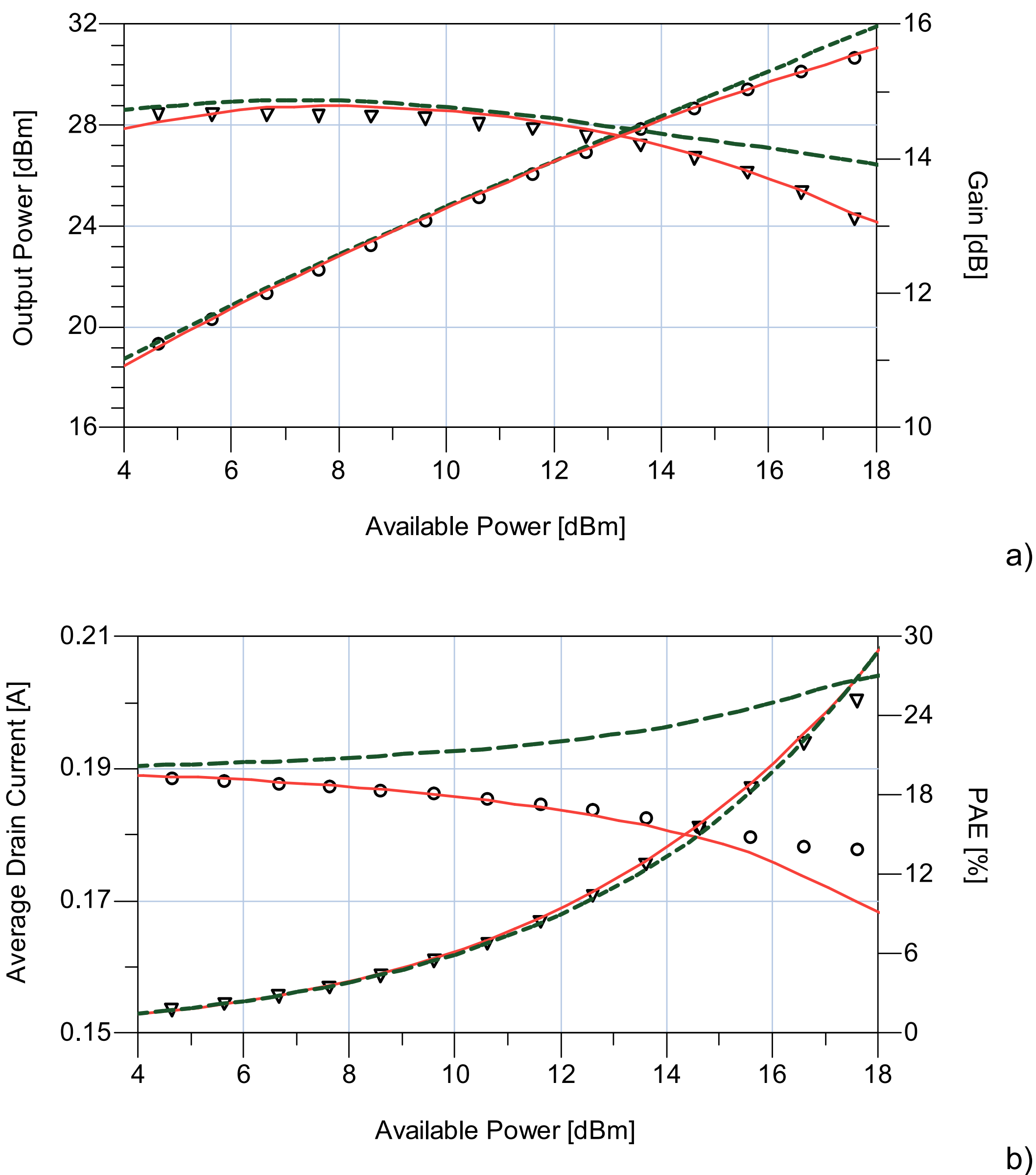

Fig. 4.9. Comparisons between load-pull measurements (symbols) carried out at 4 GHz and model predictions obtained by the proposed formulation (continuous lines) and a simplified one (dotted lines). Output power (circles), gain (triangles), average drain current (circles) and power added efficiency (triangles). a) and b) Bias condition V_g^0 = -2 V, V_d^0 = 25 V, source impedance Z_S = 4.56 + j*8.11 Ω and load impedance Z_L = 42.63 + j*55.02 Ω.

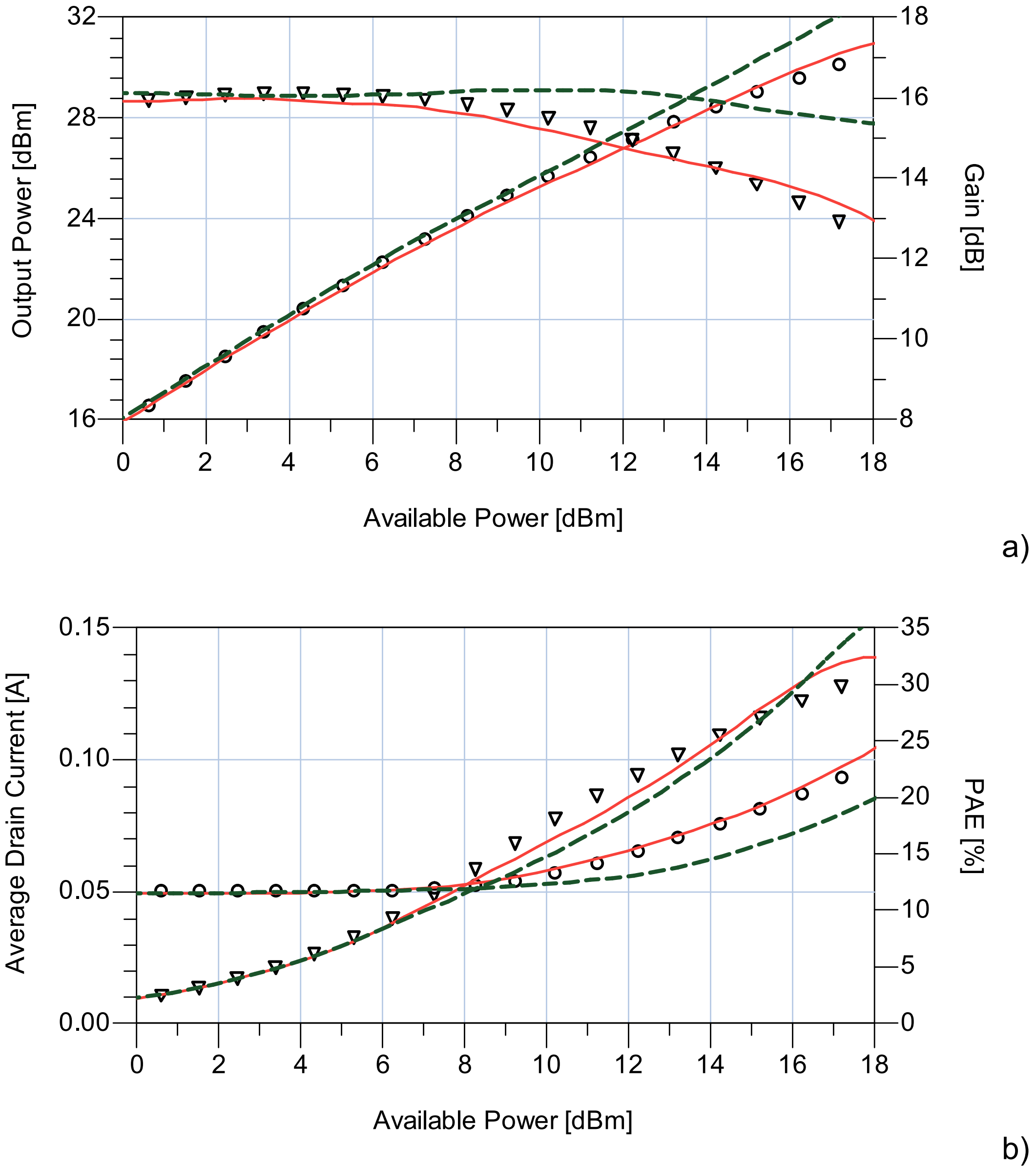

Fig. 4.10. Comparisons between load-pull measurements (symbols) carried out at 4 GHz and model predictions obtained by the proposed formulation (continuous lines) and a simplified one (dotted lines). Output power (circles), gain (triangles), average drain current (circles) and power added efficiency (triangles). a) and b) Bias condition V_g^0 = -3 V, V_d^0 = 35 V, source impedance Z_S = 11.19 + j*11.73 Ω and load impedance Z_L = 65.89 + j*98.84 Ω.

Parameter	***Value***	***Parameter***	***Value***
$\alpha^m_{0,0,1}$	0.0022 W^{-1}	$\alpha^g_{1,0,0}$	-0.21
$\alpha^g_{0,1,0}$	0.0035		

Table 4.6. Simplified Model Parameters for the Considered 0.7-μm GaN HEMT Device

CONCLUSIONS

A very general formulation has been discussed which allows to correctly account for low-frequency dispersion affecting FET electron devices. The proposed modeling approach has been validated under very different operations both at low- and high-frequencies definitely demonstrating its validity for power amplifier design.

References

[1] S. Marsh, *Practical MMIC Design*. Norwood, MA: Artech House, 2006.

[2] M. Albulet, *RF Power Amplifiers*. Atlanta, GA: Noble Publishing Corporation, 2001.

[3] S. C. Cripps, *RF Power Amplifiers for Wireless Communication*. Norwood, MA: Artech House, 1999.

[4] S. C. Cripps, *Advanced Techniques in RF Power Amplifier Design*. Norwood, MA: Artech House, 2002.

[5] F. Giannini, G. Leuzzi, *Nonlinear Microwave Circuit Design*. Chichester, England: Wiley, 2004.

[6] U. K. Mishra, P. Parikh, Yi-Feng Wu "AlGaN/GaN HEMTs-an overview of device operation and applications," *Proceedings of the IEEE*, vol. 90, no. 6, pp. 1022–1031, Jun. 2002.

[7] P. Colantonio, F. Giannini, R. Giofre, E. Limiti, A. Serino, M. Peroni, P. Romanini, C. Proietti, "A C-band high-efficiency second-harmonic-tuned hybrid power amplifier in GaN technology," *IEEE Trans. On Microw. Theory and Tech.*, vol. 54, no. 6, pp. 2713-2722, Jun. 2006.

[8] M. Helaoui, F. M. Ghannouchi, "Optimizing Losses in Distributed Multiharmonic Matching Networks Applied to the Design of an RF GaN Power Amplifier With Higher Than 80% Power-Added Efficiency," *IEEE Trans. On Microw. Theory and Tech.*, vol. 57, no. 2, pp. 314-322, Feb. 2009.

[9] J.M. Cusak, S.M. Perlow, B.S. Perlman, "Automatic load contour mapping for microwave power transistors," *IEEE Trans. On Microw. Theory and Tech.*, vol. 22, no. 12, pp. 1146-1152, Dec. 1974.

[10] A. Ferrero, V. Teppati, "Accuracy Evaluation of On-Wafer Load-Pull Measurements," in *Proc. IEEE 55th ARFTG Microwave Measurements Conference*, Boston, 2000, pp. 1–5.

[11] *Focus Microwaves Data Manual,* Focus Microwaves Inc., Montreal, Canada, 1988.

[12] M.N. Tutt, D. Pavlidis, C. Tsironis, "Automated On-Wafer Noise and Load Pull Characterization Using Precision Computer Controlled Electromechanical Tuners," in *Proc. IEEE 37th ARFTG Microwave Measurements Conference*, Boston, 1991, pp. 66–75.

[13] D. Schreurs, K. Van der Zanden, J. Verspecht, W. De Raedt, and B. Nauwelaers, "Real-time measurement of InP HEMTs during large-signal RF overdrive stress," in *Proc. European Gallium Arsenide and related III-V compounds Application Symposium*, Amsterdam, 1998, pp. 545-550.

[14] F. De Groote, J.-P. Teyssier, O. Jardel, T. Gasseling, J. Verspecht, "Introduction to measurements for power transistor characterization," *IEEE Microwave Mag.*, vol. 9, no. 3, pp. 70–85, Jun. 2008.

[15] J. Rodriguez-Tellez, T. Fernandez, A. Mediavilla and A. Tazon, "Characterization of Thermal and Frequency-Dispersion Effects in GaAs MESFET Devices," *IEEE Trans. Microw. Theory and Tech.,* vol.49, pp. 1352–1355, Jul. 2001.

[16] P. McGovern, J. Benedikt, P.J. Tasker, J. Powell, K.P. Hilton, J.L. Glasper, R.S. Balmer, T. Martin, M.J. Uren, "Analysis of DC-RF dispersion in AlGaN/GaN HFETs using pulsed I-V and time-domain waveform measurements," in *Proc. IEEE MTT-S Int. Microwave Symp.*, Long Beach, 2005. [CD ROM]

[17] W. Ciccognani, F. Giannini, E. Limiti, P.E. Longhi, M.A. Nanni, A. Serino, C. Lanzieri, M. Peroni, P. Romanini, V. Camarchia, M. Pirola, G. Ghione, "GaN Device Technology: Manufacturing, Characterization, Modelling and Verification," in *Proc. IEEE 14th Conference on Microwave Techniques*, Prague, 2008, pp. 1–6.

[18] S. Augaudy, R. Quere, J.P. Teyssier, M.A. Di Forte-Poisson, S. Cassette, B. Dessertenne, S.L. Delage, "Pulse characterization of trapping and thermal effects of microwave GaN power FETs," in *Proc. IEEE MTT-S Int. Microwave Symp.*, Phoenix, 2001, pp. 427-430, May 2001.

[19] C. Fiegna, F. Filicori, G. Vannini, F. Venturi "Modeling the effects of traps on the I-V characteristics of GaAs MESFETs," in *Proc. IEEE International Electron Devices Meeting*, Washington, pp. 773–776, Dec. 1995.

[20] C. Camacho-Penalosa, "Modeling frequency dependence of output impedance of a microwave MESFET at low frequencies," *Electron. Lett.*, vol. 21, no.12, pp. 528-529, Jun. 1985.

[21] F.Filicori, G. Vannini, A. Santarelli, A.M. Sanchez, A. Tazon and Y. Newport, "Empirical modeling of low-frequency dispersive effects due to traps and thermal phenomena in III-V FET's," *IEEE Trans. Microw. Theory and Tech.,* vol. 43, pp. 2972-2981, Dec. 1995.

[22] A. Raffo, A. Santarelli, P.A. Traverso, M. Pagani, F. Palomba, F. Scappaviva, G. Vannini, F. Filicori, "Accurate PHEMT Nonlinear Modeling in the Presence of Low-Frequency Dispersive Effects," *IEEE Trans. Microw. Theory and Tech.*, vol. 53, no. 11, pp. 3449-3459, Nov. 2005.

[23] A. Raffo, V. Vadalà, G. Vannini, A. Santarelli, "A new empirical model for the characterization of low-frequency dispersive effects in FET electron devices accounting for thermal influence on the trapping state," in *Proc. IEEE MTT-S Int. Microwave Symp.*, Atlanta, 2008, pp. 1421–1424.

[24] K. Jeon, Y. Kwon, S. Hong, "A frequency dispersion model of GaAs MESFET for large-signal applications," *IEEE Microwave and Guided Wave Letters*, vol. 7, pp. 78-80, Mar. 1997.

[25] A. Santarelli, G. Vannini, F. Filicori, P. Rinaldi, “Backgating model including self-heating for low-frequency dispersive effects in III-V FETs,” *Electron. Lett.*, vol.34, no. 20, pp. 1974-1976, Oct. 1998.

[26] M. Chaibi, T. Fernandez, J. Rodriguez-Tellez, J.L. Cano, M. Aghoutane, “Accurate large-signal single current source thermal model for GaAs MESFET/HEMT,” *IEEE Electronics Letters*, vol. 43, no. 14, Jul. 2007.

[27] M. Chaibi, T. Fernandez, J.R. Tellez, A. Tazon, M. Aghoutane, “Modelling of temperature and dispersion effects in MESFET and HEMT transistors,” in *Proc. IEEE Workshop on Integrated Nonlinear Microwave and Millimetre-Wave Circuits,* Malaga, 2008, pp. 173–175.

[28] T. Roh, Y. Kim, Y. Suh, W. Park, B. Kim, “A simple and accurate MESFET channel-current model including bias-dependent dispersion and thermal phenomena”, *IEEE Trans. Microw. Theory and Tech.*, vol.45, no. 8, pp. 1252-1255, Aug. 1997.

[29] O. Jardel, F. De Groote, T. Reveyrand, J.-C. Jacquet, C. Charbonniaud, J.-P. Teyssier, D. Floriot, R. Quere, “An Electrothermal Model for AlGaN/GaN Power HEMTs Including Trapping Effects to Improve Large-Signal Simulation Results on High VSWR,” *IEEE Trans. Microw. Theory Tech.*, vol. 55, no. 12, pp. 2660–2669, Dec. 2007.

[30] I. Angelov, C. Karnfelt, “Direct Extraction Techniques for Thermal Resistance of MESFET and HEMT Devices,” in *Proc. IEEE Radio Frequency Integrated Circuits Symp.*, Honolulu, 2007, pp. 351–354.

[31] A. Raffo, V. Vadalà, P.A. Traverso, A. Santarelli, G. Vannini, F. Filicori, “An Innovative Two-Source Large-Signal Measurement System for the Characterization of Low-Frequency Dispersive Effects in FETs,” in *Proc. 16th International Measurement Confederation TC4 Symposium*, Florence, 2008, pp. 72–77.

[32] G. Crupi, D. M. M.-P. Schreurs, D. Xiao, A. Caddemi, B. Parvais, A. Mercha, and S. Decoutere, “Determination and validation of new nonlinear FinFET model based on lookup tables,” *IEEE Microwave and Wireless Components Letters*, vol. 17, no 5, pp. 361-363, May 2007.

[33] I. Angelov, N. Rorsman, J. Stenarson, M. Garcia, H. Zirath, “An empirical table-based FET model,” *IEEE Trans. Microw. Theory and Tech.*, vol 47, no. 12, pp. 2350-2357, Dec. 1999.

[34] M. Fernández-Barciela, P. J. Tasker, Y. Campos-Roca, M. Demmler, H. Massler, E. Sanchez, M. C. Curras-Francos, and M. Schlechtweg, “A simplified broadband large signal non quasi-static table-based FET model,” *IEEE Trans. Microw. Theory Tech.*, vol. 48, no. 3, pp. 395–405, Mar. 2000.

CHAPTER V :

Low-Frequency Active Load-Pull Measurement System

Introduction

Passive and active load-pull (LP) measurement systems have been widely used for electron device characterization and amplifier design [1]-[3]. As previously said they allow to test transistors under actual large-signal operating conditions by imposing at the ports of the device under test (DUT) arbitrary terminations. The measurements obtained by means of these systems are useful for the construction of load-pull contours [1] which represent a powerful tool providing information on best performance achievable by the device. The drawback is that LP setups are very expensive, especially for high power levels and high frequencies; moreover, accuracy limitations are well evident when the required terminations approach the Smith-chart edge [2]-[3]. As a matter of fact, it is difficult to synthesize the full range of device terminations especially when on-wafer devices having a large periphery are considered: passive load-pull suffers from the inability to synthesize very low impedances, whereas active load-pull may become critical from the stability point of view [4].

An alternative approach is represented by high-frequency time-domain measurement systems (Large-Signal Network Analyzers - LSNA) [5]-[7], which are able to provide a vectorial information. Nevertheless, they present the same frequency and power limitations of standard LP setups as well as critical calibration procedures.

In this chapter, a new, low-cost technique for drawing load-pull contours is presented. By exploiting the low-frequency measurement system described in chapter 3 and conventional descriptions of device parasitic elements and nonlinear reactive effects [8], the proposed approach allows to obtain the same information gathered by expensive high-frequency LP measurement systems. Moreover, some limitations previously discussed are overcome. In fact, with the described approach, the frequency range is mostly limited by the Vector Network Analyzer (VNA) exploited for the small-signal S-parameter measurements needed for the identification of the capacitance-based model, whereas, power limit is not a critical issue as high power levels can be easily achieved at low frequency without expensive instrumentation.

5.1 The proposed method

The aim of the work of this chapter is to obtain information about load-pull contours at microwave frequencies by exploiting a simple measurement system based on low-frequency large-signal I/V measurements jointly with frequency- and bias-dependent small-signal S-parameters which characterize the linear parasitic elements and nonlinear reactive effects. To this end the measurement system shown in Fig. 5.1 has been developed, which is made up of three pieces: a low frequency active load-pull I/V measurement system [8], that is largely described in chapter 3, a DC source and a VNA.

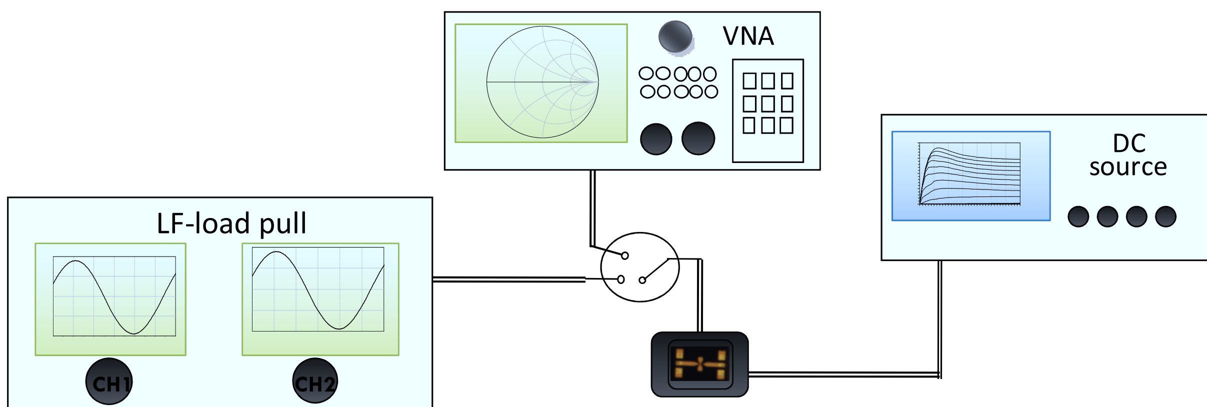

Fig. 5.1. Block-diagram of the measurement system adopted for the load-pull contour drawing

The low-frequency Load Pull system works with sinusoidal excitation set at 2 MHz, a frequency appropriate to operate above the cut-off of dispersive phenomena but low

enough to neglect dynamic effects related to the linear extrinsic parasitic network and the capacitive effects [9]. Such a system enables, for a given bias, different load conditions to be synthesized by controlling the gate and drain incident signal amplitudes and their relative phase.

The VNA is used for bias- and frequency-dependent small-signal characterization in the frequency range of interest. Finally a semiconductor analyzer (HP 4155B) provides the bias voltage for the DUT.

The low-frequency Load Pull characterization of the DUT under different terminations, together with a suitable description of the device parasitic elements and bias-dependent capacitance effects obtained by means of S-parameter measurements can be effectively exploited to draw the load-pull contours at microwave frequencies. The adopted procedure is based on the approach proposed in [8] for power amplifier design.

As suggested by conventional nonlinear model descriptions and also described in chapter 2, the intrinsic electron device can be split in two parts which can be considered strictly in parallel [8], as clearly shows Fig 5.2: the first one is purely "*resistive"* and accounts for the dc and low-frequency (LF) I\V device characteristics; the second one is purely *"capacitive"* (displacement currents) and describes the strictly nonlinear dynamic phenomena.

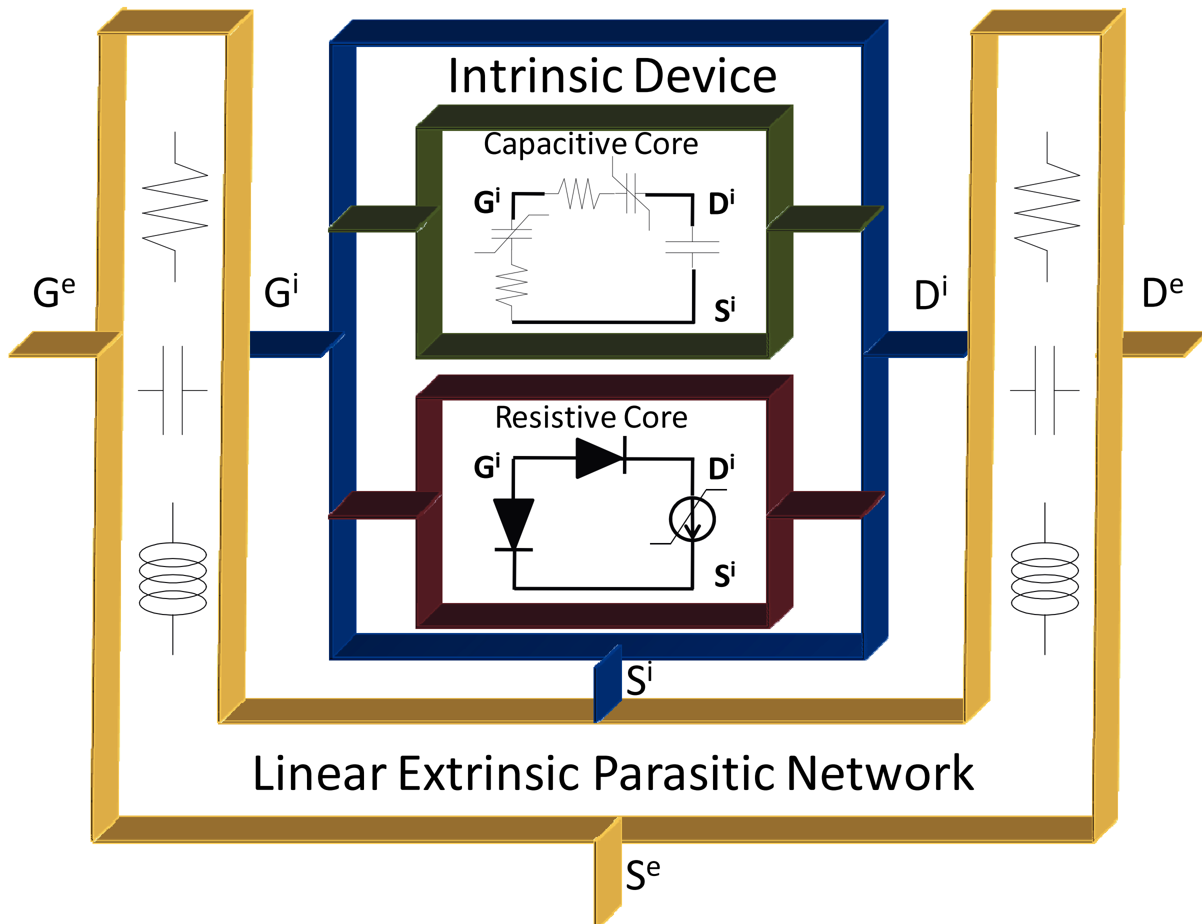

Fig. 5.2. Nonlinear equivalent circuit for a FET electron device.

The main idea is that of directly characterizing the large-signal I/V electron device behavior which is made highly complex due to important nonlinearities involved (channel current, gate-source and gate-drain junctions) and affected by important thermal and low-frequency dispersion phenomena. On the other hand, the electron device nonlinear capacitances are to some extent less affected by these phenomena and their identification on the basis of small-signal, bias- and frequency-dependent S-parameters is usually accurate enough.

Electron device parasitic elements can be identified by using well-known and sound procedures available in the literature [10]-[11]. They can be easily de-embedded from S-parameter measurements in order to obtain a bias-dependent capacitance matrix $\underline{C}$ which is stored as a look-up table.

The intrinsic and extrinsic currents and voltages will be expressed in terms of their practically finite number N of spectral components, according to:

$$x(t) = \sum_{k=-N}^{N} X(k\omega) e^{jk\omega t} \qquad (5.1)$$

The Load Pull I/V characterization carried out at a few megahertz, for each source and load condition, enables the intrinsic voltages and resistive currents to be computed through an easy de-embedding of purely resistive parasitic elements. By considering for the parasitic network in Fig. 1 any possible topology (based on lumped or distributed elements), intrinsic and extrinsic electrical variables are conveniently related by the following equations in the frequency domain:

$$\begin{bmatrix} V_{gs}^{i}(k\omega) \\ V_{ds}^{i}(k\omega) \\ I_{g}^{i}(k\omega) \\ I_{d}^{i}(k\omega) \end{bmatrix} = \underline{H}(k\omega) \begin{bmatrix} V_{gs}^{e}(k\omega) \\ V_{ds}^{e}(k\omega) \\ I_{g}^{e}(k\omega) \\ I_{d}^{e}(k\omega) \end{bmatrix}, \; k = -N,..,N \qquad (5.2)$$

where $\underline{H}(\omega)$ is a suitable hybrid-matrix description of the linear extrinsic parasitic network, $V_{gs}^{i,e}(k\,\omega)$, $I_{g}^{i,e}(k\,\omega)$ and $V_{ds}^{i,e}(k\,\omega)$, $I_{d}^{i,e}(k\,\omega)$ are respectively input and output intrinsic and extrinsic voltage and current phasors. At microwave frequencies the harmonic components of the “global” intrinsic currents are composed of the sum of the conduction[1] and displacement currents denoted with the superscripts R and C, respectively:

$$\begin{bmatrix} I_{g}^{i}(k\omega_{RF}) \\ I_{d}^{i}(k\omega_{RF}) \end{bmatrix} = \begin{bmatrix} I_{g}^{i,R}(k\omega_{RF}) + I_{g}^{i,C}(k\omega_{RF}) \\ I_{d}^{i,R}(k\omega_{RF}) + I_{d}^{i,C}(k\omega_{RF}) \end{bmatrix}, \; k = -M,..,M \qquad (5.3)$$

Successively, the obtained intrinsic voltages can be directly adopted to calculate the corresponding intrinsic *capacitive* currents contribution at the desired frequency. More precisely, the RF capacitive currents can be calculated, on the basis of the

[1] Due to the frequency-independence of the conduction current its harmonic RF-components simply coincide with the LF ones, that is $I_{x}^{i,R}(k\omega_{RF}) = I_{x}^{i,R}(k\omega_{LF})$.

capacitance matrix $\underline{C}$, starting from the intrinsic voltages measured at LF by means of the following equations:

$$\begin{bmatrix} i_g^{i,C}(t) \\ i_d^{i,C}(t) \end{bmatrix} = \begin{bmatrix} \sum_{k=-N}^{N} I_g^{i,C}(k\omega_{RF}) e^{jk\omega_{RF}t} \\ \sum_{k=-N}^{N} I_d^{i,C}(k\omega_{RF}) e^{jk\omega_{RF}t} \end{bmatrix} = = \sum_{k=-N}^{N} jk\omega_{RF} \underline{C}\left(v_{gs}^i(t), v_{ds}^i(t)\right) \begin{bmatrix} V_{gs}^i(k\omega_{LF}) e^{jk\omega_{RF}t} \\ V_{ds}^i(k\omega_{LF}) e^{jk\omega_{RF}t} \end{bmatrix}, \quad (5.4)$$

where input and output intrinsic voltage phasors $V_{gs}^{i}(k\ \omega_{LF})$ and $V_{ds}^{i}(k\ \omega_{LF})$ are multiplied by $e^{jk\omega RFt}$ and thus *"reallocated"* at RF, while $v_{gs}^{i}(t)$ and $v_{ds}^{i}(t)$ are the corresponding time-domain quantities. The intrinsic capacitance currents in Eq. (5.4) are summed to the resistive ones obtained by the large-signal I/V measurements, in order to obtain the *"global"* intrinsic currents. The last step consists of applying straightforward mathematical procedures to compute, on the basis of the parasitic network description, the extrinsic electrical variables. These quantities uniquely define the load and source terminations, given by Eq. (5.5) and (5.6).

$$Z_L(k\omega_{RF}) = -\frac{V_{ds}^e(k\omega_{RF})}{I_d^e(k\omega_{RF})} \quad (5.5)$$

$$Z_{IN}(k\omega_{RF}) = \frac{V_{gs}^e(k\omega_{RF})}{I_g^e(k\omega_{RF})} \quad (5.6)$$

The whole procedure clearly enables also electrical figures (i.e., output power, drain efficiency, DC converted currents, etc.) to be computed. Moreover, it is noteworthy that the device intrinsic load-line is directly gathered, which can be very useful in order to assess reliability constraints [12].

The described procedure can be repeated for different source and load conditions synthesized at low frequencies, in order to draw load-pull contours (e.g., output

power, efficiency, etc.).

In the previous discussion a purely capacitance-based description of the intrinsic device has been considered. When non quasi-static effects are important, series RC networks must be considered instead of pure capacitances. This makes the mathematical part of the approach slightly more involved yet preserving the accurate evaluation of the electron device performance.

5.2 Experimental results

The proposed approach has been validated by predicting constant power contours for a 400 μm periphery 0.25 μm GaN HEMT device at 7 GHz. S-parameter measurements (2 GHz – 40 GHz) were carried out for a wide range of bias conditions (- 6 V < V_{g0} < 1 V, 0 V < V_{d0} < 36 V). Successively, the device parasitic network was identified and its resistive part used to de-embed both the low frequency Load Pull I/V and S-parameter measurements. The imaginary parts of the intrinsic Y-parameters obtained after parasitic de-embedding directly provide the device $\underline{C}$ matrix. It should be noticed that (see Fig. 5.3), non quasi-static effects can be reasonably neglected since, at the frequency of 7 GHz and for class-A device operation, they are of minor importance up to 14 GHz.

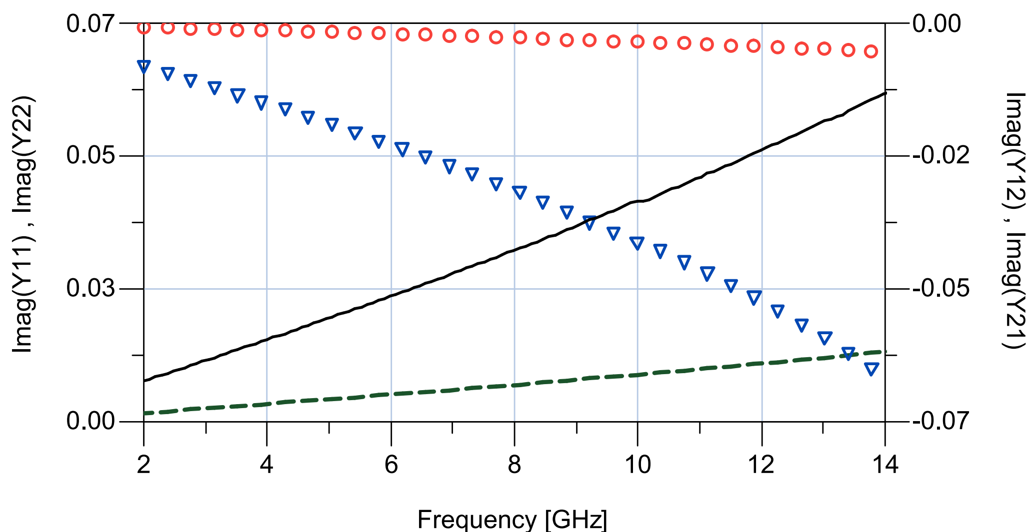

Fig. 5.3. Y-parameter imaginary parts at the intrinsic device (bias condition V_{g0} = -2 V, V_{d0} = 25 V). Y(1,1) (continues line) and Y(1,2) (dotted line) Y(2,1) (circle) and Y(2,2) (triangles).

Fig. 5.4 shows an example of measurements performed by means of the LF measurement system on the DUT biased under class-A operation. The different load-lines, corresponding to the same output impedance Z_L*=86.61-j*40.80* Ω, are obtained by varying proportionally the amplitude of the gate and drain incident signals and keeping constant the relative phase.

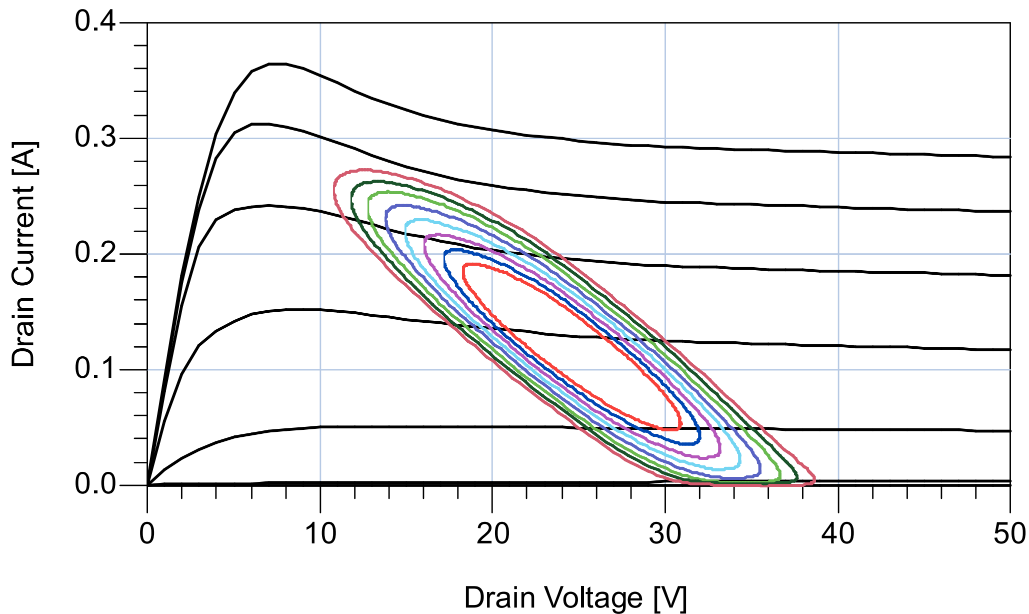

Fig. 5.4. Low-frequency measurements for constant impedance Z_L=86.61-j*40.80 Ω as a function of increasing input power (bias condition V_{g0} = -2 V, V_{d0} = 25 V). The load-lines are superimposed to DC characteristics (-5 V < V_{g0} < 1 V , step 1 V).

This measurement set is practically a "power sweep" carried out up to 1 dB gain compression. The procedure previously described to obtain the load termination at 7 GHz was applied to this measurement set and provided Z_L=82.61+j*28.97 Ω with an output power of 29.57 dBm The same load condition was measured with a passive high-frequency load-pull measurement system [3]. Fig. 5.5 shows the comparison between LP measurements and the ones obtained through the proposed technique (output power, gain, power efficiency and average current) as a function of the available input power. The excellent agreement confirms the validity of the proposed technique.

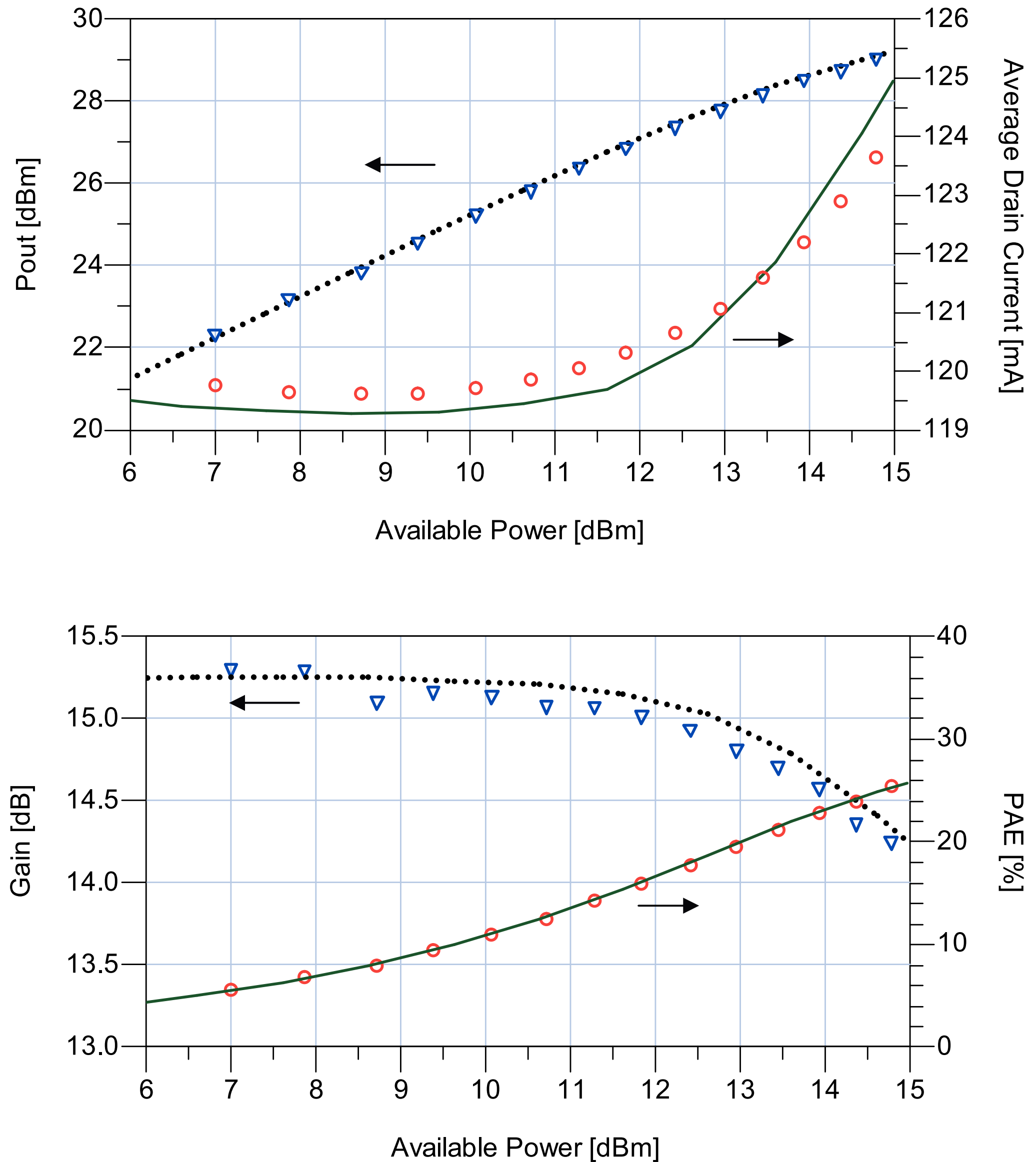

Fig. 5.5. Load-pull measurements (lines) carried out at 7 GHz for V_{g0} = -2 V, V_{d0} = 25 V and Z_L=83.80+j*27.17 Ω versus measurements obtained by applying the proposed approach (symbols) for the same load impedance. a) Output power and average drain current. b) Power added efficiency and transducer power gain

Different impedances were synthesized adopting this technique to draw accurate load-pull contours. Fig. 5.6 shows how each of the nineteen low-frequency impedances considered maps itself at high frequency. Measurements carried out under class-A bias and by sweeping the input power level, provide all the information needed for power contours tracing. Fig. 5.7 shows the constant output power contours at 7 GHz for constant levels of the drain average current obtained by means of the proposed technique and the load-pull measurement system. These contours represent constant output power loci at constant drain efficiency. The optimal output

impedance found with the described approach is Z_L=82.61+j*28.97 Ω which corresponds to a power equal to 29.57 dBm and an efficiency of 26%. The measurements carried out at 7 GHz by means of the LP system gives a maximum output power equal to 29.12 dBm and efficiency around 25% at Z_L=83.80+j*27.17 Ω. In terms of efficiency this point represents the maximum efficiency reached in the considered impedance range. Graphs shown in Fig 5.5 represent the performance of the device for the optimal impedance. It is interesting to notice that the proposed technique, for a fixed bias condition, allows to draw load-pull contours at any frequency of interest by simply re-applying simple mathematical procedures

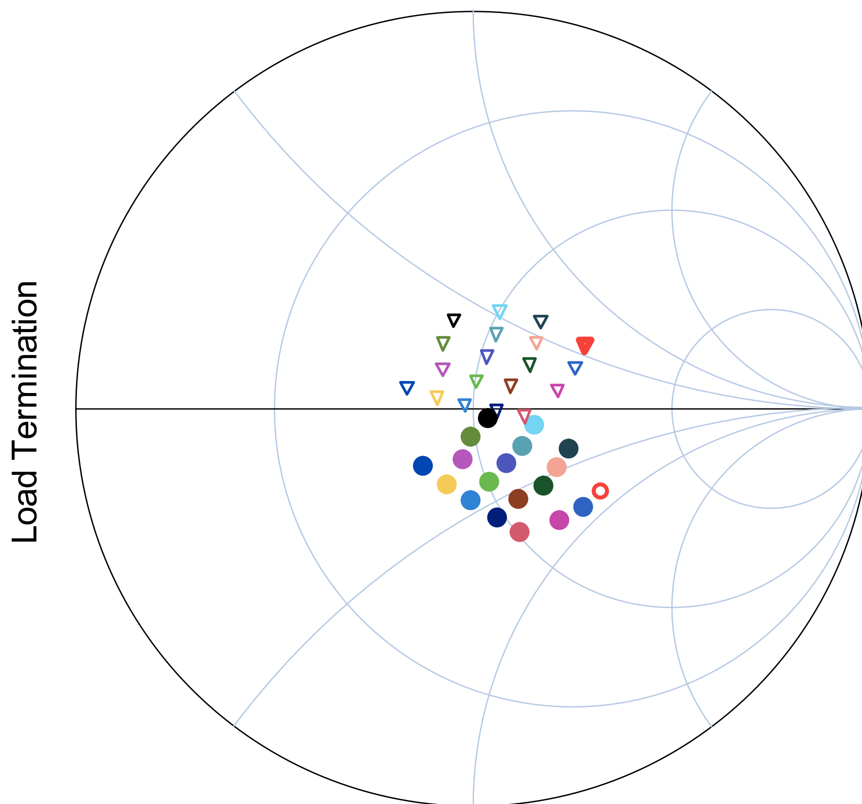

Fig. 5.6. Load impedances at 2 MHz (circles) and at 7 GHz (triangles) obtained by applying the proposed approach. The empty circle and filled triangle represent the optimal impedance

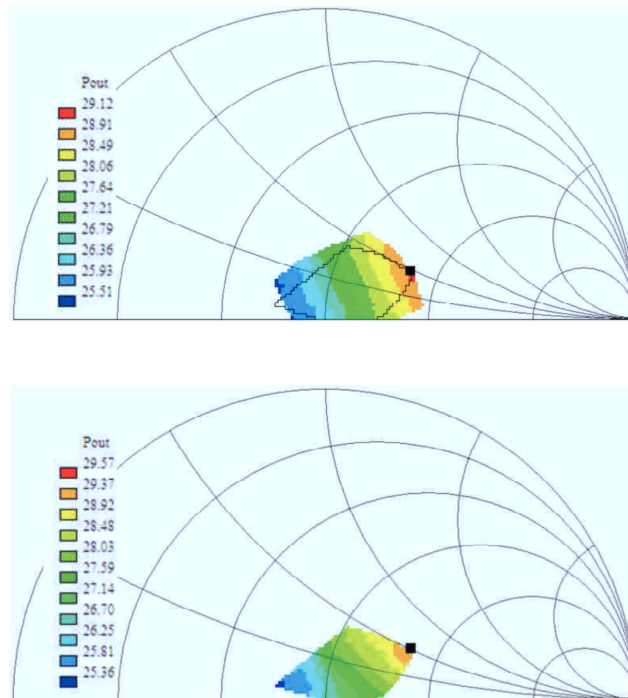

Fig. 5.7. Constant output power contours at constant average drain current I_{D0}=125 *mA* obtained by measurements at 7 GHz (a), and by exploiting the proposed approach (b).

Conclusions

A low-cost, simple approach for power contours drawing based both on large-signal low-frequency I/V measurements and a small-signal measurement-based description of nonlinear reactive effects has been proposed.

The method has provided excellent agreement with experimental results obtained by means of complex and expensive high-frequency load-pull setups

References

[1] J.M. Cusak, S.M. Perlow, B.S. Perlman, “Automatic load contour mapping for microwave power transistors,” *IEEE Trans. On Microw. Theory and Tech.*, vol. 22, no. 12, pp.1146-1152, Dec. 1974.

[2] A. Ferrero, V. Teppati, “Accuracy Evaluation of On-Wafer Load-Pull Measurements,” in Proc. *IEEE 55th ARFTG Microwave Measurements Conference*, Boston, 2000, pp. 1– 5L.

[3] *Focus Microwaves Data Manual,* Focus Microwaves Inc., Montreal, Canada, 1988.

[4] F. Giannini, G. Leuzzi, *Nonlinear Microwave Circuit Design*. Chichester, England: Wiley, 2004.

[5] J. Verspecht, “Large signal network analysis,” *IEEE Microwave Mag.*, vol. 6, no. 4, pp. 82–92, Dec. 2005.

[6] J. Benedikt, R. Gaddi, P. Tasker, and M. Goss, “High-power time-domain measurement system with active harmonic load-pull for high-efficiency base-station amplifier design,” *IEEE Trans. Microw. Theory Tech.*, vol. 48, no. 12, pp. 2617–2624, Dec. 2000.

[7] F. De Groote, J.-P. Teyssier, O. Jardel, T. Gasseling, J. Verspecht, “Introduction to measurements for power transistor characterization,” *IEEE Microwave Mag.*, vol. 9, no. 3, pp. 70–85, Jun. 2008.

[8] A. Raffo, F. Scappaviva, G. Vannini, “A New Approach to Microwave Power Amplifier Design Based on the Experimental Characterization of the Intrinsic Electron-Device Load Line,” *IEEE Trans. Microwave Theory & Tech.,* vol. 57, no. 7, pp. 1743-1742, July 2009

[9] A. Raffo, A. Santarelli, P.A. Traverso, M. Pagani, F. Palomba, F. Scappaviva, G. Vannini, F. Filicori, “Accurate PHEMT Nonlinear Modeling in the Presence of Low-Frequency Dispersive Effects,” *IEEE Trans. Microw. Theory and Tech.*, vol. 53, no. 11, pp. 3449-3459, Nov. 2005.

[10] G. Dambrine, A. Cappy, F. Heliodore, and E. Playez, “A new method for determining the FET small-signal equivalent circuit,” *IEEE Trans. Microw. Theory Tech.*, vol. 36, no. 7, pp. 1151–1159, Jul. 1988

[11] D. Resca, A. Santarelli, A. Raffo, R. Cignani, G. Vannini, F. Filicori, D.M.M.-P. Schreurs, “Scalable Nonlinear FET Model Based on a Distributed Parasitic Network Description,” *IEEE Trans. Microw. Theory and Tech.*, vol. 56, no. 4, pp. 755-766, Apr. 2008

[12] R. Menozzi, “Off-state breakdown of GaAs PHEMTs: Review and new data,” *IEEE Trans. Device Mater. Rel.*, vol. 4, no. 1, pp. 54–62, Mar.2004

List of Publications

- ✓ Antonio Raffo, **Valeria Vadalà**, Pier Andrea Traverso, Alberto Santarelli,Giorgio Vannini, Fabio Filicori, "***A Dual-Source Nonlinear Measurement System Oriented to the Empirical Characterization of Low-Frequency Dispersion in Microwave Electron Devices***" accepted for publication on *CSJI- Computer Standards & Interfaces*
- ✓ Antonio Raffo, **Valeria Vadalà**, Dominique M. M.-P. Schreurs, Giovanni Crupi, Gustavo Avolio, Alina Caddemi, and Giorgio Vannini, "**Nonlinear Dispersive Modeling of Electron Devices Oriented to GaN Power Amplifier Design"** , accepted for publication on *IEEE Trans. on Microwave Theory and Tech (April 2009)*
- ✓ Antonio Raffo, **Valeria Vadalà**, Pier Andrea Traverso, Alberto Santarelli, Giorgio Vannini, Fabio Filicori, "An Innovative Two-Source Large-Signal Measurement System for the Characterization of Low-Frequency Dispersive Effects in FETs" *IMEKO 16th Symposium on Electrical Measurements and Instrumentation & 13th Workshop on ADC Modelling and Testing (TC4), Florence, ITALY, (September 2008).*
- ✓ Antonio Raffo, **Valeria Vadalà**, Giorgio Vannini, and Alberto Santarelli, "A New Empirical Model for the Characterization of Low-Frequency Dispersive Effects in FET Electron Devices Accounting for Thermal Influence on the Trapping State" *IMS International Microwave Symposium Atlanta (15-20 June 2008).*
- ✓ Antonio Raffo , Sergio Di Falco, **Valeria Vadalà**, Giorgio Vannini, "Class-A Power Amplifier Design Technique Based on Electron Device Low-Frequency Characterization". *EuMic - European Microwave Integrated Circuits Conference - Rome, (28-29 September 2009).*
- ✓ Gustavo Avolio , Antonio Raffo , Dominique M. M.-P. Schreurs, **Valeria Vadalà**, Sergio Di Falco, Walter de Raedt, Bart Nauwelaers, Giorgio Vannini , "Experimental Investigation of LF Dispersion and IMD Asymmetry within GaN based HEMT Technology" *accepted in INMMiC Conf., Göteborg 26-27 April, 2010.*

- ✓ Antonio Raffo , **<u>Valeria Vadalà</u>** , Sergio Di Falco , Giorgio Vannini “Hybrid Approach to Microwave Power Amplifier Design” , *accepted in INMMiC Conf., Göteborg 26-27 April, 2010.*
- ✓ **<u>Valeria Vadalà</u>**, Antonio Raffo, Sergio Di Falco and Giorgio Vannini “A Low-Cost and Accurate Technique for the Prediction of Load-Pull Contours” *accepted in IMS International Microwave Symposium, Anaheim , Los Angeles (22-28 May 2010).*

Publication under Review

- ✓ Antonio Raffo , Sergio Di Falco, **<u>Valeria Vadalà</u>**, Giorgio Vannini , “Characterization of GaN HEMT Low-Frequency Dispersion Through a Multi-Harmonic Measurement System” , Review on *IEEE Trans. on Microwave Theory and Tech*
- ✓ Antonio Raffo , Sergio Di Falco, **<u>Valeria Vadalà</u>**, Giorgio Vannini , “Characterization of Electron Device Breakdown Under Nonlinear Dynamic Operation” , Review on *EuMic - European Microwave Integrated Circuits Conference , Paris 2010.*

Acknowledgment

Only a few words to thank all those who, near or far, have accompanied and supported me in these three years. First of all I would really like to thank my tutor , Prof. Giorgio Vannini, who given to me the confidence and the opportunity to live this wonderful experience. I also wish to thank Antonio Raffo, my mentor and “the lighthouse” in the sea of research. He has been helping me in all the difficulties faced during my work, passing the passion for this work on to me.
My gratitude goes also to my family and my friends who have to stand me all the time.

Registrazione modulo Dichiarazione di conformità

MODULO INVIATO CORRETTAMENTE

Consegnare la copia stampata e debitamente firmata all'Ufficio Dottorato e Alta Formazione in via Scienze 41b Ferrara

Io sottoscritto Dott. (Cognome e Nome) **Vadalà Valeria**

nato a **Reggio Calabria**

Provincia **RC**

il giorno **25-11-1982**

Your E-Mail Address **valeria.vadala@unife.it**

avendo frequentato il corso di Dottorato di Ricerca in: **Scienze dell'Ingegneria**

Ciclo di Dottorato **XXII**

Titolo della tesi in Italiano

CARATTERIZZAZIONE E MODELING DEGLI EFFETTI DISPERSIVI IN BASSA FREQUENZA NEI DISPOSITIVI ELETTRONICI III-V

Titolo della tesi in Inglese

CHARACTERIZATION AND MODELING OF LOW FREQUENCY DISPERSIVE EFFECTS IN III-V ELECTRON DEVICES

Tutore - Prof: **Giorgio Vannini**

Settore Scientifico Disciplinare (SSD) **ING-INF/01**

Parole chiave (max 10) **SEMICONDUCTOR DEVICE MODELING , NON-LINEAR MEASUREMENTS , FETs**

Consapevole - Dichiara

CONSAPEVOLE --- 1) del fatto che in caso di dichiarazioni mendaci, oltre alle sanzioni previste dal codice penale e dalle Leggi speciali per l'ipotesi di falsità in atti ed uso di atti falsi, decade fin dall'inizio e senza necessità di alcuna formalità dai benefici conseguenti al provvedimento emanato sulla base di tali dichiarazioni; -- 2) dell'obbligo per l'Università di provvedere al deposito di legge delle tesi di dottorato al fine di assicurarne la conservazione e la consultabilità da parte di terzi; -- 3) della procedura adottata dall'Università di Ferrara ove si richiede che la tesi sia consegnata dal dottorando in 4 copie di cui una in formato cartaceo e tre in formato .pdf, non modificabile su idonei supporti (CD-ROM, DVD) secondo le istruzioni pubblicate sul sito : http://www.unife.it/dottorati/dottorati.htm alla voce ESAME FINALE – disposizioni e modulistica; -- 4) del fatto che l'Università sulla base dei dati forniti, archivierà e renderà

consultabile in rete il testo completo della tesi di dottorato di cui alla presente dichiarazione attraverso l'Archivio istituzionale ad accesso aperto "EPRINTS.unife.it" oltre che attraverso i Cataloghi delle Biblioteche Nazionali Centrali di Roma e Firenze. --- DICHIARO SOTTO LA MIA RESPONSABILITA' --- 1) che la copia della tesi depositata presso l'Università di Ferrara in formato cartaceo, è del tutto identica a quelle presentate in formato elettronico (CD-ROM, DVD), a quelle da inviare ai Commissari di esame finale e alla copia che produrrò in seduta d'esame finale. Di conseguenza va esclusa qualsiasi responsabilità dell'Ateneo stesso per quanto riguarda eventuali errori, imprecisioni o omissioni nei contenuti della tesi; -- 2) di prendere atto che la tesi in formato cartaceo è l'unica alla quale farà riferimento l'Università per rilasciare, a mia richiesta, la dichiarazione di conformità di eventuali copie; -- 3) che il contenuto e l'organizzazione della tesi è opera originale da me realizzata e non compromette in alcun modo i diritti di terzi, ivi compresi quelli relativi alla sicurezza dei dati personali; che pertanto l'Università è in ogni caso esente da responsabilità di qualsivoglia natura civile, amministrativa o penale e sarà da me tenuta indenne da qualsiasi richiesta o rivendicazione da parte di terzi; -- 4) che la tesi di dottorato non è il risultato di attività rientranti nella normativa sulla proprietà industriale, non è stata prodotta nell'ambito di progetti finanziati da soggetti pubblici o privati con vincoli alla divulgazione dei risultati, non è oggetto di eventuali registrazioni di tipo brevettale o di tutela. --- PER ACCETAZIONE DI QUANTO SOPRA RIPORTATO

Firma Dottorando

Ferrara, lì **01/03/2010**

Firma del Dottorando **VALERIA VADALA'**

Firma Tutore

Visto: Il Tutore

Si approva

Firma del Tutore **GIORGIO VANNINI**

FORMAZIONE POSTLAUREA

Ufficio Dottorato di Ricerca - Ufficio Alta Formazione ed Esami di Stato - IUSS